Julius-Maximilians-
UNIVERSITÄT
WÜRZBURG

UNIVERSITÄT WÜRZBURG
PHYSIKALISCHES INSTITUT
epVI

Optical spectroscopy on silicon vacancy defects in silicon carbide

Dissertation zur Erlangung des naturwissenschaftlichen Doktorgrades der Julius-Maximilians-Universität Würzburg

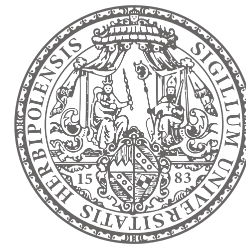

vorgelegt von
Franziska Fuchs
aus Bamberg

Würzburg, 2015

CC BY NC SA

Eingereicht am: 09. Juli 2015
bei der Fakultät für Physik und Astronomie

1. Gutachter: Prof. Dr. Vladimir Dyakonov
2. Gutachter: Prof. Dr. Jean Geurts
3. Gutachter: -
der Dissertation.

Vorsitzende(r)

1. Prüfer: Prof. Dr. Vladimir Dyakonov
2. Prüfer: Prof. Dr. Jean Geurts
3. Prüfer: Prof. Dr. Matthias Kadler
im Promotionskolloquium.

Tag des Promotionskolloquiums: 28. September 2015

Doktorurkunde ausgehändigt am:

Contents

1. Introduction 7

2. Theory 9
2.1. An old acquaintance – silicon carbide . . . 9
2.1.1. Properties of silicon carbide . . . 10
2.1.2. Polytypes . . . 10
2.1.3. Growth of silicon carbide . . . 12
2.2. Shining like new – defects in silicon carbide . . . 14
2.2.1. Types of defects . . . 14
2.2.2. Color centers and their application . . . 16
2.2.3. Spin defects . . . 17
2.3. Silicon vacancy in SiC . . . 21
2.3.1. Energy level model . . . 21
2.3.2. Photoluminescence . . . 23
2.3.3. Spin state . . . 24
2.3.4. The zero field interaction . . . 25
2.3.5. Optical cycle model . . . 28
2.3.6. Photon statistics . . . 29

3. Methods 35
3.1. Luminescence spectroscopy . . . 35
3.2. Optically detected magnetic resonance . . . 36
3.3. Single photon counting . . . 37
3.4. The experimental setups . . . 37
3.4.1. LabRAM . . . 38
3.4.2. Home-built zfODMR setup . . . 39
3.4.3. Single photon counting setup . . . 40
3.4.4. Combined imaging setup . . . 40

4. Optical properties of silicon vacancies 43
4.1. Creation of silicon vacancies . . . 43

4.2. Optical excitation and recombination dynamics 47

5. Defect engineering of silicon vacancies 53

5.1. Controlling defect density 53

5.2. Single silicon vacancies 58

5.3. Annealing behavior 64

6. Electrical excitation in a SiC LED structure 69

6.1. Emission in the visible range 70

6.2. NIR emission from V_{Si} 72

6.3. Emission and LED characteristic 73

7. Silicon vacancies in silicon carbide nanocrystals 77

7.1. Nanoparticles and their applications for bioimaging 77

7.2. SiC nanocrystals (NCs) 79

7.2.1. Fabrication 79

7.2.2. Characterization 79

7.3. Photoluminescence of silicon vacancies in SiC NCs 82

7.4. ODMR of silicon vacancies in SiC NCs 85

8. Summary 89

Bibliography 92

A. Appendix 109

A.1. Samples used in this thesis 109

A.2. Correlation function 110

A.3. Calculation of transition rates 111

A.4. Publications and conference contributions 113

A.5. Danksagung 115

1. Introduction

The discovery of non-classical quantum effects triggered one of the most striking developments in the 20th century. With the quantization of light and quantum mechanics, many experiments could then be explained. Especially on the atomic scale, our *customary classical* experience fails, as things behave quantum mechanically.

In our computerized world, where the size of hardware components is continuously shrinking, we will reach into this atom-scale quantum world sooner or later. Thus, its effect on the nowadays classical digital data handling with bits has to be considered. But one could also turn the tables and employ a quantum system for computational tasks. Feynman stated already in 1982, that only a quantum computer could simulate a real quantum system in a satisfactory way [1]. The following 30 years of research didn't achieve a breakthrough and thus in 2010 Nielsen notes that *"it remains a great challenge to physicists and engineers of the future to develop techniques for making large-scale quantum information processing a reality."* [2, p. 4, ll. 5-7].

One critical point is to find a suitable quantum system, at first fulfilling the DiVincenzo criteria [3], but also being convertible at ambient conditions. While the DiVincenzo criteria are fulfilled by several systems, like quantum dots, superconducting Josephson junctions or single trapped ions/atoms and quantum operations succeeded on laboratory scale, these systems need low temperatures. In contrast, spin defects in semiconductors are promising candidates for room temperature quantum applications, like quantum metrology, quantum computing and communication as well as spintronics. Even at ambient conditions, they behave like artificial single atoms with the surrounding semiconductor as vacuum-like matrix. Optical excitation and readout is straight-forward and the nonzero spin makes them sensitive to magnetic resonance. With the most prominent example, the NV (nitrogen-vacancy) center in diamond, several applications have been shown [4, 5, 6, 7, 8, 9, 10]. Yet, the system faces some drawbacks. First, an extrinsic nitrogen atom is needed to form the defect, second the emission in the visible range and the spin state of S=1 is strain sensitive, limiting reproducibility. Therefore research of complementary defect systems is promising.

The here investigated defect -the silicon vacancy in silicon carbide- is indeed such an alternative. Its technologically developed host system SiC, the vacancy's near in-

frared emission and its high spin state of S=3/2 are advantageous for many purposes. Coherent spin manipulation of single silicon vacancies has been shown [11, 12], but there are still open question about basic physical properties of the defect. The here presented investigations answer some of these and proof-of-principle measurements provide a guideline regarding the feasibility of certain applications, e.g. electrically driven single photon sources or nanocrystal-embedded defects.

The first chapter introduces general properties of the host system silicon carbide, classifies defects and then provides theoretical background as well as state-of-the-art knowledge of the silicon vacancy. Subsequently, the second chapter describes the used spectroscopical methods and experimental setups. The next four chapters give the experimental results of my investigation. The treated topics, namely defect creation and optical properties of silicon vacancies, defect engineering, electrical excitation and silicon vacancies in SiC nanocrystals and the obtained insights are summarized in the final chapter.

2. Theory

This chapter describes important aspects of silicon carbide (SiC) as well as its defects and finally the investigated protagonist, the silicon vacancy.

2.1. An old acquaintance – silicon carbide

Silicon carbide is a crystalline solid state semiconductor (compare figure 2.1) consisting of silicon $_{14}$Si and carbon $_{6}$C atoms and is the only stable compound of these two elements [13].

The idea, that a compound of silicon and carbon may exist, was first mentioned 1824 by Berzelius [14]. Already in the late 19th century the first method to artificially grow silicon carbide was developed and patented by Acheson [15]. Around 1892, in vicinity of the Barringer Crater (Arizona, USA), the meteorite Cañon Diablo was found , in which Henry Moissan discovered the first natural silicon carbide crystals [16] (therefore also called *moissanite*). SiC is being used for various applications: as abrasive (mostly under the name *carborundum*), as ceramics for automotive industry (*carbon ceramic* car brake disks), bulletproof vests or space applications (mirrors for astronomical telescopes), in power electronics (e.g. MOSFETs etc.). Especially since the 1990s it is seen as an alternative to silicon in semiconductor industries [17, in German]. Since February 2012 some wagons of Tokyo's Ginza metro line are being driven with power supply and inverters based on silicon carbide, exhibiting several advantages over the corresponding silicon based devices, leading to an energy saving of 30% [18]. Last but not least, silicon carbide is also used for jewelry [19]), and is almost as brilliant as diamond.

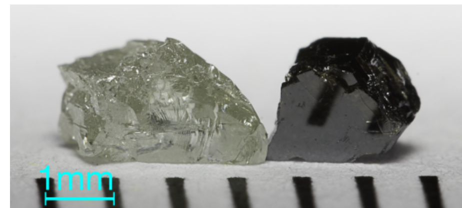

Figure 2.1.: Silicon carbide crystals of polytpye 4H. Left: as-grown, transparent. Right: after irradiation; Rayleigh scattering on introduced defects leads to opaqueness. *photography by K. Kister, with kind permission.*

From these applications it is obvious that silicon carbide is an elusively versatile material.

This section will elucidate its properties and mention the different fabrication techniques. A good overview over SiC properties can also be found in Chapter 1 of [20].

2.1.1. Properties of silicon carbide

Silicon carbide combines two elements from the fourth main group in the periodic system. It can be seen as a hybrid between pure silicon and diamond as its physical properties often lie in between the values for the two elemental materials, which is exemplarily shown in table 2.1.

	Silicon [21]	Silicon carbide	Diamond [22]
Bond length [Å]	2.3	1.9	1.5
Hardness [Mohs]	6.5	9.5	10
Band gap [eV]	1.1	2.3-3.3	5.5
Breakdown field [10^5 Vcm^{-1}]	3	40-60	
Thermal conductivity [W(cmK)$^{-1}$]	1.1	3.87	10-25

Table 2.1.: Properties of SiC in comparison with silicon and diamond. Values for SiC taken from [21, 23, 24, 25].

In silicon carbide, every carbon atom is tetragonally surrounded by four silicon atoms and vice versa. The covalent bonding between the atoms makes SiC chemically inert to most substances. Additionally, it is mechanically robust due to the high hardness, making it an ideal abrasive. The band gap of silicon carbide lies between that of silicon and diamond and can vary between ca. 2.3 eV and 3.3 eV [21], depending on the crystal configuration. Due to the rather high band gap, SiC exhibits a high breakdown field and good thermal stability (sublimation at 2100°C [21]) as well as high thermal conductivity. This makes it suitable for high power electronics at elevated temperatures and operating frequencies. Moreover, SiC was the material, on which the electroluminescent effect was discovered in 1907 by Round [26], which is the working principle for light emitting diodes. As stated by Zheludev [27], Losev, a russian technician, independently not only observed but also explained and moreover understood the potential of the luminescence of SiC diodes in the mid 1920s.

2.1.2. Polytypes

A special feature of silicon carbide is its polytypism, which means that the crystal can occur in different crystallographic structures, although the chemical formula is identical. The polytypes of SiC are indistinguishable in two dimensions, but differ in the third. The crystal can be imagined as a stacking sequence of Si-C double layers, and this sequence can be varied. Starting with the first Si-C layer on position A and the

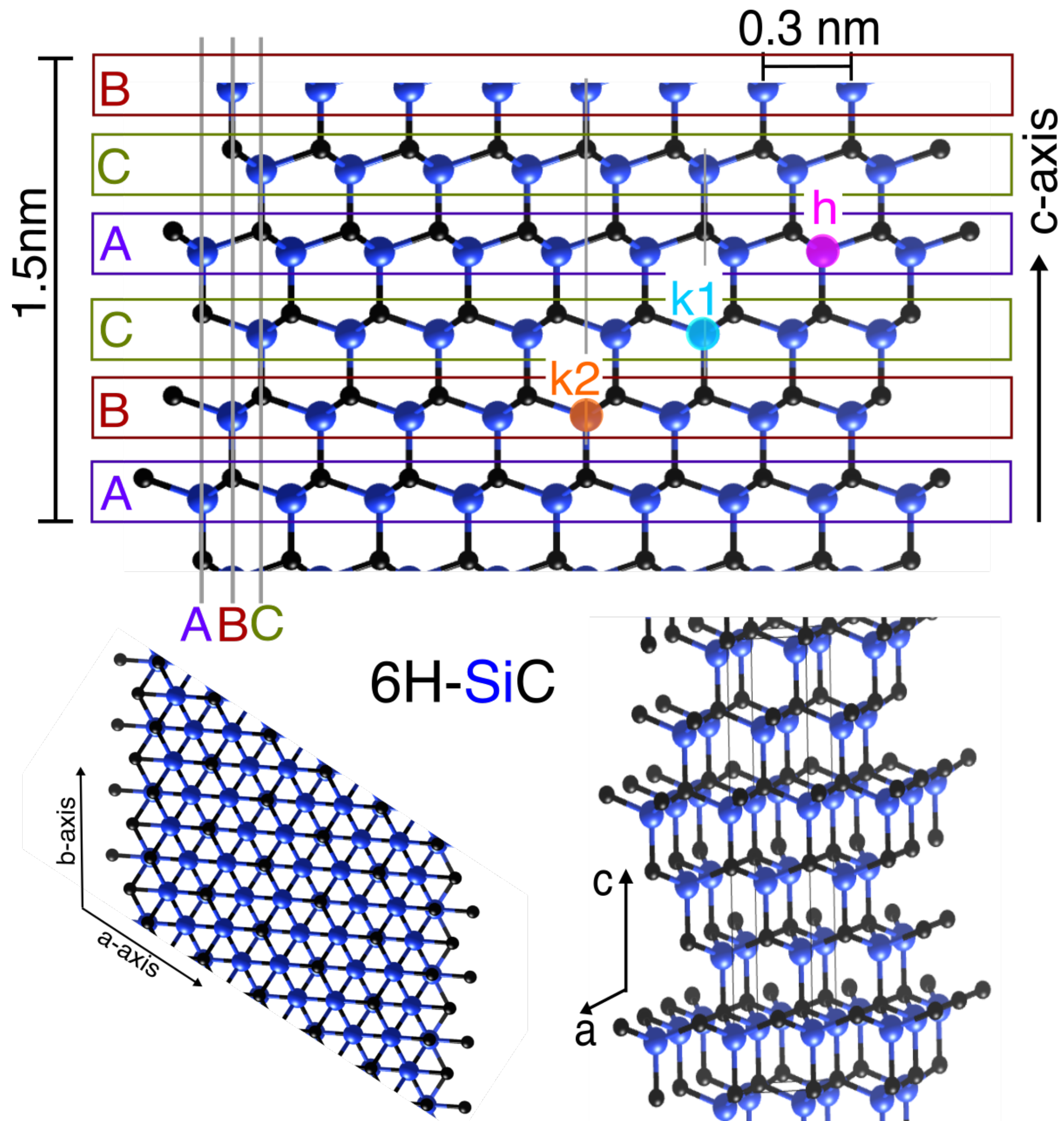

Figure 2.2.: Silicon carbide crystal structure of polytype 6H. Si atoms are blue, carbon atoms black. **Top:** cut through a-c-plane. The pattern ABCACB of one stacking sequence of Si-C double-layers is denoted with colored rectangles. Three inequivalent lattice sites h, k1 and k2 are exemplarily highlighted. **Bottom left:** cut through a-b-plane reveals the hexagonal crystal structure. **Bottom right:** 3-dimensional view. Drawings produced with VESTA [28].

second on position B, one can place the third layer either in position A again (resulting in hexagonal close packing AB**A**), or on position C (giving cubic close packing AB**C**). Hence, many different polytypes can be formed and among them more than 250 stable polytypes are known [13]. The nomenclature is as follows: A number for the stacking layer periodicity and a letter for the phase, e.g. cubic (C), hexagonal (H) or rhombic (R). The most common polytypes are 3C (stacking sequence ABC), 4H (ABAC) and 6H (AB-

CACB). The latter can be seen in figure 2.2. As a consequence of the stacking sequence, inequivalent lattice positions in the crystal occur. Their next-neighbor configuration is equal, but the next-but-one atoms have a different arrangement. One can distinguish cubic or hexagonal lattice sites. For example 4H-SiC has two inequivalent sites, one cubic (k) and one hexagonal (h). 6H-SiC possesses 3 inequivalent positions, two cubic (k_1 and k_2) and one hexagonal (h). The before mentioned band gap variation is also due to different polytypes. For example in 3C-SiC, the bandgap is 2.3 eV, and it is 3.0 eV for 6H-SiC [21]. Nevertheless, the band gap differences are not crucial for the investigations of this thesis, as the energy states of the investigated defects are located within the band gap and we use excitation energies below 2 eV.

2.1.3. Growth of silicon carbide

There is some natural occurrence of silicon carbide, but especially for industrial use, large scale fabrication methods for single crystals are preferable. This section gives a short overview over basic principles. For a good and compact overview over growth of SiC (until beginning of the 1990s) I recommend section 2 in [21], for detailed insight into special topics I refer to [29].

The first method growing silicon carbide was developed in the late 19th century [15] and produced SiC via a high current (resulting in elevated temperatures) in a mixture of carbonaceous material and silica. As SiC doesn't melt under atmospheric pressure (instead it sublimates at 1800°C [21]), a growth out of a melt like e.g. the Czochralski process – which is often used for silicon – is impossible. So the prevailing processes are based on sublimation, especially for large bulk samples. The oldest sublimation technique is the Lely growth method (patented by Jan Anthony Lely in 1958) [30], working at ca. 2500°C close to chemical equilibrium and via a temperature gradient within the crucible. Its advantages are that it works without a seed crystal and one can achieve a very good crystal quality. But this comes along with limited and random shapes. This sublimation method was later modified and improved by Tairov and Tsvetkov, using lower temperatures and a better temperature gradient as well as a seed to better control the nucleation process [31]. State of the art bulk seeded sublimation growth is mostly carried out with physical vapor transport [29, p. 1]. Besides sublimation techniques there is also liquid phase epitaxy, where dissolving carbon in liquid silicon produces SiC crystals, as well as chemical vapor deposition [21].

Another important issue, especially for semiconductor electronics, is doping. SiC can be doped n-type (mostly with nitrogen) or p-type (with aluminum, boron or phosphor). The dopant is either present as impurity in the precursor material or has to be

added either during growth or afterwards via ion implantation. With the Lely method, N concentrations of 10^{16}-10^{19} cm^{-3} are typical [25, 32].

Samples used in this thesis

The samples used in this thesis are of polytypes 4H and 6H and were grown either via sublimation or epitaxial. Depending on the application, the doping type and level was adapted. The samples also experienced different post-growth treatments, e.g. irradiation, annealing or milling. This is summarized in table A.1 in the appendix.

2.2. Shining like new – defects in silicon carbide

After having clarified the properties of silicon carbide, we turn our attention onto defects in SiC. As there are several different kinds of defects, the first section will introduce their general classification in semiconductors. Following, color centers and their applications are described. The last section treats more specifically point defects carrying a spin, as the investigated silicon vacancy defect belongs to that species of color centers.

2.2.1. Types of defects

Crystallographic defects can generally be defined as deviations from the regular pattern or imperfections in the ideal crystal lattice. Effectively, defects always occur in real crystals and are sometimes even relevant for its properties. Defects can be classified by their dimensionality, from extended 3-dimensional to pointlike 0-dimensional defects.

Three-dimensional defects

Bulky defects can be formed by clusters of impurities, inclusions or precipitates, but also voids. From a physical point of view, they do not alter the properties of the host material, although they can limit its performance or mechanical stability.

Two-dimensional defects

Those defects are mostly planar and occur e.g. at grain boundaries, the interface of crystallites with different crystallographic orientation. Grain boundaries play a role for the material strength and cyclic fatigue resistance [33], and hence their prevention is important in electronic devices. Another type of two-dimensional defect is the stacking fault, where the stacking order of the crystal layers changes. This is common for close-packed structures, which can have a hexagonal (hcp=ABAB..) or cubic (ccp=fcc=ABCABC..) symmetry. A stacking fault could here look like ABAB**C**ABAB. As silicon carbide can occur in many crystal structures (see polytypism in section 2.1.2), here stacking faults can lead to a mixture of polytypes. For SiC diodes a stacking fault can cause a decrease in performance as the Schottky barrier height and breakdown voltage are diminished [34]. Alternatively, stacking faults may act as luminescence centers [35]. To get rid of this kind of defect, grain growth at elevated temperatures can be applied [36].

One-dimensional defects

Linear, one-dimensional defects are mostly dislocations. They can either be edge or screw dislocations. Edge dislocations are like a half plane being inserted in the crystal, so that on either side the crystal looks normal. Only in the vicinity of the end of the half plane, the layers next to the half plane bend around the edge, and lead to this linear dislocation. Screw locations also have a linear dislocation line, around which the atoms are displaced in a helical arrangement. A special type of screw dislocation in SiC are micro pipes, which have an open hollow core. They were a severe issue for power electronics in the past, as they reduce the device performance. But today the micro pipe density is sufficiently reduced, that they are not a real problem any more [37].

Zero-dimensonal defects

Due to their limited extension of up to only few atom sizes, zero-dimensional defects are also called point defects. They can be discriminated into two subspecies:

An *extrinsic* defect is an impurity which isn't among the crystal components. This impurity can sit at a lattice position instead of a crystal atom (substitutional), or it can hold a position in between lattice sites (interstitial). The most famous example for that case are dopants, and here it is obvious, that such impurities can be a requirement for the asked-for properties (like color or conductivity) of the material.

If the point defect is *intrinsic*, there is no foreign atom involved in the defect structure. The most important types among these are:

An interstitial atom is not positioned on a lattice site.

A vacancy is an empty lattice position, where an atom is missing. Vacancies are also called **Schottky** defects.

A Frenkel defect is a still bound pair of interstitial and vacancy.

An antisite can only occur in compounds, when one atom sits on the *wrong* position, so on the lattice site of the other kind of atom. In SiC this can be either a carbon atom on a silicon spot (C_{Si}) or a silicon on a carbon position (Si_C).

Combinations thereof are also possible, like divacancies V_{Si}-V_C or vacancy-antisite pairs, e.g. V_{Si}-Si_C or vacancy-impurity complexes. Not only the variety of point defects is immense, but they come up with different charge states. Additionally, each defect's properties also vary with the SiC polytype.

Point defects can form already during growth, but they can also be introduced via post-growth particle irradiation (see Chapter 4.1). The latter treatment is preferable, as the radiation introduced damage leads to more control over defect type and density.

2.2.2. Color centers and their application

The presence of point defects leads to additional energy levels within the band gap of the host crystal. Hence, sub-bandgap light can be absorbed, which often leads to a changed color of the crystal. These point defects are therefore also called color centers. For example Al_2O_3 can occur as blue sapphire due to Fe^{2+} or Ti^{4+} ions, but Cr^{3+} ions dye the Al_2O_3 ruby red. Also the NV-center in diamond, consisting of a substitutional nitrogen and an adjacent vacancy, is a color center, giving the transparent diamond a yellow-brown opaqueness. The optical properties make color centers accessible with optical spectroscopy and these defects are suitable for different applications, some of which are described in the following.

Single photon source

A semiconductor with a color center can serve as a single photon source, as the defect can emit indistinguishable single photons on demand with a high efficiency and small probability of multiple photon emission per pulse. This is necessary for photonic quantum technologies like secure communication, quantum information processing and quantum metrology [38].

The prerequisite is to produce and address single centers, which is feasible in diamond since middle of the 1990s. A review about the fabrication of single optical centers in diamond by Orwa et al. can be found in [39]. An overview over diamond-based single photon emitters is provided by Aharonovich et al. [40]. Mostly optical excitation is used, but also electrically driven single photon emission from a NV-center at room temperature was successful [4, 41]. Other centers in diamond can as well be single photon emitters, like the SiV-center (substitutional silicon and adjacent vacancy) [42]. But also in SiC, a single photon source based on the carbon antisite-vacancy pair, optically driven at room temperature [43] has been reported.

Bioimaging applications

Another application for color centers is bioimaging. Here, the defects have to be embedded in nanometer-sized crystals, which can be incorporated in living cells or organisms. The fluorescence is then used as marker to track the cell movement or development. Especially nanodiamonds can be produced and functionalized very well, as described in an overview by Krueger [44]. Stable nanodiamonds even down to molecular scale can contain luminescent centers [45]. McGuiness et al. showed that the magneto-fluorescent NV can be used for quantum measurement and orientation tracking in living cells [10].

Due to diamond-like properties of silicon carbide (chemical inertness, non-toxicity), it is also suitable for biological use, and nanocrystals can as well be produced. Emission, even from a single carbon-antisite vacancy pair defect has been observed in nanoscale SiC particles [46]. Investigations in our group showed not only emission from silicon vacancies in silicon carbide nanocrystals, but also optical alignment of these defects [47], which is topic of chapter 7.2.

Nanosensing applications

Furthermore, color centers are highly promising for nanosensing applications. Nanosensing means the *local* measurement of a physical quantity. The principle of nanosensing is based on the optical readout of the spin resonance frequency, which may be sensitive to crystal strain, temperature, electric or magnetic field. This sensing technique can potentially allow for monitoring neuron activity, imaging of single proton spins in complex molecular systems and measuring the heat produced by chemical reactions inside living cells. Here again the NV-center in diamond is suitable for NMR spectroscopy [8, 9] or (nanoscale) magnetometry [48, 49, 50]. In our group, we also found several, separately addressable spin centers in the same SiC crystal to be suitable as sensors for magnetic field or temperature [51]. One of them exhibits a giant thermal shift at room temperature, which can be used for thermometry applications. Contrarily, a uniaxial spin-3/2 defect in hexagonal SiC is characterized by nearly temperature independent axial crystal fields, allowing for vector magnetometry of weak magnetic fields in the mT range. Particularly, the silicon vacancy center in 4H-SiC allows for measurement the magnetic field strength, as well as reconstruction of the magnetic field orientation with respect to the symmetry axis of the crystal [52].

2.2.3. Spin defects

Special attention among these optically active color centers deserve the ones carrying a net electron spin. This makes them also accessible for spin manipulating techniques, like EPR (Electron Paramagnetic Resonance) or ODMR (Optically Detected Magnetic Resonance)[1]. The nanosensing applications just described above already indicate that the spin property of some color centers can be optically detected. Another ascending field of applications, where this property can be exploited, are so called *quantum applications*. Here, spin defects in semiconductors are very promising candidates, especially for room temperature utilization. This will be described in this section, followed by a discussion of the advantages of the silicon vacancy in SiC.

[1]The principle of the ODMR technique is explained in chapter 3.2.

Quantum applications

Spin defects in semiconductors are suitable for quantum applications [53, 54] like quantum metrology, quantum computing and communication as well as spintronics. Although there's much effort in this research field, the to date "quantum computers" consist of only a few qubits (the equivalent to a classical bit) and can just do dozens of quantum operations [2]. A promising qubit candidate has to fulfill the DiVincenzo criteria [3]:

- Scalability: It should be possible to easily (up)scale the number of qubits.
- Initialization: There must be a tool to set the qubit(s) into a defined state to start with.
- Decoherence time: The time, after which the qubits start to dephase should be sufficiently long.[2]
- Set of quantum gates: This allows for operations upon the qubits' state(s).
- Measurement: There has to be a possibility to read out the state(s) after application of the gates.

Quantum operations succeeded at least on small laboratory scales for several different qubit systems, like quantum dots [55], superconducting Josephson junctions or single trapped ions/atoms [56]. Each system has its own advantages and drawbacks, so these different approaches should not be seen as competition but rather as complement. A good overview is provided by Ladd in [57].

In contrast to most other approaches, the spin carrying color centers in semiconductors can be operated at room temperature. The realization of such a system with a long spin coherence time T_2 of 2 seconds was shown by Tyryshkin et al. on phosphorus donors in silicon [58]. However, the most prominent example in this field is the NV-center in diamond. The first observation of single NV-centers and their magnetic resonance at room temperature [59] set a milestone. Up to now, many publications on coherent control and entanglement of NV-centers have been published [60, 61, 62, 63]. The most recent publications show e.g. quantum teleportation between NV quantum bits separated by 3 meter distance [64], an experimental realization of universal geometric quantum gates with a NV-center coupled to a nearby ^{13}C nuclear spin [5] or quantum error correction in a hybrid NV electron- and nuclear-spin register [65]. Despite this huge progress for NV-centers in diamond, the large scale production of diamond is challenging. In the ongoing search for alternatives [66], silicon carbide is

[2]The decoherence time depends also on the required time to initialize them and to perform an operation.

getting increased attention [67, 68, 69] as there are eligible qubit candidates in SiC, like the carbon-antisite vacancy pair [46], the neutral carbon–silicon divacancy [12, 70] and the silicon vacancy [11, 71, 72, 73]. Regarding the variety of possible defects in SiC, a good overview is provided by Castelletto et al. [74].

Advantages of the silicon vacancy in SiC

Obviously, several applications of spin defects, especially the NV-center in diamond, have been already demonstrated. So the need of research on other spin defect systems is not self-evident. The silicon vacancy (abbreviation: V_{Si}) in SiC however has several advantages that makes its investigation worthwile.

- The production technology of SiC is already established in industry and wafers are produced in large scale.
- SiC can be easily implemented in or used for semiconductor electronics, in contrast to the isolating diamond. The thermal conductivity and the breakdown field of SiC is higher than in silicon (compare table 2.1 in section 2.1.1), making SiC devices very robust.
- The polytypism of SiC allows more choices of material parameters and due to the bi-atomic composition, a bigger variety of -even intrinsic- defects is possible. Especially in the field of nanosensing, V_{Si} can be used for magnetic field sensing, while another defect *in the same device* can measure the temperature [51].
- The color center V_{Si} is an intrinsic defect unlike the NV-center in diamond, which needs the implantation of nitrogen. Hence the creation is far easier and can e.g. be done in a state-of-the-art transmission electron microscope [75].
- The V_{Si} emission is in the near infrared (NIR) from around 860 nm up to 1000 nm. Although not exactly matching the very commonly used original fiber-optic telecommunication window (O band, 1260-1360 nm), the attenuation for the V_{Si} emission is far lower than the visible (VIS) range, where most of the investigated color centers emit. Also for bioimaging use, NIR is advantageous over VIS, as biological tissue autofluoresence [76] and attenuation [77] are lower in the NIR.
- In contrast to the NV-center in diamond [78], the V_{Si} shows no blinking [11].
- Defects occupying several inequivalent lattice positions are energetically slightly different. Selective resonant optical excitation of only one type of the V_{Si} is possible. The spectral linewidth of such an isolated line can be as small as 2 μeV [72].

- As the $\frac{3}{2}$ spin state of the silicon vacancy is *half-integer*, the Kramers theorem holds: Without external fields, the spin sublevels $+\frac{1}{2}$ and $-\frac{1}{2}$ as well as $+\frac{3}{2}$ and $-\frac{3}{2}$ are degenerate. In particular, the energy levels are more robust agains strain fluctuations than spin = 1 systems like the NV-center in diamond, whose energy levels are subject to electric and strain fields [79, 80].
- An optically induced population inversion of the ground state can lead to stimulated microwave emission [81], with which a MASER working at room temperature could be established.

2.3. Silicon vacancy in SiC

The defect investigated in this thesis is the silicon vacancy (V_{Si}), and its particular advantages regarding applications have been already named in the previous section. This section describes the vacancy's physical properties more closely.

As the name implies, a V_{Si} in SiC is a missing silicon atom. This is schematically shown in figure 2.3 for a V_{Si} in a 4H-SiC unit cell.

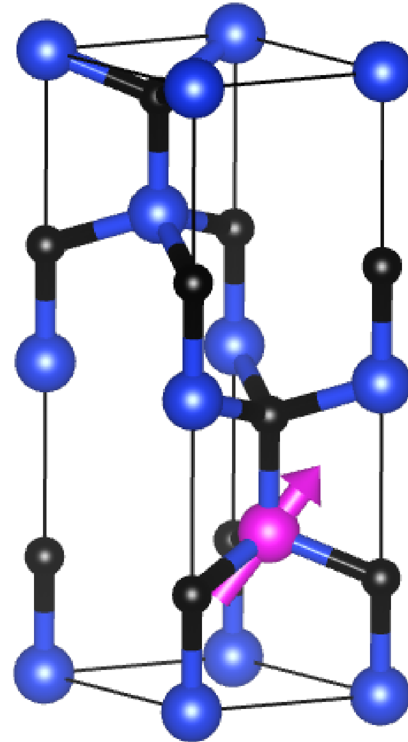

Figure 2.3.: Silicon vacancy in SiC. Spatial model of a V_{Si} (magenta) in a 4H-SiC unit cell. The defect is tetragonally surrounded by four carbon atoms (black) and the arrow symbolizes the spin. Drawing produced with VESTA [28].

Discrete energy levels within the band gap of SiC can be associated with the V_{Si} and it has a net electron spin. These properties make the defect sensitive to optical and spin-sensitive measurements.

Nevertheless the identification remained challenging for several decades: First calculations of the electronic structure of single vacancy centers in SiC were done by Larkins and coworkers already in 1970 [82]. The experiments in the 1970s gave some hints to, but no clear assignment of the silicon vacancy: Balona and Loubser [24] performed Electron paramagnetic resonance (EPR) experiments on irradiated 6H- and 3C-SiC and tentatively ascribed three spectral features to certain vacancies. Hagen and Kemenade observed infrared luminescence in 15R- and 6H-SiC, but couldn't identify the emission lines. The identification of the silicon vacancy in 6H-SiC succeeded in 1981 by Vainer and Ilyin via EPR experiments [83]. In 1990, Itoh and coworkers identified the T1 center, which has already been observed since the '70s (e.g. in [24]), in 3C-SiC to be the silicon vacancy [84]; and in 1995, the same group correlated this EPR signal with a photoluminescence emission at 1.913eV [85].

2.3.1. Energy level model

Jansén, Gali and coworkers performed theoretical density functional theory calculations for the (negatively charged) silicon vacancy in 4H- and 6H-SiC and proposed

the following model for the defect [86]. The energy levels of this model for the V_{Si}^- are schematically shown in figure 2.4.

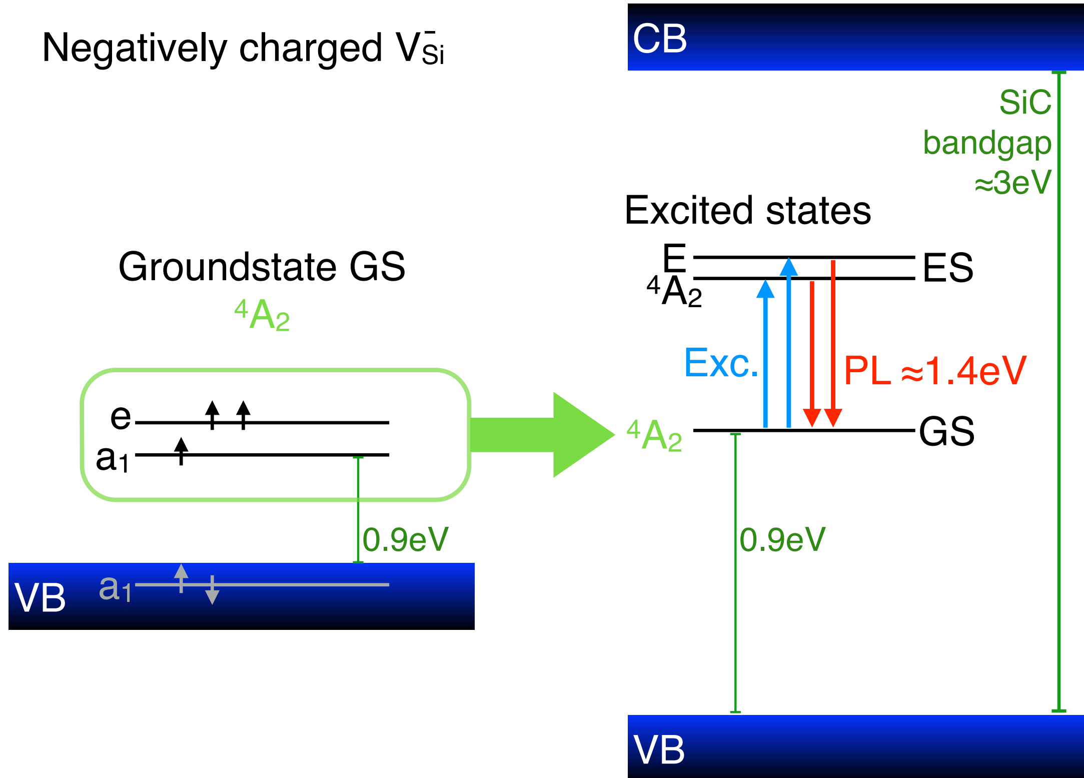

Figure 2.4.: Energy level scheme of the silicon vacancy in silicon carbide. Left: Ground state model for the V_{Si}^- in 4H- and 6H-SiC, adapted from [86]. **Right:** The ground state (GS) levels can be reduced to one $^4A_2$ level. There are excited states (ES) of the defect within the bandgap of SiC. Optical excitation from the GS to the ES is possible and subsequently results in photoluminescence (PL) emission. Some energy values are also denoted. Abbrevations: VB: valence band, CB: conduction band of SiC.

From the former bonds to the four next-neighbor carbon atoms, four dangling bonds point to the vacant lattice position. Due to the lack of p-electrons in the carbon atoms, the dangling bonds around the V_{Si} are strongly localized at the neighboring C atoms and don't overlap. The C atoms do not relax towards the vacant space, but maintain the C_{3v} symmetry, basically independent from the charge state or site (k or h). According to group theory and the character table for the C_{3v} symmetry , the dangling bonds form two a_1-levels and one doubly degenerate e-level. If we include the electron spin, then the a_1-levels are of degeneracy 2 and the e-level is of degeneracy 4. The lower $a_{1'}$-level is resonant with the SiC valence band and slightly below the valence band edge. The other a_1 and e are very close (e is higher), and lie within the bandgap. The levels are around 0.9 eV above the valence band edge for a negatively charged V_{Si}^-, which will

be considered in the following. In this case, five electrons are distributed among the energy levels $a_{1'}$, a_1 and e. There are different possible multiplets, but the only one allowing for a high spin state is a fully occupied $a_{1'}$-level ($a_{1'}^2$). Therefore the ground state is expected to be a quadruplet $^4A_2 = a_{1'}^2 a_1^1 e^2$. Additional measurements in [86] show the existence of excited states (still below the conduction band), as the defect can be optically excited and shows sharp photoluminescence emission lines around 1.4 eV.

2.3.2. Photoluminescence

The defect can be excited optically and subsequently shows photoluminescence around 1.4 eV. This emission consists of a sharp line, which is the direct transition without phononic contribution (in the following called ZPL (Zero Phonon Line)) and the phononic sideband, which is schematically depicted in figure 2.5. With respect

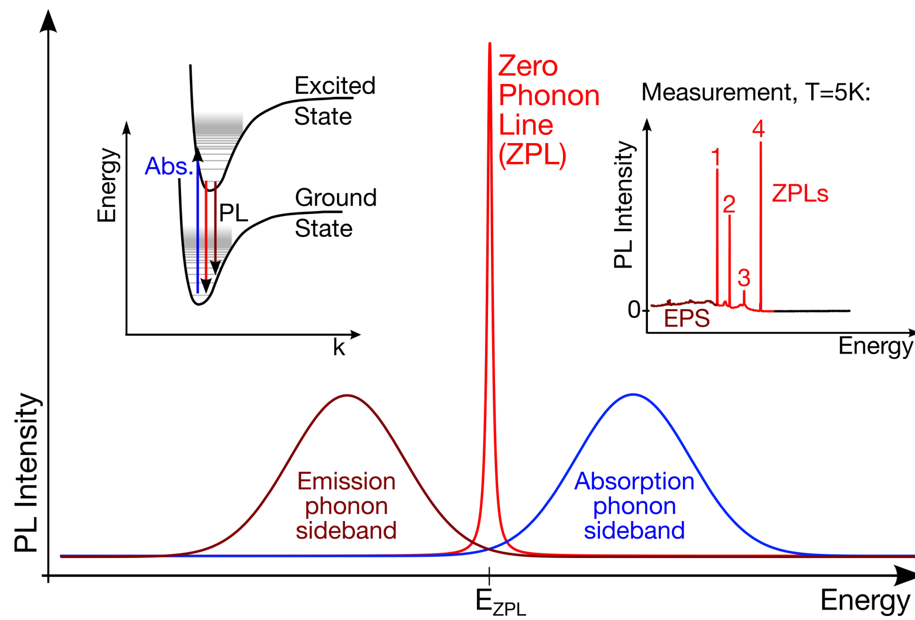

Figure 2.5.: Zero phonon line and phonon sidebands. The ZPL is the direct absorption/emission line and therefore sharp and characteristic for a specific defect (at T=0). Due to lattice phonons, each individual defect shifts its ZPL according to the Franck-Condon principle (see left inset). For an ensemble of defects, this leads to the absorption/emission phonon sidebands. *With permission adapted from [87, Figure 5.4].* The right inset shows a PL measurement of a bulk SiC sample with defect ensembles at T=5K. Four numbered ZPLs show the presence of four different kinds of defects. Their phonon sidebands cannot be distinguished and add up to one emission phonon sideband (denoted with EPS).

to the ZPL, the phononic sideband is blue shifted in absorption but red shifted in emission, both due to absorption/emission to a higher vibronic excited/ground state, according to the Franck-Condon principle. The ZPL position is unique for each

inequivalent lattice position in a certain polytype. Wagner et al. [88] and Orlinski et al. [89] investigated the electronic structure for the silicon vacancy in 4H-SiC and 6H-SiC, and their reported ZPL energies are summarized in table 2.2.

SiC polytype	position	energy [eV]	λ [nm]	ZPL name
4H	k	1.438	862	V1
	h	1.352	917	V2
6H	k_1	1.433	865	V1
	k_2	1.398	906	V3
	h	1.368	887	V2

Table 2.2.: ZPL energies and respective wavelengths for the silicon vacancy in 4H- and 6H-SiC. The abbrevations for the positions are k for a cubic lattice position, and h for a hexagonal site. Values are taken from [88] and [89].

2.3.3. Spin state

As already mentioned, the silicon vacancy is a defect with a nonzero electron spin. More precisely, as the charge state of the defect can be different, also the defect's spin state can vary. This is summarized in table 2.3.

defect notation	V_{Si}^{+}	V_{Si}^{0}	V_{Si}^{-}	V_{Si}^{2-}
charge state [e]	+1	0	-1	-2
spin m_s [$\hbar$]	$\frac{1}{2}$	1	$\frac{3}{2}$	1

Table 2.3.: V_{Si} charge and spin states. Possible silicon vacancy charge configurations and respective spin states. From [90].

The charge/spin state of the silicon vacancy was controversially debated in the last two decades, which is just briefly sketched here. For a detailed description, I refer to [87]. Wimbauer et al. identified the V_{Si}^{-} to be spin $\frac{3}{2}$ with electron nuclear double resonance (ENDOR) experiments [91]. In contrast, the swedish researchers around Sörman, Son and Janzén promoted a triplet state ^{3}A of the silicon vacancies in 4H- and 6H-SiC via electron paramagnetic resonance (EPR) [88, 92]. As they assigned the photoluminescence emission to a spin 1 state, they connected it to the neutral vacancy instead of V_{Si}^{-}. Therefore they called the vacancies T_{Vja}, with $j \in \{1,2,3\}$; T for triplet state and a for allowed optical excitation. Orlinski, Baranov and coworkers [89] also proved the vacancy's ground state to be of high spin. But this could still be either ^{3}A triplet state with S=1 or a quadruplet ^{4}A with S=$\frac{3}{2}$. The latter was not only favored by Wimbauer et al. but also concluded by Mizuochi and coworkers via pulsed ENDOR experiments for

the T_{V2a} in 4H-SiC [93]. This shows that there was no consensus concerning the spin state of the silicon vacancy. But one drawback of the previous experiments was, that many different defects were excited simultaneously, so it was challenging to differ between their contributions to the signal.

Therefore in our group we performed measurements under *double radio optical resonance* conditions, which allows for selective excitation of a specific type of defect [72]. In a cooperation with the group of Prof. Baranov, we could unambiguously prove the spin state $\frac{3}{2}$ for the V2 (hexagonal) and V3 (2nd cubic) silicon vacancies' ground state in 6H-SiC and for V2 (hexagonal) in 4H-SiC [81]. Therefore, the following considerations are for the negatively charged silicon vacancy with electron net spin of S=$\frac{3}{2}$, for simplicity written as $\mathrm{V_{Si}}$.

2.3.4. The zero field interaction

The spin Hamiltonian $\mathcal{H}_{spin}$ describes the energy levels (respectively level splittings) due to interactions of a spin with magnetic fields and other magnetic dipoles. In general, $\mathcal{H}_{spin}$ comprises

- Zeeman interaction of electron spin i
- Zero field interaction of electron spin i
- Nuclear Zeeman interaction of nuclear spin k
- Nuclear quadrupole interaction of nuclear spin k
- Exchange and dipolar interaction between electron spins i and j and
- Hyperfine interaction between electron spin i and nuclear spin k.

The nuclear quadrupole interaction can be disregarded, as its relevance is limited to interactions with $I > \frac{1}{2}$ nuclei, which doesn't hold for both silicon and carbon. The hyperfine interaction and the nuclear Zeeman effect are weak and in the measurements of this thesis not resolved. Therefore this term can also be omitted. The contributions of the electron-exchange and dipolar interactions are not yet investigated. They may play a role, as the V_{Si} is a system with effectively three electrons in close, atomic-scale proximity.

But it turned out that the remaining contributions, the **zero field interaction** (ZFI)[3] and the electron Zeeman term, sufficiently describe the behavior of the electron system. Therefore, the exchange and dipolar interactions are here also omitted and the

[3] The ZFI is an anisotropic magnetic dipole-dipole interaction of the participating electron spins. It may additionally have some contribution of spin-orbit coupling or crystal field [94].

now simplified spin Hamiltonian for the V_{Si} in SiC contains the ZFI and the Zeeman interaction:

$$\mathscr{H}_{\text{spin}} = D\left(\hat{S}_z^2 - \tfrac{1}{3}\hat{S}^2\right) + E\left(\hat{S}_x^2 - \hat{S}_y^2\right) + g\mu_B \vec{B}_0 \circ \hat{S} = \tag{2.1}$$

$$= D\left(\hat{S}_z^2 - \tfrac{1}{3}S(S+1)\right) + E\left(\hat{S}_x^2 - \hat{S}_y^2\right) + g\mu_B \vec{B}_0 \circ \hat{S}. \tag{2.2}$$

Here, g is the electron g-factor (Landé factor), μ_B the Bohr magneton, $\vec{B}_0 = (B_{0x}, B_{0y}, B_{0z})^T$ an externally applied magnetic field. The spin operator of the spin $\vec{S}$ is $\hat{S} = (\hat{S}_x, \hat{S}_y, \hat{S}_z)^T$ and S=$|\vec{S}| = \frac{3}{2}$.

The ZFI is described by the zero field splitting (ZFS) parameters D and E. D describes an axial anisotropy, lifting the degeneracy between the different $|m_s|$ sublevels. According to literature, D is positive and E « D due to uniaxial symmetry in the ground state [92, 89].

With the assumption that $\vec{B}_0$ is along the spin quantization axis (i.e. $\vec{B}_0 = (0, 0, B_0)^T$), the matrix form of this Hamiltonian can be given as:

$$\begin{pmatrix} \frac{3}{2}g\mu_B B_0 + D & 0 & \sqrt{3}E & 0 \\ 0 & \frac{1}{2}g\mu_B B_0 - D & 0 & \sqrt{3}E \\ \sqrt{3}E & 0 & -\frac{1}{2}g\mu_B B_0 - D & 0 \\ 0 & \sqrt{3}E & 0 & -\frac{3}{2}g\mu_B B_0 + D \end{pmatrix} \tag{2.3}$$

The eigenvalues (energy levels $\mathscr{E}$) of $\mathscr{H}_{\text{spin}}$ for the respective eigenstates are:

$$\begin{aligned} &\tfrac{1}{2}g\mu_B B_0 + \sqrt{(g\mu_B B_0 + D)^2 + 3E^2} && \text{for } m_s = \tfrac{3}{2} \\ -&\tfrac{1}{2}g\mu_B B_0 + \sqrt{(g\mu_B B_0 - D)^2 + 3E^2} && \text{for } m_s = \tfrac{1}{2} \\ &\tfrac{1}{2}g\mu_B B_0 - \sqrt{(g\mu_B B_0 + D)^2 + 3E^2} && \text{for } m_s = -\tfrac{1}{2} \\ -&\tfrac{1}{2}g\mu_B B_0 - \sqrt{(g\mu_B B_0 - D)^2 + 3E^2} && \text{for } m_s = -\tfrac{3}{2}. \end{aligned}$$

The energy levels in an external magnetic field are depicted in figure 2.6 for different parameter values. In case E=0, the energy levels can be clearly assigned to certain m_s sublevels, which is denoted in the top left graph of figure 2.6 at the branches. But if E is not negligible, level anticrossing and state mixing occurs.

In case of no external magnetic field ($B_0 = 0$), there are no Zeeman terms[4] and the energy levels $\mathscr{E}$ of the states $|m_s\rangle$ splitting yields $\mathscr{E}(|\pm\frac{3}{2}\rangle) = +\sqrt{D^2 + 3E^2}$ and $\mathscr{E}(|\pm\frac{1}{2}\rangle) = -\sqrt{D^2 + 3E^2}$. This means that a deviation from uniaxial symmetry, resulting in non-

[4] Here, the splitting due to earth magnetic field (B_{earth} ≈50 µT) can also be neglected.

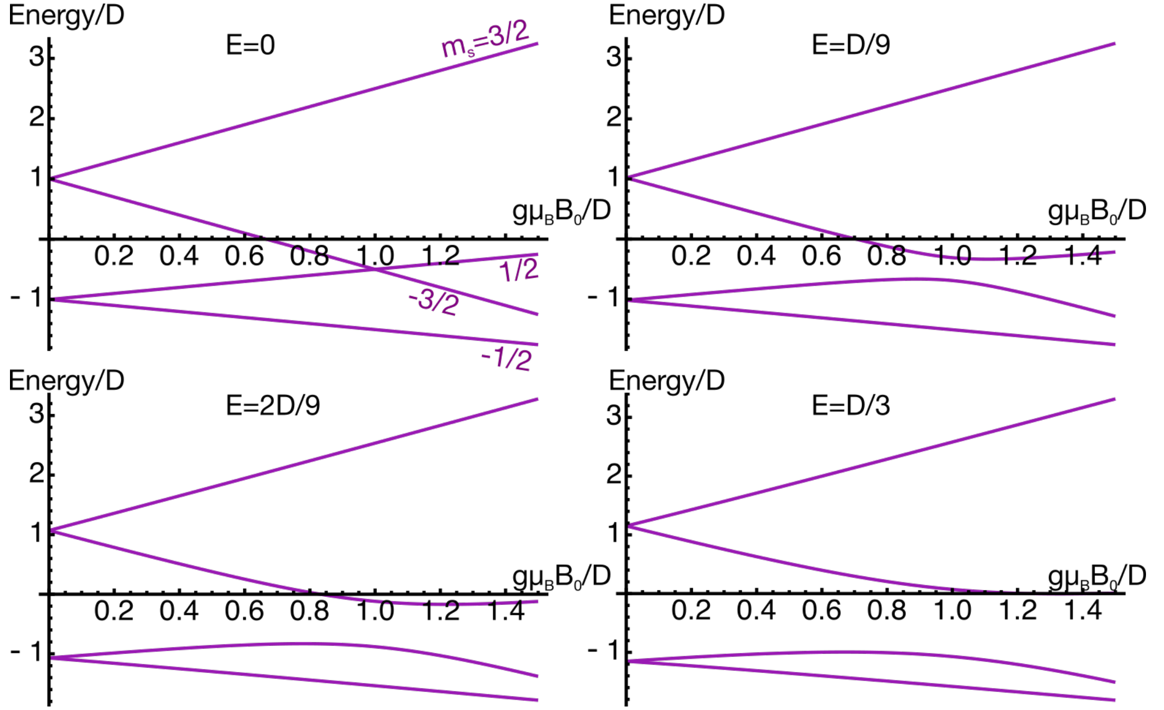

Figure 2.6.: Energy levels of a spin S=$\frac{3}{2}$ system with ZFS and Zeeman splitting. The energy diagrams show the energy levels in the case $\vec{B}_0||$z-axis versus the magnetic field. Both axes are shown relative to the value of D. The value of E is varied from 0 to $\frac{D}{3}$, the respective value is written in the graph. In zero magnetic field and for D≠0, E«D, the $m_s = \pm\frac{3}{2}$ sublevels are split from the $m_s = \pm\frac{1}{2}$ level by 2D (see top left graph).

vanishing E parameter, does not lift the degeneracy of the $\pm\frac{3}{2}$ or $\pm\frac{1}{2}$ states at zero magnetic field. The resulting splitting between the $|m_s| = \frac{3}{2}$ and $|m_s| = \frac{1}{2}$ is $2\sqrt{D^2+3E^2}$ ≈2D for E«D.

Note that the splitting occurs in the ground state as well as in excited states, but in general the D parameters will be different. Hence, it would be correct to write D_{GS} or D_{ES}. This distinction is omitted here for simplicity, as the here accessible D is that of the GS.

The fact that the silicon vacancies comprise a ZFS is still discussed. In some cw EPR measurements, no silicon vacancy related ZFS could be observed [71, 89, 91], but other measurements observe a ZFS [95]. This indicates a complex behavior due to the variation of the level splitting with different orientation of the c-axis with respect to the microwave B_1-field vector. To account for this non-isotropy, the general ZFI term $\mathscr{H}_{ZFI} = \hat{S}^T \mathbf{D} \hat{S}$ is written with a ZFS-tensor **D**, containing the ZFS parameters D and E (compare $\mathscr{H}_{spin}$ matrix form 2.3).

Baranov proposes for the observed vacancy with ZFS a model with an interaction of a V_{Si}^- with a neutral carbon vacancy, leading to this ZFS [73]. Zywietz in contrast calculates for the V_{Si}^- in 4H-SiC a splitting of the t_2-vacancy level, which is threefold degener-

ate in the T_d symmetry of 3C-SiC [96]. This means that the local point-group symmetry is already reduced to C_{3v}, which allows for a ZFS. Mizuochi et al. experimentally reveal C_{3v} symmetry for the V_{Si}^- in 4H- and 6H-SiC, instead of the formerly assumed T_d symmetry [91]. But they also see a V_{Si}-related center (T_{V2a}), whose distortion – manifested in the ZFS – *“is likely to be caused by a perturbation of the crystal field, presumably by the presence of an accompanying impurity or defect located at some distance along the c-axis.”* [93, p.1]. So although the spin state of the vacancy is revealed, there are still many open questions and the discussion is ongoing.

2.3.5. Optical cycle model

As already mentioned in subsection 2.3.2, the V_{Si} can be optically excited and shows photoluminescence, which turns out to be spin-dependent. To explain the excitation behavior, at least a third energy level MS (metastable state) between the excited state ES and the ground state GS has to be considered. This is in analogy to the energy scheme of the NV-center in diamond, were a three-level model describes the excitation dynamics very well [97, 98]. Eventually, a fourth energy level $|4\rangle$ that can be accessed via optical laser excitation from the metastable level, may participate in the pumping cycle. The possibility to depopulate the *shelving* state MS to a state $|4\rangle$ can be considered by introducing an effective deshelving rate (see section 5.2).

The general pumping cycle however is in principle the same for both models, depicted in figure 2.7. The optical excitation (blue arrows) takes place from the GS to the ES. Depicted is the resonant case, but the phonon-assisted excitation followed by non radiative relaxation into the lowest ES also takes place. Some time later, the system relaxes into the GS again. There are two pathways for the relaxation: Either a radiative recombination via emission of a photon (PL, red arrows) or a nonradiative process via the metastable level MS (dashed arrows). The excitation and radiative recombination are spin-conserving, but this doesn't hold for the recombination via the MS. Here, *intersystem crossing* can occur, i.e. transitions between states with different spin quantum numbers.

Spin alignment

As denoted in figure 2.7, the spinsublevels $\pm\frac{3}{2}$ and $\pm\frac{1}{2}$ of the quadruplets are separated by the *zero field splitting* (ZFS) (see also figure 2.6 and explanation in the previous section 2.3.4). Remarkably, the recombination rates strongly depend on the spinsublevel. This leads to overpopulation of one GS spinsublevel compared to the other spinsub-

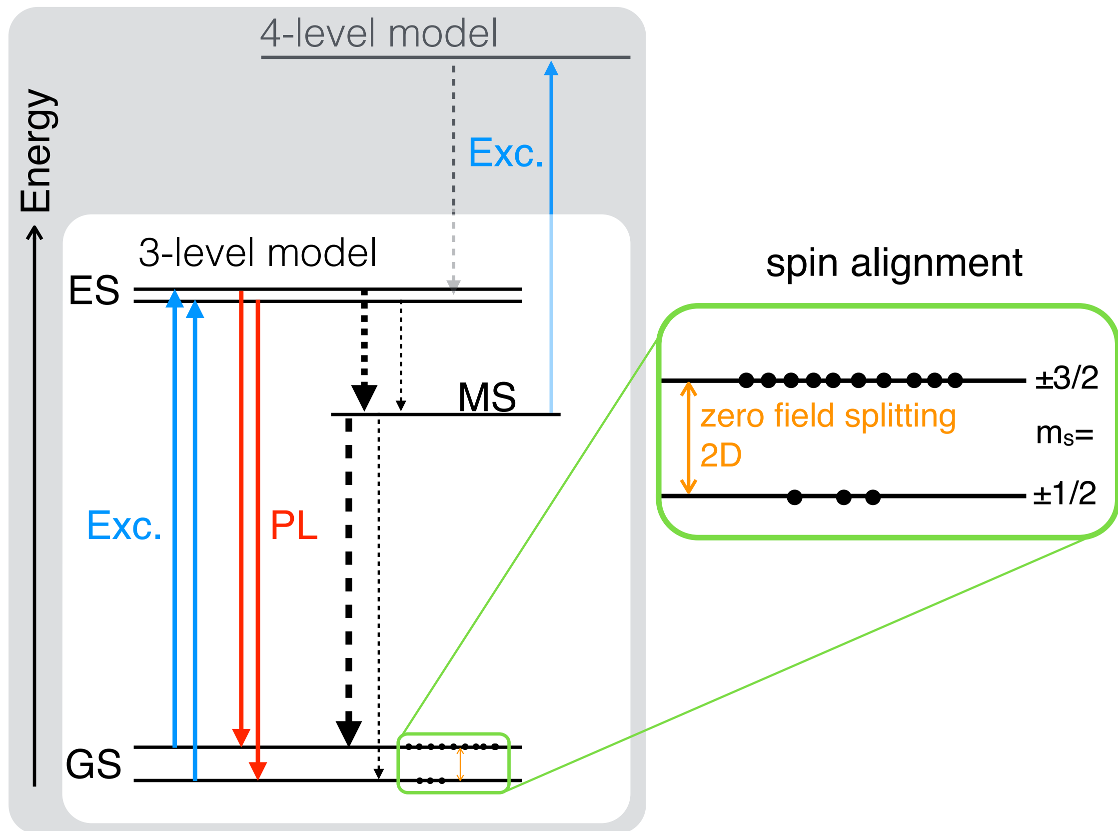

Figure 2.7.: Optical cycle models of V_{Si} and spin alignment. Effective 3-level model with ground state GS, excited state ES and metastable state MS and effective 4-level model with an additional level, that is accessible via optical excitation of the MS. The excitation and radiative recombination are drawn with solid lines, the non-radiative pathways are dashed, with thickness denoting different transition rates. The magnified green box shows the ZFS for the GS and illustrates the *spin alignment* after optical pumping with different numbers of filled circles.

levels. This phenomenon is called *spin alignment*. Which spinsublevel overpopulates depends on the polytype and also on the lattice site of the vacancy.

For example after several excitation cycles of the hexagonal position V_{Si}(V2) in 6H-SiC, the majority of the V_{Si} prefers the $m_s = \pm\frac{3}{2}$ spinsublevel in the GS. This means this optical pumping initializes a certain spinsublevel and leads here to a population inversion in the GS, as the $m_s = \pm\frac{1}{2}$ is energetically lower than the $m_s = \pm\frac{3}{2}$ spinsublevel. This gives a promising starting point for various quantum applications, like stimulated microwave emission for a MASER [81].

2.3.6. Photon statistics

The silicon vacancy can be regarded as a light source. A light source can be characterized by its statistical properties of the emitted photon stream. In general, three dif-

ferent types of statistics can occur: *Poissonian, super-Poissonian* and *sub-Poissonian*. The latter cannot be explained with classical theory of light, hence providing a direct evidence of the photon nature of light. A detailed treatment is beyond the scope of this thesis, but a clear insight into photon statistics can be found in Quantum Optics by Fox [99, Ch. 5]. Figure 2.8 exemplarily shows the emission time traces for different light sources.

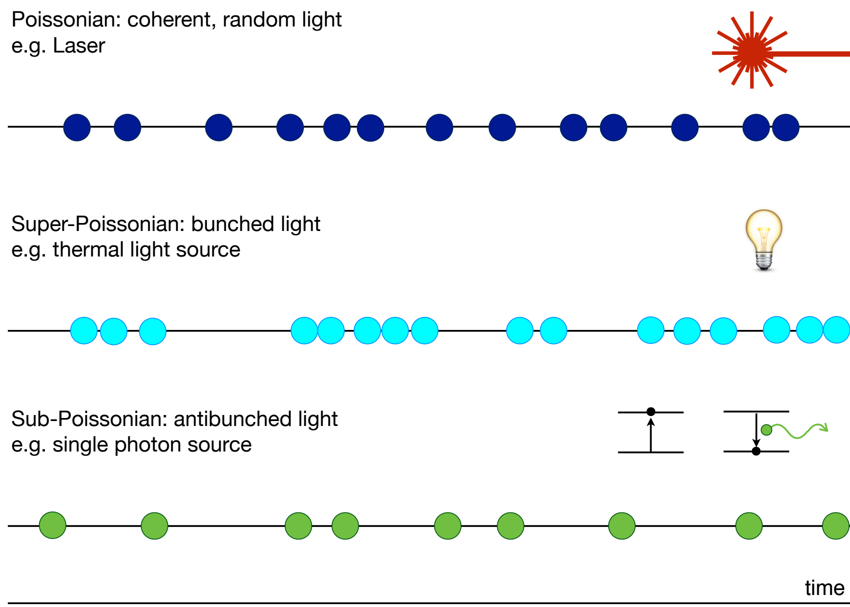

Figure 2.8.: Emission time traces for different light sources with different photon statistics. The random emission of a coherent light source like a laser has a Poissonian statistic (top). A thermal light source like a light bulb has super-Poissonian statistic with typical bunching behavior (middle). A quantum mechanical single photon emitter has sub-Poissonian statistic and often shows antibunching (bottom).

An important photon statistical feature is the distribution of delay times between emission of subsequent photons. Imagine an emitter that has complete uncorrelated photon emissions, e.g. a coherent laser emission. Then after emission of one photon at time 0, the probability to have another emission at time τ is the same for every time τ (i.e. there's no distinct time). If on the one hand an emitter often emits several photons at one time, there's a bigger probability to measure the second photon at small times than at larger times. Such a behavior is called *bunching* and holds for e.g. thermal light sources (figure 2.8, middle). On the other hand, a single photon source (figure 2.8, bottom) cannot emit two photons at the same time, so the emission probability of a second photon at time $\tau = 0$ is zero.

A mathematical description and distinction of the emission statistics can be done with the second order correlation function.

Second order correlation function

The joint probability for the detection of a photon at time $\tau = 0$ (without loss of generality) and the detection of a subsequent photon at some later time τ is related to the second order correlation function $g^{(2)}(\tau)$. The derivation and detailed treatment of $g^{(2)}(\tau)$ can be found in [99, Ch. 6]. Here, a look at some general properties of $g^{(2)}(\tau)$ will be sufficient. Figure 2.9 shows exemplarily the different $g^{(2)}(\tau)$ functions for different photon statistics.

In a stationary case the second order correlation function is

$$g^{(2)}(\tau) = \frac{\langle I(t)I(t+\tau)\rangle}{\langle I(t)\rangle^2} \tag{2.4}$$

with the intensity amplitude $I(t) = \vec{E}^*(t) \circ \vec{E}(t)$ of the electromagnetic wave with (complex) electric field strength $\vec{E}(t)$ and $\langle \ldots \rangle$ denoting the statistical average.

Classical light source

If the light emitter can be treated classically, the *classical inequalities* hold:

$$g_c^{(2)}(0) \geq 1 \tag{2.5}$$

$$g_c^{(2)}(\tau) \leq g_c^{(2)}(0) \forall \tau \tag{2.6}$$

furthermore one has

$$\lim_{\tau \to 0} g_c^{(2)}(\tau) = 1. \tag{2.7}$$

A special case is the *Poissonian* statistic of a light source with complete coherence, i.e. having no variance or no fluctuations. Here, for all τ it is: $g^{(2)}(\tau) \equiv 1$.

Quantum emitter

In quantum mechanical (qm) systems, the correlation function can be written with the corresponding operators:

$$g^{(2)}(\tau) = \frac{\langle \hat{I}(t)\hat{I}(t+\tau)\rangle}{\langle \hat{I}(t)\rangle^2}. \tag{2.8}$$

Nonclassical light sources break the *classical inequalities*, e.g. $g^{(2)}(0) < 1$, hence the statistic is called *sub-Poissonian*.

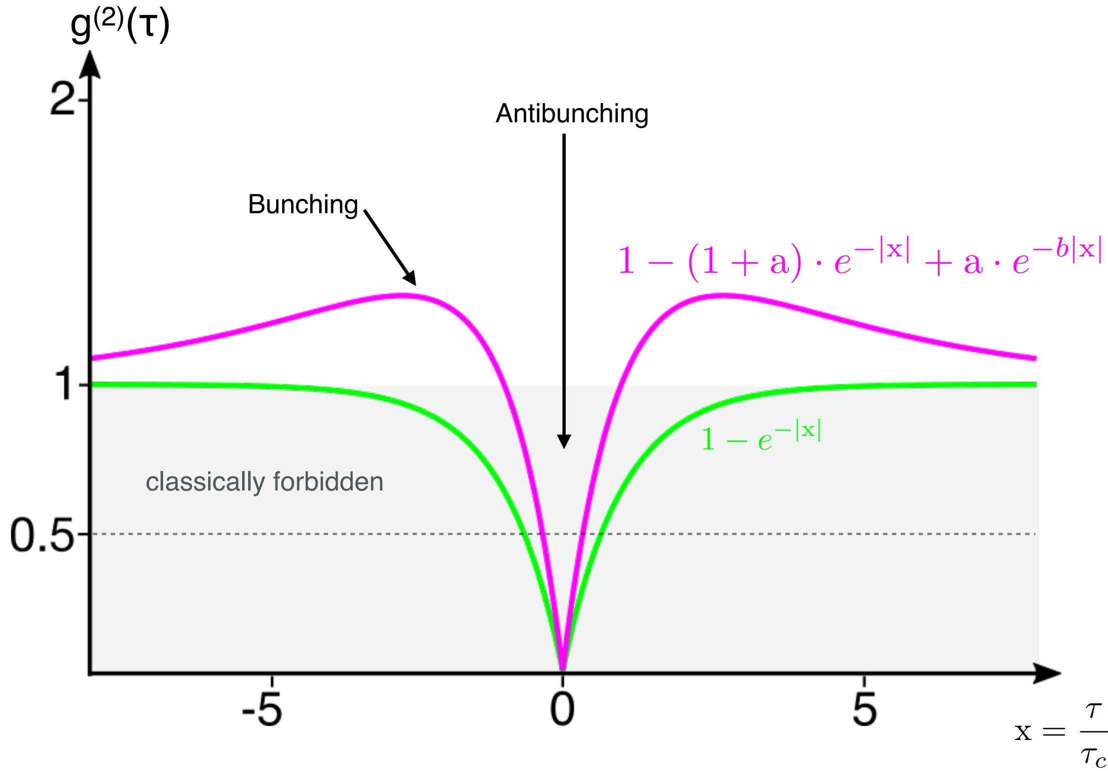

Figure 2.9.: Second order correlation function for quantum emitters. Schematic drawing of $g^{(2)}(\tau)$ function for two possible sub-Poissonian photon statistics. The used functions are written next to the respective graphs. The scale on the abscissa is $\frac{\tau}{\tau_c}$ with the characteristic coherence time τ_c (which is temperature dependent, typically ns-µs [100]). The classically forbidden region is shaded in light grey. The antibunching proofs the non-classical behavior of quantum emitters and the number n of emitters can be evaluated (here: n=1 as $g^{(2)}(0)=0$; see text for explanation). In the case with bunching (magenta curve), the fit parameter were chosen to be a=1, b=0.3.

Antibunching and bunching

If inequality 2.6 is violated, i.e. $g^{(2)}(0) < g^{(2)}(\tau)$, the system undergoes so called **antibunching**. This is a doubtless indication of a qm system. One can furthermore determine the number of qm emitters, as $g^{(2)}(0) = \frac{\langle n(n-1)\rangle}{\langle n\rangle^2}$ with the photon number observable n. Especially for a single photon emitter (n=1), it is $g^{(2)}(0) = 0$ (see figure 2.9).

But nonclassical systems may also have a **bunching** effect, meaning there are some time values τ for which $g^{(2)}(\tau) > 1$ (see figure 2.9, magenta curve). This bunching cannot be explained with a simple 2-level emitter model. Hence, a third, *shelving* state

has to be considered. Due to shelving of the direct emission from ES to GS, bursts of emissions are separated by dark intervals.

In case of a single silicon vacancy in silicon carbide, antibunching is expected, as the system is purely quantum mechanical. This behavior will be used in chapter 5.2 to proof the emission from a *single* defect. The V_{Si} correlation function also shows bunching (see also ch. 5.2), which can be explained either with a 3- or 4-level model (see optical cycle model in section 2.3.5 of this chapter).

3. Methods

Three different methods were used for this investigation of silicon vacancies in silicon carbide. Hence the first three sections of this chapter will explain for each method the underlying physical processes and technical aspects. The subsequent section describes the utilized setups and measurement equipment.

3.1. Luminescence spectroscopy

An excited system relaxes from the excited state to the ground state (or at least a lower lying state) and in doing so is emitting electromagnetic radiation, called *photoluminescence* (PL). For the V_{Si} in SiC, this is already depicted in figures 2.4, 2.5 and 2.7 of the previous chapter. The requisite to measure PL is a spectrometer with the possibility to excite the sample and a detector for the emitted light. Besides PL measurements, also *photoluminescence excitation* (PLE) measurements were performed, which is essentially the PL intensity in dependence of the excitation energy. This provides not only information on the energy levels, but gives also insight into the excitation efficiency.

Additionally, it is not only possible to excite the system optically, but also electrically, resulting in *electroluminescence* (EL). This excitation scheme employs a SiC LED-structure and will be described later in chapter 6.

Raman spectroscopy

Additionally to the PL of the V_{Si}, the SiC Raman lines are detected. Raman lines arise due to inelastic light scattering, involving lattice phonons. As the phonons are individual for a specific type of crystal, the Raman lines are an unambiguous fingerprint of each SiC polytype. This is especially useful to localize the SiC nanoparticles (see chapter 7). Explaining Raman scattering in more detail is beyond the scope of this thesis, but the interested reader may have a look at *Modern Raman Spectroscopy* by Smith and Dent [101].

3.2. Optically detected magnetic resonance

Optically Detected Magnetic Resonance (ODMR) is a spin manipulating technique for systems with spin-dependent optical transitions. ODMR technique using 10 GHz microwaves and respective magnetic fields (*full field*) is well described in [87]. Additionally to the optical excitation an *external magnetic field*, inducing a Zeeman splitting to the energy levels, is applied. Microwave radiation that is resonant with the Zeeman splitting, opens a pathway between the split spin levels and changes the population. If the optical transition rates are spin dependent, this change in spin population is reflected in a change in the observed optical transition. The ODMR contrast is the relative change in the optical transitions, e.g. in PL intensity $\frac{\Delta PL}{PL}$.

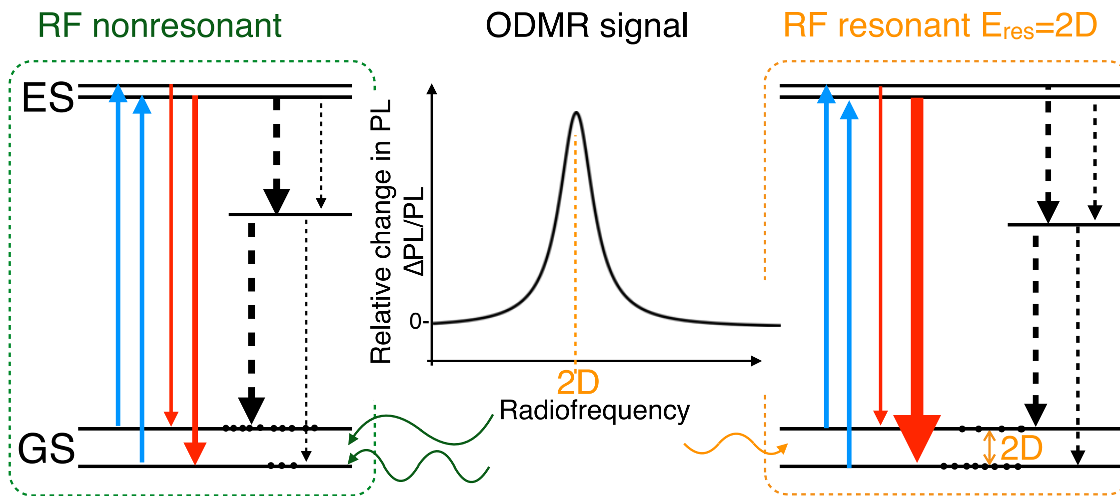

Figure 3.1.: Principle of zfODMR on V_{Si} in SiC. Additionally to optical excitation (blue arrows), radio frequencies (RF) are applied. The RF frequency is swept and the relative change in PL observed (schematic graph in the middle). Off resonance, there's no change in PL (left energy scheme), but at resonant condition with the GS splitting ($E_{RF,\,res}$=2D, right energy scheme), spin flips can occur between the sublevels. Due to the spin dependent transition rates, the PL intensity changes (denoted by arrows' widths), resulting in a peak in the ODMR signal.

In case of the V_{Si}, the spinsublevels have a zero field splitting 2D (see section 2.3.4). Hence, ODMR without an external magnetic field, called *zero field* (zf) ODMR can be measured. The zfODMR principle on V_{Si} in SiC is depicted in figure 3.1. Here, 2D and hence the suitable microwave quanta are rather in the radiofrequency (RF) range from 10 MHz to 1 GHz.

3.3. Single photon counting

Luminescence and ODMR measurements were mostly performed on defect ensembles, with the advantage of a high PL signal. However it is also interesting to investigate a single defect, which is e.g. a prerequisite for a V_{Si}-based single photon source. As the PL intensity from a single defect is very low, one has to collect many emission events and evaluate the statistics of them, considering also the temporal character of the emission. This method of time resolved fluorescence spectroscopy is called *time-correlated single photon counting* (TCSPC). For a detailed treatment of TCSPC I refer to [102].

As explained in chapter 2.3.6, the second order correlation function $g^{(2)}(\tau)$ can prove the number of emitters and their quantum mechanical nature. A *start-stop* cross-correlation measurement yields the delay-time distribution of consecutive photon pairs. Due to the experimental conditions (low count rates and short separation times), the normalized and background corrected delay-time histogram is equivalent to $g^{(2)}(\tau)$ [103].

3.4. The experimental setups

For the investigations in this thesis, the described measurement techniques were applied in four different setups, which are described in the following. The common denominator of the different setups is the ***confocal microscopy***, schematically shown in figure 3.2. The excitation light is focused through an objective onto the sample. The sample's PL is measured in reflection geometry. The collected reemission is detected after passing the objective again, so that the focus of excitation and of detection coincide. A dichroic mirror is used for reflecting the PL in the detection path and a longpass filter cuts out the residual excitation wavelength. Furthermore, a pinhole is used as aperture and improves the spatial resolution significantly.

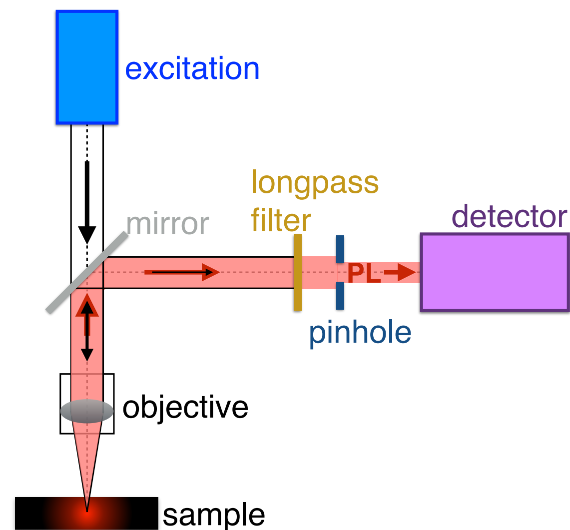

Figure 3.2.: Confocal microscopy scheme. For description see text.

This method has two advantages: First, the image of the sample is not areal, but rather a selective signal from the illumination focus. And second, misleading and unwanted background signal is omitted, as emission centers surrounding the focused volume are in the ideal case not even excited. With this confocality, the fluorescence of a sample can be investigated almost point by point. Nevertheless, in combination with a movable stage, the whole sample surface can be screened and this fluorescence map can e.g. help to localize single defects (see section 5.2) or to find nanoparticles (see section 7.2) on a cover slide.

3.4.1. LabRAM

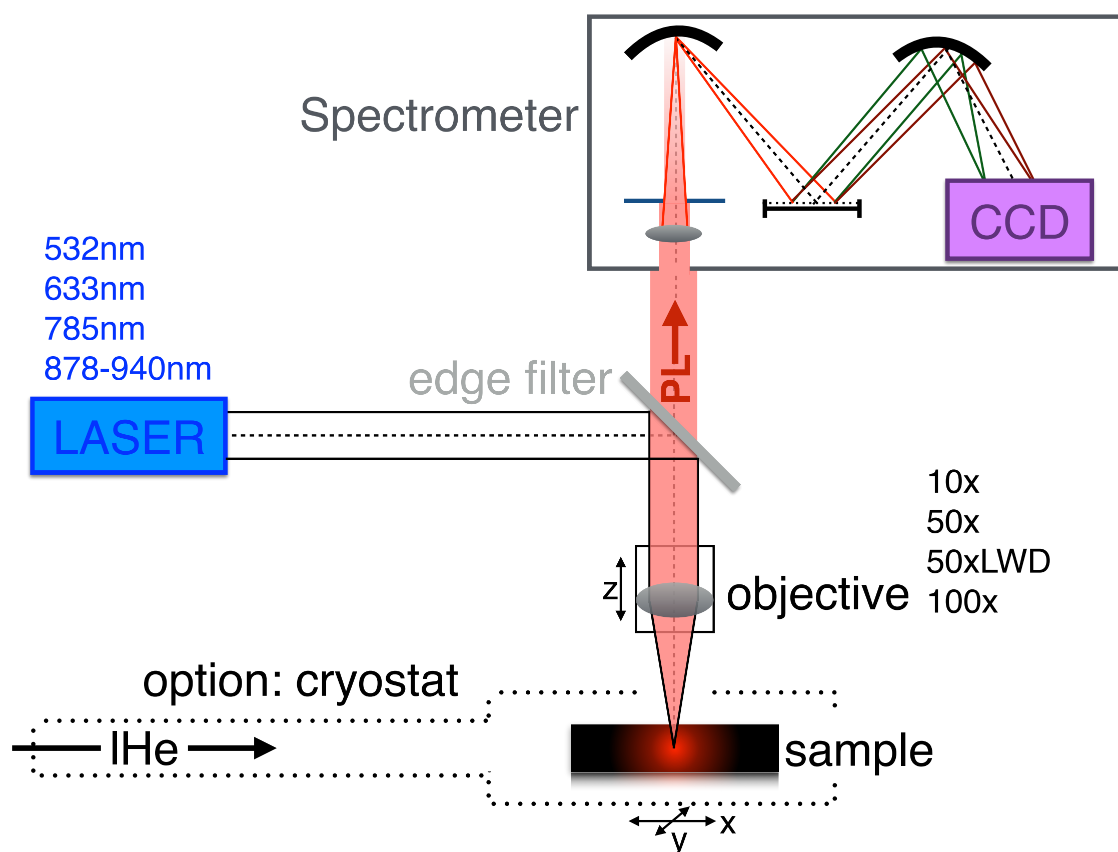

Figure 3.3.: LabRAM setup scheme. This spectrometer can measure spectrally resolved PL and EL. The optional implementation of a coldfinger cryostat allows for temperature dependent measurements from 4.2K to room temperature.

The confocal Micro-Ramanspectrometer LabRAM HR800 from HORIBA (see scheme 3.3) is equipped with the following lasers: a 632.8nm He-Ne-laser, a frequency doubled 532 nm Nd:YAG laser and a 785 nm laser diode, as well as the tunable diode laser Lion from Sacher (878 nm-940 nm, output power P≤15mW). The laser is focused via an objective (available magnification: 10x, 50x, 50xLWD (long working distance) and 100x)

on the sample. The emitted PL is collected with the same objective, and spectrally resolved in a spectrometer in Czerny-Turner configuration with 0.8 m focal length and two available gratings (600 or 1800 grooves per mm). A Peltier-cooled silicon based charge coupled device (CCD) is used as line detector, and the software LabSpec displays the measured spectra already corrected for the CCD sensitivity. This setup is mainly used for PL, but also for the EL measurements. The setup can be combined with an optically accessible cold finger cryostat (MicrostatHe from Oxford Instruments), when using the 50xLWD objective, so that temperatures from 300 K down to 4.2 K can be applied.

3.4.2. Home-built zfODMR setup

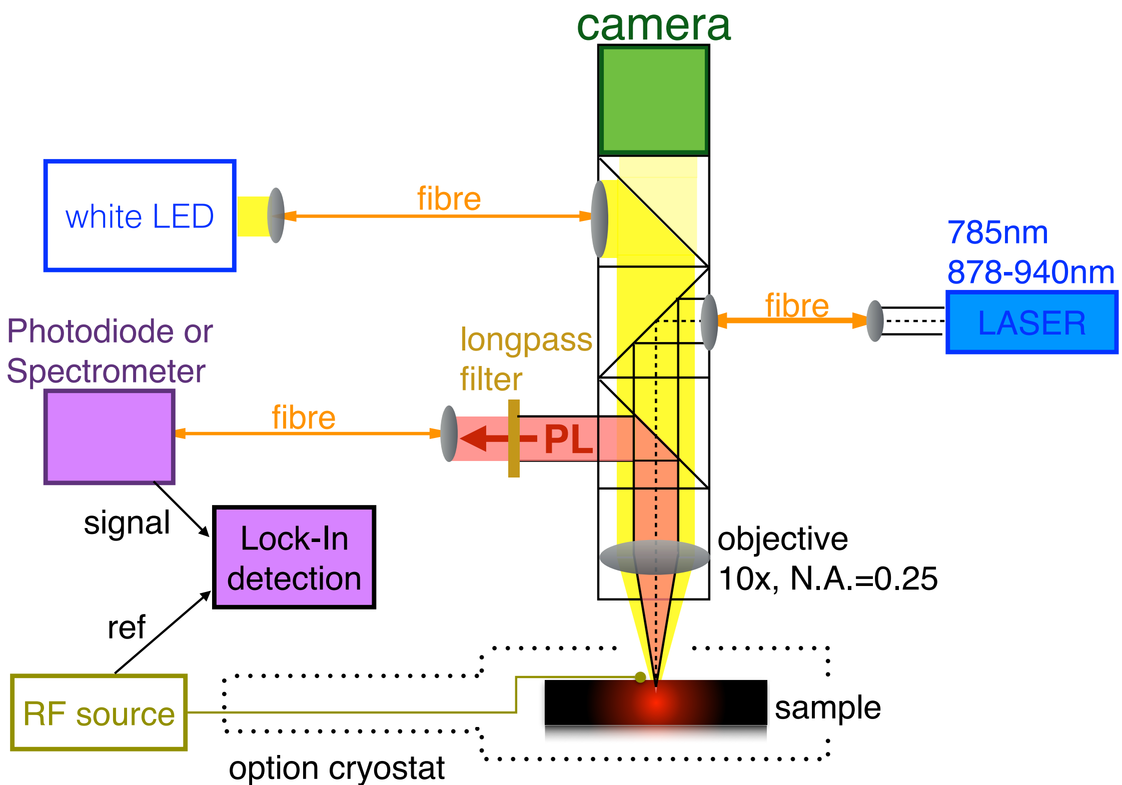

Figure 3.4.: Home-built zfODMR setup scheme. With a white light LED and a camera, the setup functions as classical optical microscope. Excitation and detection are fibre-coupled to and from an optical tower. This setup is for PL and zfODMR. For zfODMR, RF are coupled to the sample via a wire. The Lock-In detects the change in the photodiode signal due to RF modulation. The cryostat can also be used here for temperature dependent measurements.

We also built a confocal setup, which is optimized in the relevant NIR region and with mostly fibre coupled optics from and to a Thorlabs-cube optical tower, schematically

depicted in figure 3.4. For excitation, either a 785 nm laser diode with output power up to 400 mW is used or the tunable laser Lion from Sacher, the latter especially for resonant excitation. The optical response is detected with a fibre spectrometer SPM-002 from Photon Control or can be measured integrally with a Photodiode (Hamamatsu S2281-01, with pre-amplifier Femto DLPCA-200). This setup is used for PL, PLE and zfODMR measurements. Here, the sample is placed under a thin wire, wich is terminated with a 50Ω resistor and acts as an antenna to couple radio frequency (RF) into the sample. The RF is swept by a Stanford Research SG384 RF generator, additionally amplified by a solid state amplifier Becker 20280035-T with a maximum power output of 4 W. For ODMR signal detection the RF-amplitude is modulated (i.e. switched on/off) with 677Hz and the signal is locked-in with a Signal Recovery DSP Lock-In amplifier 7230. The Lock-In makes it possible to distinguish the tiny changes ($\sim 10^{-6} - 10^{-5}$) in the integrally detected signal.

The cryostat MicrostatHe can also be implemented in the home-built setup (denoted in figure 3.4). It has been modified, so that even temperature dependent zfODMR measurements could be carried out.

3.4.3. Single photon counting setup

For single defect measurements, another home-built confocal spectrometer setup is used, schematically shown in figure 3.5. The 785nm cw laser excitation beam is focused onto the sample by a high aperture (NA=1.49) oil immersion microscope objective (UAPON 100XOTIRF, Olympus). The sample is placed on a 3-dimensional piezo stage (c330, npoint) and can be moved in lateral and axial directions with high precision (1nm positioning noise). The optical response of the sample is collected by the same objective and guided through a 30 or 75 μm pinhole (Thorlabs) followed by a 850 and 875 nm longpass filter (Edmund Optics). Due to the precise stage, PL maps or raster scans of a sample can be measured with diffraction limited resolution. The delay-time histogram is recorded in a Hanbury Brown and Twiss setup consisting of a 50:50 beamsplitter, two avalanche photodiodes (APDs) (Count-100C-FC, Laser-components GmbH) with a quantum efficiency of about 0.3 at the signal wavelength and less than 100 cps in the dark and a 16-channel photon correlator card (DPC-230, Becker&Hickl GmbH) with a time resolution of at least 165 ps.

3.4.4. Combined imaging setup

Measurements were also performed in a combined spectrometer for spatial and spectroscopical imaging and time resolved measurements, depicted in figure 3.6. The used

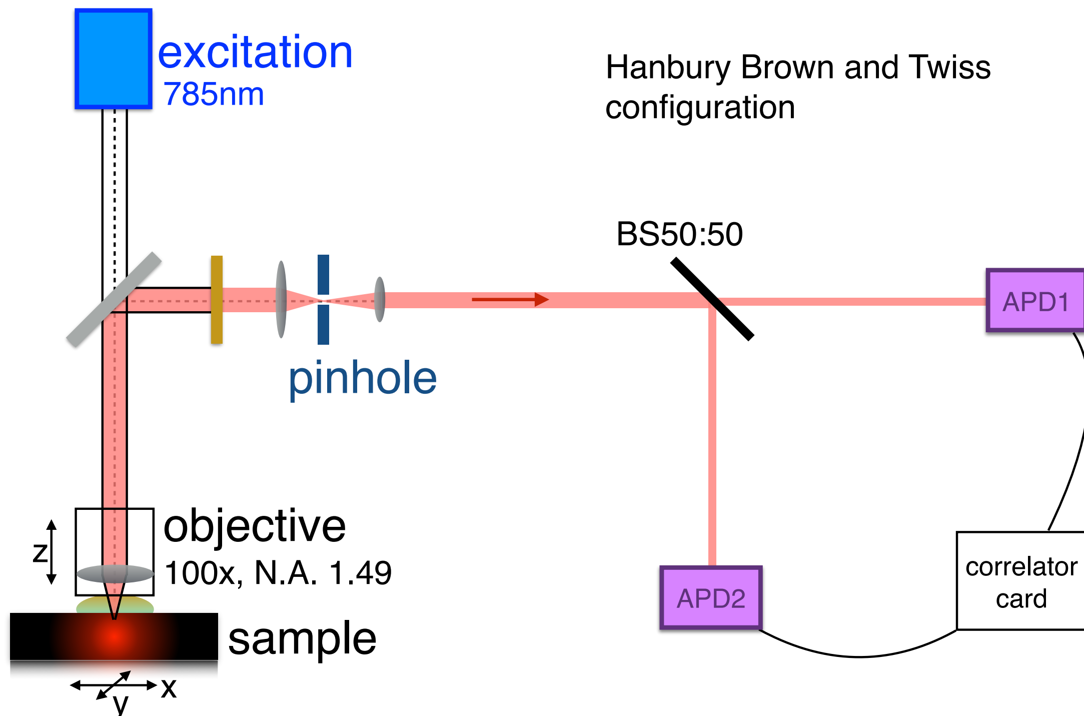

Figure 3.5.: Single photon counting setup scheme. The pinhole serves as entrance aperture. The Hanbury Brown and Twiss configuration is comprised of a 50:50 beam-splitter (BS) and two single-photon counting APDs, connected with a correlation card to capture the cross-correlation.

source in this case is a super-continuum white light laser SuperK EXTREME (EXR-15, NKT Photonics) with a tunable bandpass filter (SuperK VARIA, NKT Photonics). An CFI Super Plan Fluor ELWD (Nikon) objective with 20x magnification and NA=0.45 is used. The setup is equipped with a Clara interline CCD camera (Andor) for PL imaging. A Shamrock SR-303i spectrograph (Andor) together with either a Newton CCD camera (DU920P-OE) for detection from 760 to 1000 nm or an iDus InGaAs array detector (DU491A-1.7) for detection from 1000 to 1500nm can measure PL spectra and perform PLE mappings with a spectral resolution of circa 0.6 nm.

Additionally, time resolved measurements are possible. Here, the excitation is pulsed (5ps) at a repetition rate of 10 MHz. A single-photon silicon APD (Micro Photon Devices) detects the transient PL signal. The overall time resolution of the setup is 50ps.

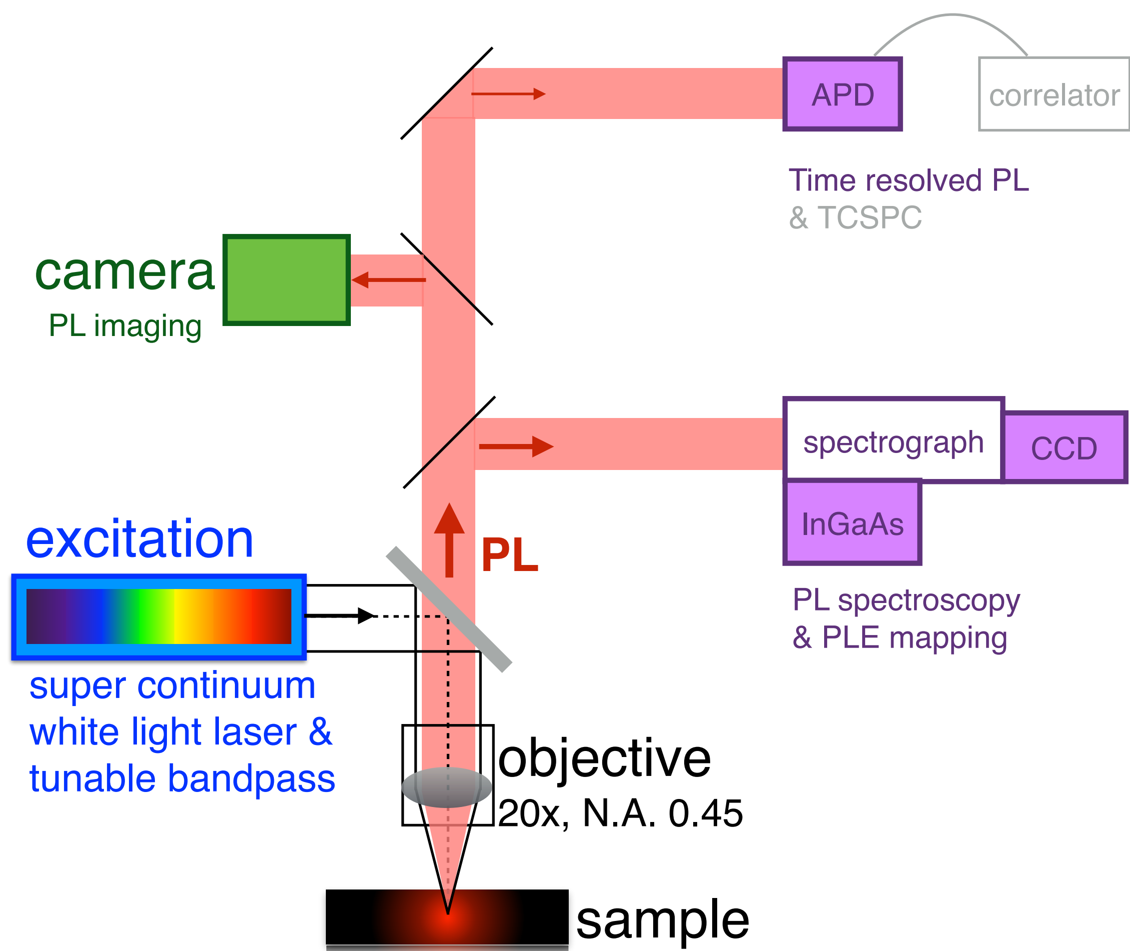

Figure 3.6.: Combined imaging setup scheme. The excitation wavelength of the white light laser can be tuned. In cw operation, the PL spectra are detected with a CCD or an InGaAs detector. PL transients after pulsed exciation can be recorded with an APD.

4. Optical properties of silicon vacancies

In the following chapter, optical properties of V_{Si} in SiC are investigated. The first section compares electron and neutron irradiation, both used for the creation of V_{Si}. The second section is dedicated to optical excitation and recombination dynamics, where two fundamental properties of the vacancies are evaluated, namely the optimum excitation wavelength and the lifetime of the excited state.

4.1. Creation of silicon vacancies

Intentional creation of defects in silicon carbide via irradiation damage has been used for many investigations. Already in 1970, Balona and Loubser used 0.8 MeV-electron and 1 MeV-neutron irradiation on 6H- and 3C-SiC [24]. Itoh and coworkers employed 1 MeV-electron and 2 MeV-proton irradiation on 3C-SiC [84] and also recorded the spin density dependence on the irradiation fluence over up to three orders of magnitude. In 2013, Falk and coworkers used an ion implantation process (^{12}C, at 190keV and doses of 10^{11}, 10^{12} and 10^{13} cm^{-2}) and annealing [104]. They showed good control of ensemble spin defects, but employed only 3 different ion doses. In two recent publications, 2 MeV electron irradiation yielded single spins, and both Widmann et al. [11] and Christle et al. [12] showed coherent control on them. The former also varied the electron fluence, but only at four test points within two orders of magnitude.

To sum up, despite many publications with different irradiation particles, systematic investigations over a wide range of irradiation fluences have not been reported yet. This gap will be filled with the investigation in chapter 5 where the neutron irradiation fluence is varied over 8 orders of magnitude. Also comparative studies of defect creation via different mechanisms are scarce. Hence, this section will show and compare electron and neutron irradiated 4H-SiC samples.

Sample

As the irradiation target, we used a high-quality silicon carbide crystal, namely a two inch 4H-SiC wafer from CREE (part number W4NRD8C-S0T4) with several epitaxial layers. The crystal c-axis is oriented 8° off the surface normal. The wafer thickness is

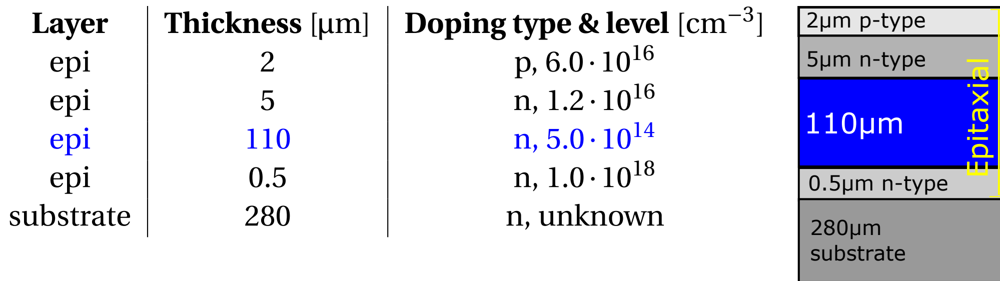

Layer	**Thickness** [µm]	**Doping type & level** [cm^{-3}]
epi	2	p, $6.0 \cdot 10^{16}$
epi	5	n, $1.2 \cdot 10^{16}$
epi	110	n, $5.0 \cdot 10^{14}$
epi	0.5	n, $1.0 \cdot 10^{18}$
substrate	280	n, unknown

Table 4.1.: 4H-SiC sample structure. The thickness and doping details of each layer is listed from top (surface) to bottom (substrate), the investigated layer is highlighted in blue. The layer structure is also schematically depicted to the right (not to scale).

ca. 0.4 mm and the wafer is diced into pieces of the size 2 x 4 mm^2. The interesting layer is the 110 µm thick epitaxial layer, being capped by a 5 µm thin n-type and a 2 µm thin p-type layer (see table 4.1 with sample scheme). Due to its very low residual doping level of $5.0 \cdot 10^{14} cm^{-3}$, it is ideal for the investigation of irradiation induced defects. Additionally, the other epitaxial layers and the substrate, do not disturb the measurements, as the confocality allows to spatially select the probed volume within the sample.

Defect creation

The samples were electron or neutron irradiated in order to create V_{Si}. Electron irradiation was done at the Ioffe Institute in St. Petersburg, Russia with 0.9 MeV electrons with different fluences from $2 \cdot 10^{16}$ up to $7.5 \cdot 10^{18}$ $e \cdot cm^{-2}$.

In the other case, neutron irradiation from a fission reactor of type TRIGA mark II at the Institute of Atomic and Subatomic Physics in Vienna, Austria[1] was applied. The reactor core delivers at its maximum thermal power (250 kW) $5 \cdot 10^{12} s^{-1} cm^{-2}$ fast neutrons (E > 183 keV). The neutron energies are distributed evenly from 100 eV to 0.1 MeV, and the peak in flux density around 2.5 MeV is followed by a sharp cut-off [105]. In silicon carbide, the damage caused by neutron irradiation varies weakly with neutron energy in the range 0.18 MeV< E_n < 2.5 MeV, but falls off rapidly for smaller energies, so that desired amount of vacancies can be tuned accurately with the fast neutron fluence [106]. The lower fluences were achieved by placing the samples either in the re-

[1] for further information see http://ati.tuwien.ac.at/reactor/EN/

flector irradiation tubes or in the radiography beam of the reactor, where the neutron fluence is several orders of magnitude lower than in the core. The desired fluences were then achieved by varying the irradiation time and fission power of the reactor. Thereby, the irradiation fluence could be varied from 10^9 to $5 \cdot 10^{17}$ n·cm^{-2}. During irradiation, the temperature of the samples stays below 100 °C. Some of the generated V_{Si} defects are negatively charged due to the presence of residual nitrogen donors ($5.0 \cdot 10^{14}$cm^{-3}). Additionally, the neutron transmutation doping $^{30}\mathrm{Si}(n,\gamma)^{31}\mathrm{Si} \rightarrow ^{31}\mathrm{P} + \beta$ may play a role [107]. The capture of a neutron by the nuclear isotope ^{30}Si (with natural abundance 3.2%) leads to the formation of the unstable isotope ^{31}Si. A subsequent beta decay converts it into the stable isotope ^{31}P, resulting in additional n-type doping of SiC. A negligible amount of radioisotopes is created in the irradiation process, so the crystals can be handled safely after cooling for eight hours.

Photoluminescence

After the irradiation procedures, photoluminescence (PL) was measured at different temperatures in the LabRAM setup (see section 3.4.1) to confirm the creation of defects. Figure 4.1 exemplarily shows several of the measured spectra.

At room temperature, one can see that a higher irradiation fluence results in enhanced PL intensity. This is confirms the irradiation induced damage of the SiC lattice. Furthermore, no ZPLs can be identified, as they vanish in the phononic background at room temperature. The maximum of the broad PL emission is around 890-930 nm.

At low temperature T = 5 K, the spectra show several sharp emission lines and broad phonon sideband background in the NIR from about 850 nm up to 980 nm. The lines are the ZPL of different defects. Two distinct sharp lines at 1.438 eV (≈862 nm, V1) and 1.352 eV (≈917 nm, V2) are associated with the silicon vacancies' ZPLs of the two different crystallographic sites in 4H-SiC [88]. Both spectral positions are denoted in the figure 4.1 with vertical dashed lines.

Remarkably, the peak locations are very similar despite different irradiation particles, indicating that both electrons and neutrons create the same types of defects in 4H-SiC.[2] For the lower neutron fluence (10^{13} n·cm^{-2}), no significant PL emission can be detected. With rising neutron irradiation fluence, more damage is caused to the SiC lattice, resulting in defect creation and hence detectable ZPLs. The fluence determines the defect concentration, which is investigated in detail in chapter 5. But also the ratio of the produced defect types varies with the fluence. The comparison of both

[2] For 3C-SiC this has been already suggested by Itoh et al. [108].

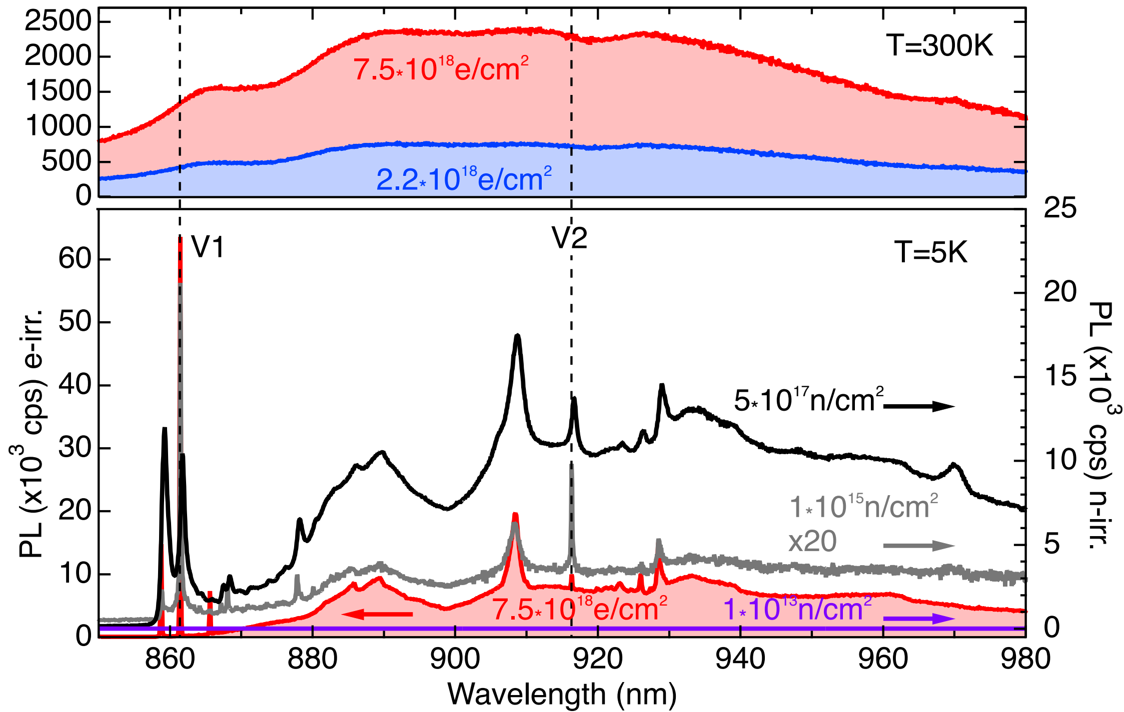

Figure 4.1.: PL of 4H-SiC after different irradiation treatment. Excitation with a He-Ne laser (633 nm) at different temperatures. **Upper part: T=300 K** PL spectra for electron irradiation at fluence $7.5{\cdot}10^{18}\,\mathrm{e{\cdot}cm^{-2}}$ (red) and $2.2{\cdot}10^{18}\,\mathrm{e{\cdot}cm^{-2}}$ (blue). A higher fluence results in higher PL intensity. **Lower part: T=5 K** The sample with electron irradiation fluence of $7.5{\cdot}10^{18}\,\mathrm{e{\cdot}cm^{-2}}$ (left PL axis) is compared to spectra of neutron irradiated samples (right PL axis) with fluences of $5{\cdot}10^{17}\,\mathrm{n{\cdot}cm^{-2}}$ (black), $10^{15}\,\mathrm{n{\cdot}cm^{-2}}$ (grey, multiplied by 20) and $10^{13}\,\mathrm{n{\cdot}cm^{-2}}$ (violet). Among other defects, also V_{Si} are created. Their two characteristic ZPLs V1 and V2 are denoted with vertical dashed lines.

neutron irradiated samples reveals that the lower fluence of $10^{15}\,\mathrm{n{\cdot}cm^{-2}}$ creates more V_{Si} in relation to other defects than the high fluence of $5{\cdot}10^{17}\,\mathrm{n{\cdot}cm^{-2}}$.

Additionally, the particle energy plays a role. The electron energy for example should be above the atom displacement threshold, which is for carbon around 100-150 keV and for silicon 250-300 keV [109, 110]. The applied electron energy of 0.9 MeV is well above the damage threshold. Thus, it can also be assumed, that the penetration depth of the electrons is comparable to the sample thickness (0.4 mm) [111].

All in all, it can be stated that, with both electron and neutron irradiation, various types of defects are created in the SiC crystal. Among them there are V_{Si}, having their two ZPL emission lines at 861.4 nm (V1) and 916.3 nm (V2).

These findings are noteworthy for defect engineering purposes. Although both irradiation types create the same type of defects, the type of irradiation may still make a difference in practical use. Neutron sources, like nuclear reactors, are less common

than electron sources. Neutrons normally have an energetically broader spectrum and the irradiation can yield a very high and homogeneous defect concentration (see next chapter 5). Electron sources are more suitable for patterning, as electrons can be focused, e.g. in a transmission electron microscope. Besides, integration in a semiconductor manufacturing process is easier with an electron source.

The investigation in the following section is performed on electron irradiated samples. Here, the V1 line at 861.4 nm is clearly the strongest line of the spectrum, surmounting the other peaks by more than a factor of three for the highest irradiation fluence of $7.5 \cdot 10^{18}$ $e \cdot cm^{-2}$. Thus the PL can assumed to be dominated by the emission of the V_{Si}.

4.2. Optical excitation and recombination dynamics

Both the excitation profile and the lifetime of the excited state of the V_{Si} were unknown so far. In a cooperation together with Prof. P. Baranov, V. Soltamov (Ioffe Institute, St. Petersburg, Russia), Prof. T. Hertel and T. Hain (Physical Chemistry, Julius-Maximilians University of Würzburg, Germany) we investigated both and evaluated the optimum excitation and the characteristic time of the PL decay. The results of this section are published in Journal of Applied Physics [112] with T. Hain as first and myself as second author.

Photoluminescence excitation at room temperature

The PLE measurements were conducted at room temperature in the combined imaging setup. Here, the PL is recorded in dependence of the excitation wavelength. The laser wavelength is chosen from the super-continuum spectrum in steps of 2 nm with a tunable bandpass filter (see section 3.4.4). Figure 4.2 shows the PLE map for the sample with electron irradiation dose of $2.2 \cdot 10^{18}$ $e \cdot cm^{-2}$. Here, the whole PL detection spectrum is plotted versus the excitation wavelength. The PL intensity is color coded in arbitrary units (a.u.). The top graph in figure 4.2 additionally shows a PLE spectrum, i.e. the PL at a certain detection wavelength in dependence from the excitation wavelength. This corresponds to a horizontal cut in the PLE map, in this case at the maximum emission wavelength (920 nm, denoted with a horizontal line in the PLE map). The PLE spectrum shows that for lower excitation wavelengths, the excitation is less efficient. For $\lambda_{exc} < 590$ nm the V_{Si} PL cannot be observed. The corresponding en-

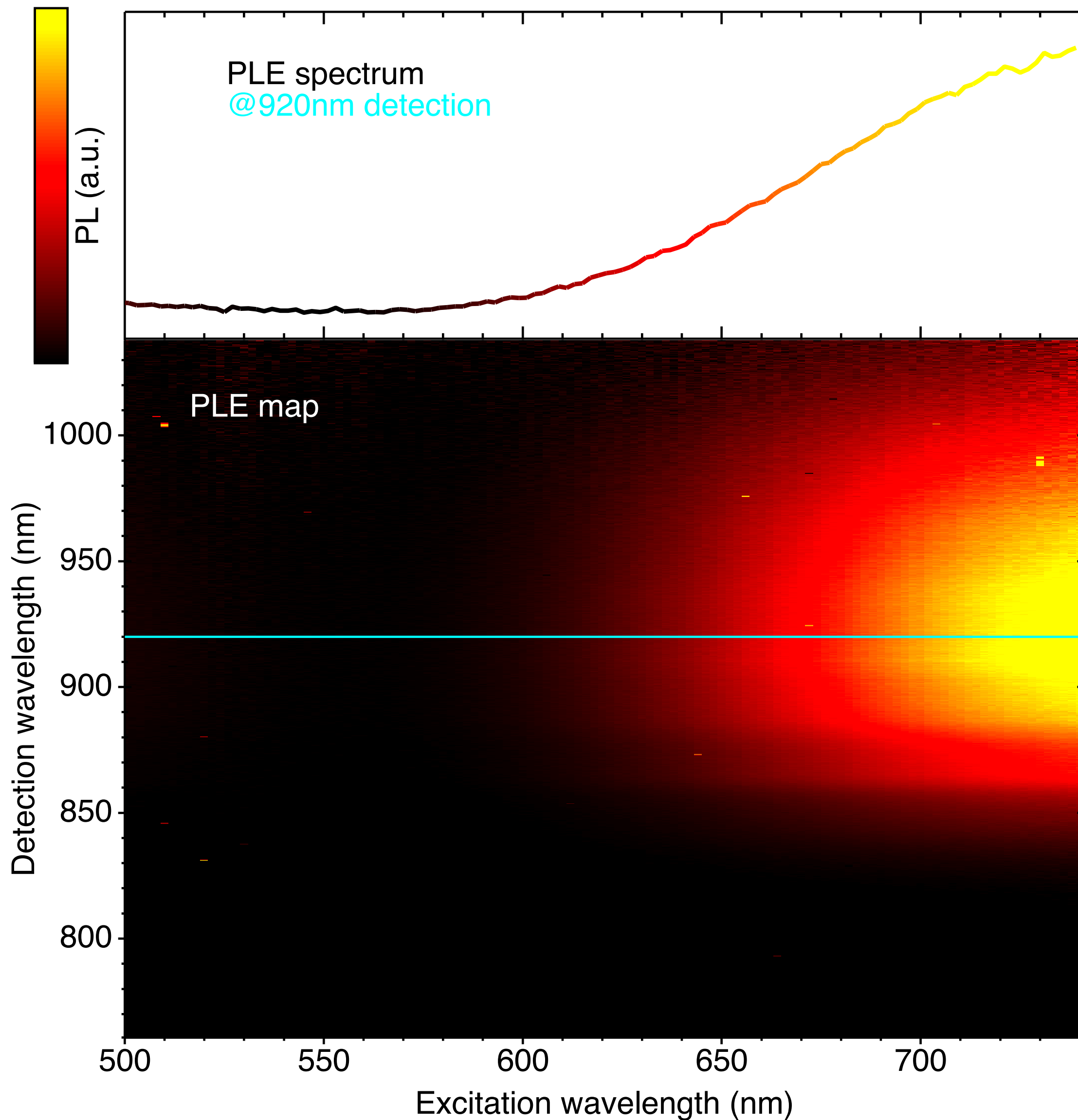

Figure 4.2.: PLE map and spectrum of 4H-SiC sample with irradiation dose $2.2{\cdot}10^{18}$ $e{\cdot}cm^{-2}$. Recorded at T=300 K in the combined imaging setup. The PL intensity is color coded in arbitrary units (dark: low PL, bright (yellow): high PL). The axes correspond to excitation (abscissa) and detection (ordinate) wavelengths. The PLE spectrum in the top graph is a horizontal cut at detection wavelength 920 nm (denoted in the map). *Measurements were carried out by Tilman Hain.*

ergy 2.1 eV is still smaller than the 4H-SiC bandgap so that no band-to-band excitation in SiC occurs.

Figure 4.3 shows again the PLE spectrum at emission wavelength 920 nm, now plotted against the excitation energy (linear bottom axis). The high-energy tail of the PLE spectrum can be fitted with a Gaussian function. This fit has its maximum at $E_{exc,max}$=1.64 eV, corresponding to a wavelength $\lambda_{exc,max}$ = 756 nm, and a FWHM

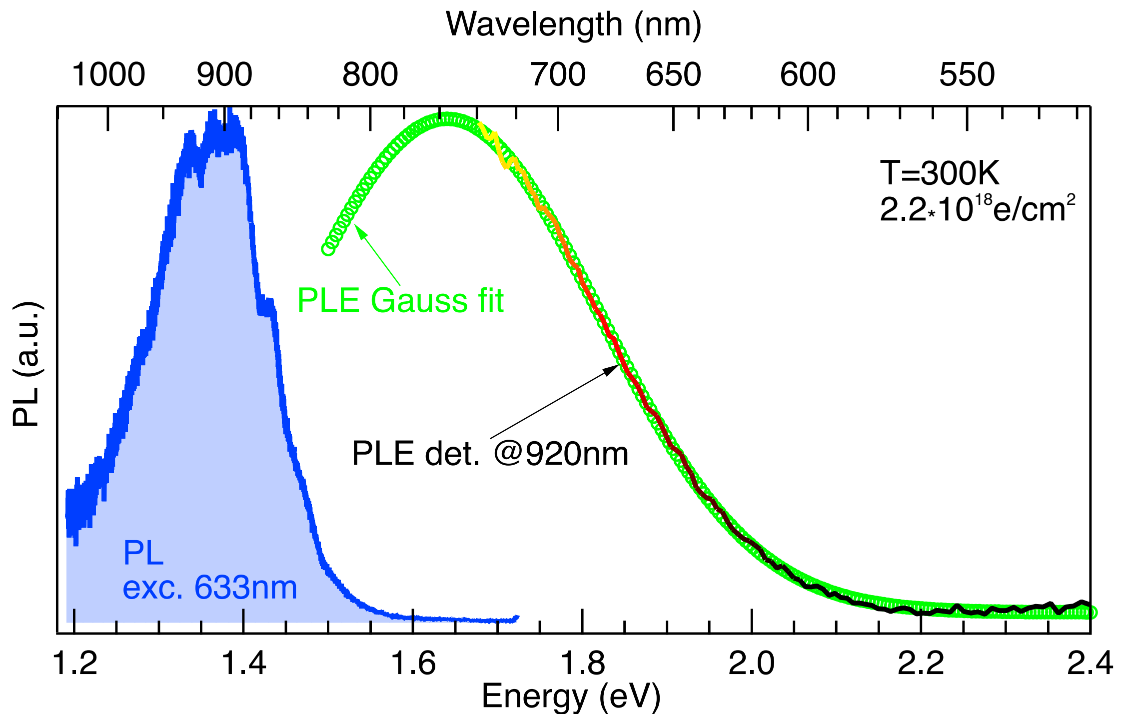

Figure 4.3.: PLE spectrum with fit and PL spectrum of 4H-SiC sample with dose $2.2{\cdot}10^{18}$ e·cm^{-2}. Temperature T=300 K. The PLE spectrum is detected at 920 nm in the combined imaging setup (color code like in fig. 4.2) and the fit is a Gauss curve (green circles). The PL spectrum is excited at 633 nm in the LabRAM setup (see also fig. 4.1). Note that the energy axis is the excitation energy in case of the PLE measurement, but the emission energy for the PL spectrum.

value of 0.43 eV. With that it can be concluded, that the optical excitation of V_{Si} is most efficient for excitation wavelengths in the region between 720 nm and 800 nm.

Additionally shown in figure 4.3 is the room temperature PL emission spectrum, measured in the LabRAM setup at excitation wavelength 633 nm. The spectral widths of PLE and PL are not the same, which is due to different potentials of the ground and excited state. Furthermore, the PLE maximum is blue-shifted with respect to the PL maximum. This behavior is in agreement with the Franck-Condon principle.

The excitation power dependence of the integrated PL intensity was also measured for two different spectral excitation ranges, shown in figure 4.4. The excitation in the range 740-760 nm is more efficient than for 600-620 nm, as expected from the PLE spectrum (fig. 4.3). In both cases, the PL depends linearly on the excitation power density up to 20 kW·cm^{-2} (600-620 nm), respectively 3 kW·cm^{-2} (740-760 nm).

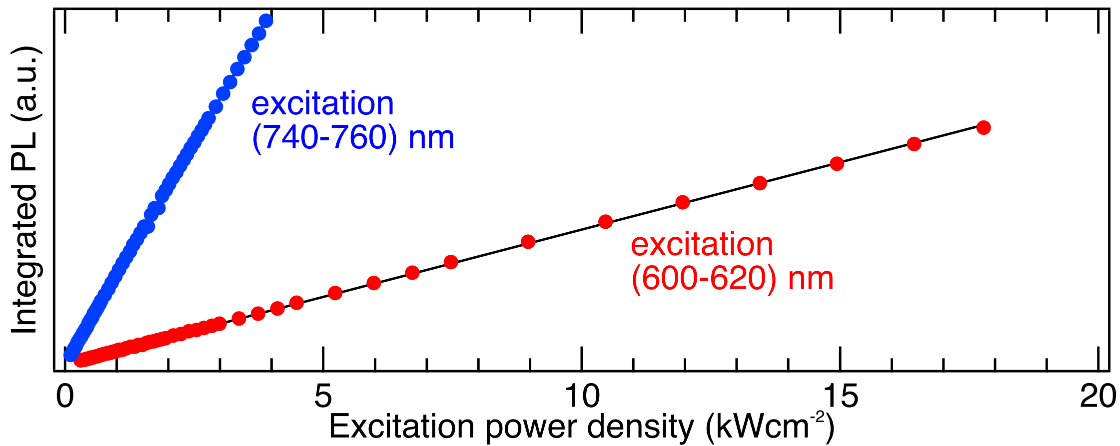

Figure 4.4.: Excitation power dependence of PL of 4H-SiC sample with dose $2.2{\cdot}10^{18}$ e·cm^{-2}. Temperature T = 300 K. The PL spectra are excited in two different ranges, 600-620 nm and 740-760 nm and the PL is integrated. The solid lines are linear fits. *Measurements were carried out by Tilman Hain and evaluated by Georgy Astakhov and myself.*

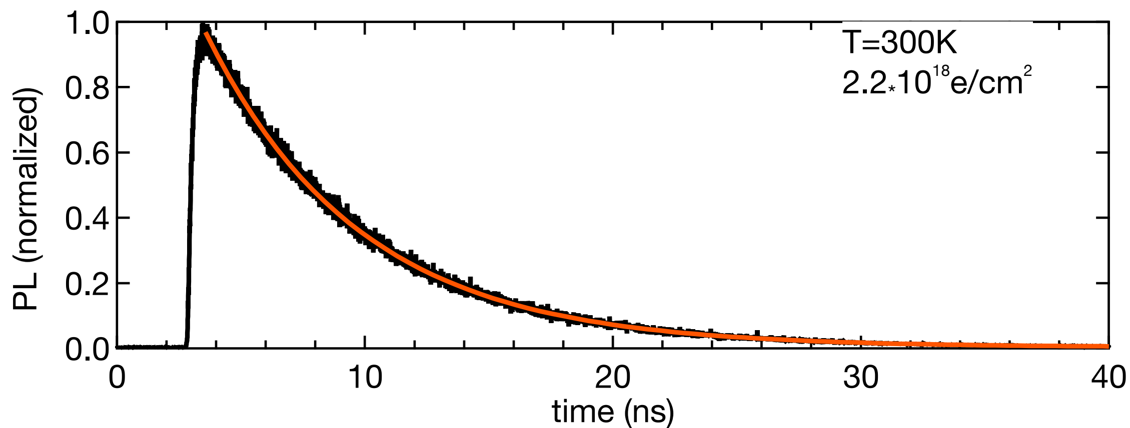

Figure 4.5.: PL decay of 4H-SiC sample with irradiation dose $2.2{\cdot}10^{18}$ e·cm^{-2}. Temperature T=300 K. *Measurements were performed by Tilman Hain.*

Photoluminescence dynamics

With transient measurements in the combined imaging setup, the PL dynamics of V_{Si} were analyzed. The excitation was pulsed and the PL integrally detected, as described in section 3.4.4.

Figure 4.5 shows the recombination dynamics of the sample with irradiation dose $2.2{\cdot}10^{18}$ e·cm^{-2} at room temperature. The PL progression after excitation can be fitted with a monoexponential decay of the form PL(t)=a+b exp(-t/τ). The fit yields a characteristic lifetime of the excited state of τ=(6.3±0.6) ns[3]. This is of the same order of

[3] Averaged value from four measurements with an estimated time uncertainty of 10%.

magnitude compared to the $C_{Si}V_C$ in SiC with 1.2 ns [43] or the NV center in diamond with 13 ns lifetime [113]. The lifetimes of these atomic-scale point defects are similar because they are all well isolated from the bulk bands and their optical transitions are determined by the coupling of the electronic and vibronic states.

Summarizing, the investigations in this section reveal two important optical properties of the silicon vacancies: First, the excitation of the V_{Si} is **most efficient** at excitation wavelengths between **720 nm and 800 nm**. Second, the PL decay yields a characteristic **excited state lifetime** of τ=(6.3±0.6) ns.

5. Defect engineering of silicon vacancies

This chapter describes the controlled creation of silicon vacancies via neutron irradiation. The defect density is varied over eight orders of magnitude and reaches down to the single vacancy level. This investigation was performed in cooperation with M. Trupke (Vienna Center for Quantum Science and Technology, Atominstitut, TU Wien, Austria), who was responsible for the irradiation and Prof. Pflaum, whose single photon counting setup I used jointly with B. Stender (Exp. Physics 6, Julius-Maximilian University of Würzburg, Germany). The results of this chapter are published in Nature Communications [114] with myself and B. Stender as equal contribution first authors.

5.1. Controlling defect density

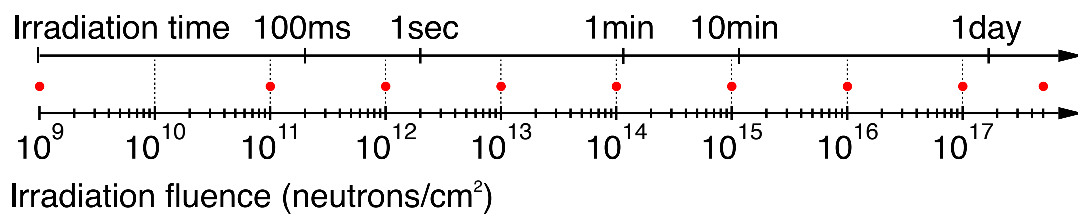

Figure 5.1.: Neutron irradiation fluences and times. Each dot corresponds to one of the 9 irradiated 4H-SiC samples. The applied fluence is the bottom axis (in n·cm^{-2}). The top axis shows the corresponding irradiation time.

Neutron irradiation

For the controlled defect introduction, we used neutron irradiation from a fission reactor (see section 4.1) with particle energies mainly between 0.18 MeV and 2.5 MeV and a variation of the irradiation fluence over more than eight orders of magnitude, from 10^9 to $5 \cdot 10^{17}$ n·cm^{-2}. The applied fluences and corresponding irradiation times in the reactor are depicted in figure 5.1.

Luminescence from defects

The spectrally resolved photoluminescence, as already shown in figure 4.1 of chapter 4.1, is measured in the LabRAM setup with excitation at 633 nm and at cryogenic temperatures of 5 K. The spectroscopic fingerprint of V_{Si} proves, that they are introduced via neutron irradiation.

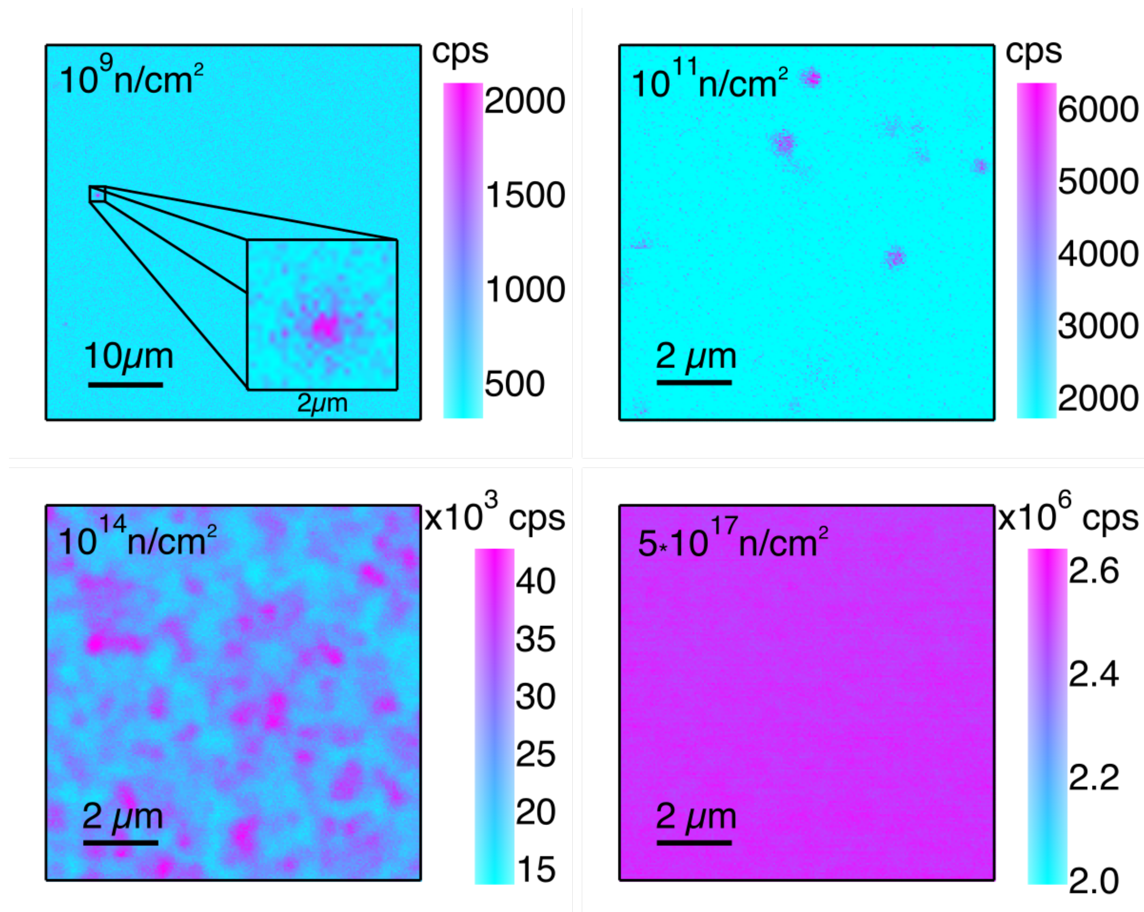

Figure 5.2.: Creation of V_{Si} in 4H-SiC via neutron irradiation. Confocal microscopy raster scans for different neutron irradiation fluences. Laser excitation was at 785 nm and 3.5mW (otherwise noted) Top left: (50×50 μm^2) PL image with a single defect (shown in the inset) for the lowest fluence of 10^9 n·cm^{-2}. Other images: 10×10 μm^2. Top right: 10^{11} n·cm^{-2}, bottom left: 10^{14} n·cm^{-2}, bottom right: highest fluence of $5{\cdot}10^{17}$ n·cm^{-2}, scanned at a laser power of 50 μW. The integrally measured PL is color coded in individual scales with the respective scale bar to the right of each image.

Additionally to PL spectra in the LabRAM setup, PL x-y-raster scans are measured at room temperature in the single photon counting (SPC) setup (see section 3.4.3). The laser excitation wavelength was 785 nm, which is in the optimal excitation regime according to chapter 4. After passing a 850 nm and a 875 nm longpass filter the PL is detected integrally with APDs. The SPC setup is also equipped with a monochromator and a CCD, so that the spectral shape of the emission can be compared with that from

the LabRAM PL measurement. Hence the PL can be confirmed to come from silicon vacancies.

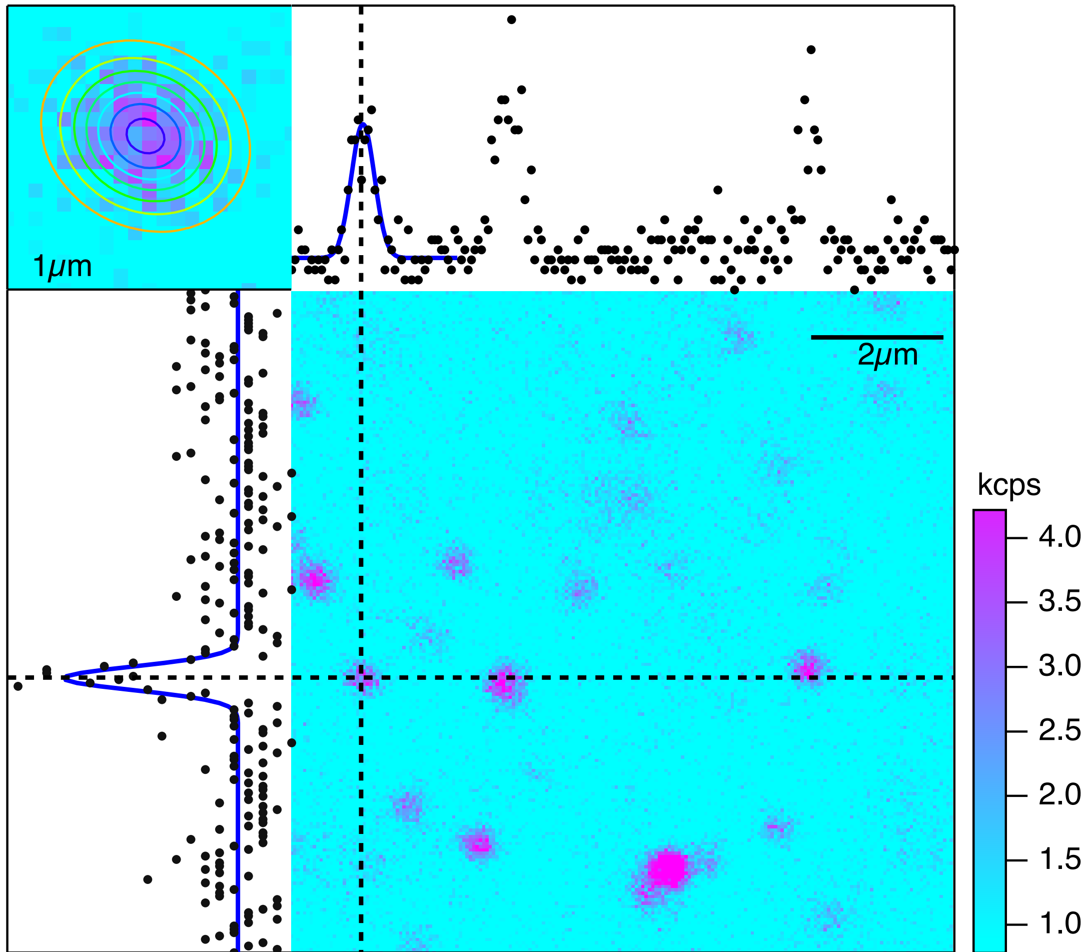

Figure 5.3.: PL raster scan image with single spots. Sample: neutron fluence 10^{12} n·cm^{-2}, Laser power: 3.5 mW. PL cross sections through a single spot are depicted above (horizontal cut) and to the left (vertical cut) of the color coded image. Both cuts are fitted with Gauss curves in the vicinity of the spot. The inset in the upper left corner shows a detail of the spot overlaid with contour plot of a 2-dimensional Gauss fit.

For the x-y-raster scans, the laser power is adjusted so that the APD detectors are below saturation. While measuring the PL, scanning an area of the sample with the movable x-y-stage yields the confocal microscopy raster scans with a spatial precision significantly lower than the diffraction limit. The PL signal intensity (in counts per second (cps)) is plotted in figure 5.2 in color coded images for four different fluences. The PL increases with increasing fluence, confirming the observation in the spectrally resolved PL (see fig. 4.1 in chapter 4.1). Due to the fluence variation over 8 orders of magnitude, the change in PL is also over a wide range. To see all features, every PL image in figure 5.2 has its own color scale, respectively depicted to the right.

Remarkably, in the with $10^9\,\mathrm{n\cdot cm^{-2}}$ negligibly weak irradiated sample (top left picture of fig. 5.2) only one PL spot is found in the $50\times50\,\mu\mathrm{m}^2$ square (magnified in the inset). This serves as upper residual defect density limit. The sample irradiated with $10^{11}\,\mathrm{n\cdot cm^{-2}}$ shows clearly four, nearly diffraction-limited spots. Note that the spectrally resolved PL for the sample with fluence $10^{13}\,\mathrm{n\cdot cm^{-2}}$ (see fig. 4.1 in chapter 4.1) did not result in measurable PL intensity. This means the PL raster scans are far more sensitive due to the different settings in the SPC setup (primarily the more sensitive APDs), giving valuable information concerning the samples with low irradiation fluence. With rising fluence to $10^{14}\,\mathrm{n\cdot cm^{-2}}$ the number of PL spots increases as well (see bottom left in fig. 5.2). For higher irradiation fluences, single PL spots cannot be resolved any more and the PL spatial distribution becomes highly homogeneous for $5\cdot10^{17}\,\mathrm{n\cdot cm^{-2}}$ (bottom right in fig. 5.2).

One of these single spots is examined more closely in the following. The sample with fluence of $10^{12}\,\mathrm{n\cdot cm^{-2}}$ is taken as example, but the single spots in all four samples with fluences up to $10^{14}\,\mathrm{n\cdot cm^{-2}}$ look similar. Figure 5.3 shows a $10\mathrm{x}10\,\mu\mathrm{m}^2$ PL raster scan with cuts (dashed lines) through a single spot. The horizontal cut is depicted above the PL image and the vertical cut to the left. Both cuts are fitted with Gauss curves in the vicinity of the spot. The full width at half maximum (FWHM) of the fits are 413 nm and 416 nm, respectively. The inset in the upper left corner shows a $1\mathrm{x}1\,\mu\mathrm{m}^2$ detail of the spot overlaid with contour plot of a 2-dimensional Gauss fit.

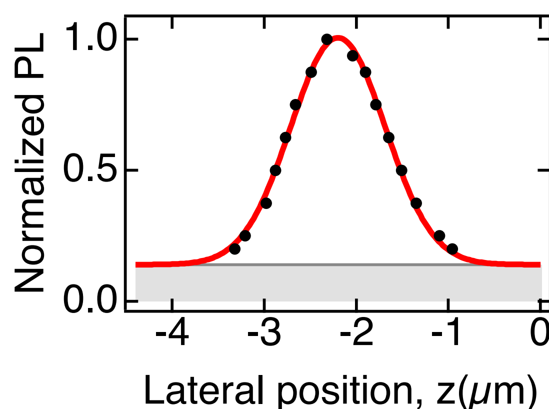

Figure 5.4.: PL profile through a single spot $z=0\,\mu\mathrm{m}$ is the top of the ultrapure layer. The solid line is a Gauss fit with a FWHM of $1.2\,\mu\mathrm{m}$.

The FWHM values for this 2D fit are 442 nm (in horizontal direction) and 405 nm (in vertical direction). So the average FWHM value of the single spot is: $\mathrm{FWHM_{mean}} \pm \sigma_{\mathrm{FWHM}} = (419 \pm 16)\,\mathrm{nm}$, i.e. the single spots are diffraction-limited. Additionally, the 2D fit shows that the round spot is almost symmetric, as the FWHM values in x- and y-direction only differ by 8%. This gives a first hint at a single emitter, which will be treated in the next section 5.1.

The PL signal of the single spot in figure 5.3 can also be measured in vertical direction by changing the focus z-position. This profile is shown in figure 5.4. The top of the ultrapure layer is at $z=0\mu m$ and negative z-direction means focusing into this layer.

The lateral PL profile can also be fitted with a Gauss curve (solid line in fig. 5.4). This Gauss fit has a FWHM of 1.2 µm, which can also be understood as a value for the focus depth.

Emitter density vs. neutron irradiation fluence

With neutron irradiation, defects, in particular silicon vacancies, are produced in SiC, as shown before in section 4.1. An important step towards defect density control is to elucidate the connection between the emitter density and the irradiation fluence.

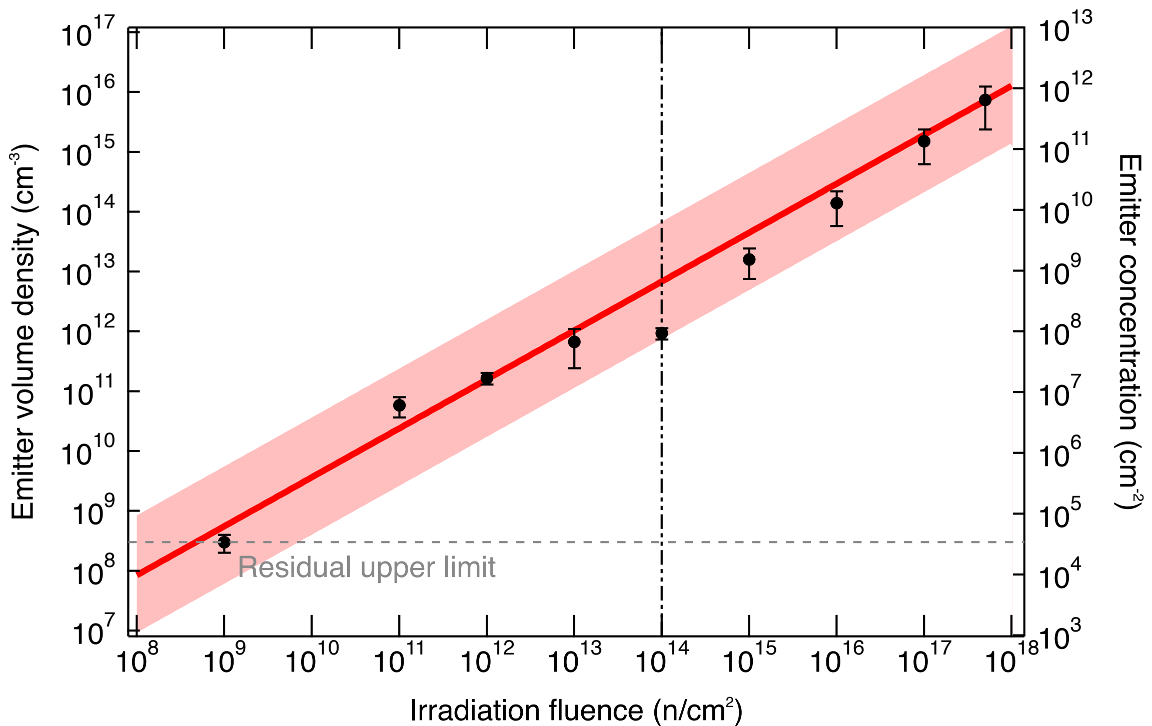

Figure 5.5.: Emitter density as a function of the irradiation fluence n. The left scale gives the defect volume density N per cm^3, whereas the right scale gives the defect concentration per cm^2. The density for the lowest fluence 10^9 n·cm^{-2} can be set as residual upper limit. For low irradiation fluences up to the vertical dashed line, the concentration is found by direct count of emitters in the given volume. The other values are determined through relations of PL intensities (see text). The solid line is a fit to $N = c \cdot n^{\alpha}$ with $\alpha = 0.8$.

In order to find the density of single emitting spots the following procedure is used. Up to the irradiation fluence of 10^{14} n·cm^{-2} one can directly count the number of PL spots in the scanned area. To extrapolate the 2-dimensional area defect concentration (in cm^{-2}) to the 3-dimensional volume defect density N (in cm^{-3}) , the focus depth is needed. From the PL line scan in z direction (see fig. 5.4) it is determined to be 1.2 µm.

As a cornerstone, also the integrated PL intensity collected from an area of about 100 μm^2 is measured for 10^{14} n·cm^{-2}. This PL is used as a reference to calculate the emitter density in the stronger irradiated samples by comparing PL intensities. The results are presented in figure 5.5. For the lowest irradiation fluence of 10^9 n·cm^{-2} the defect density is $N_{min} = 3 \cdot 10^8 cm^{-3}$, which can be taken as the upper limit of residual silicon vacancy concentration in our 4H-SiC wafer. The defect concentration after the highest irradiation fluence constitutes $N_{high} = 7 \cdot 10^{15} cm^{-3}$. The real value can be even higher due to the generation of other types of defects with non-radiative recombination channels leading to a reduction of the PL intensity. But with the applied approach, the emitter density can be varied in at least eight orders of magnitude. The error bars in figure 5.5 are determined through several countings/measurements at different spots. The irradiation fluence dependence follows quite well a power law $N=c \cdot n^\alpha$ with $\alpha=0.8 \pm 0.1$; where $[n]$=n·cm^{-2} and [N]=cm^{-3}, as shown by the solid line in figure 5.5. This empirical power law now could be used for the calculation of the required irradiation fluence to create silicon vacancies of desired concentration. Nevertheless, this method serves rather as a thumbs-rule than a quantification. Therefore, one order of magnitude above and below the fit is shaded, and in this area, all measurement points are located (including error bars). Qualitatively, the sub-linear dependence can be explained by the creation of some other types of defects in the positions of the silicon atoms with increasing irradiation fluence (see also fig. 4.1 in section 4.1), such that in these sites the silicon vacancy cannot be created. Also conversion of single silicon vacancies into other defects, e.g. divacancies with another nearby defect, may occur at higher fluences. However, these effects are relatively weak as α is not far below one.

5.2. Single silicon vacancies

For the samples with low irradiation fluence (i.e. up to 10^{15} n·cm^{-2}), single luminescent spots are isolated as shown in the previous section 5.1 in figures 5.2 and 5.3. Among these, fully photostable room-temperature near infrared (NIR) single photon emitters can clearly be identified.

To specify the type of generated defects, we measure PL spectra with the SPC setup for different irradiation fluences, shown exemplarily in figure 5.6 for two different neutron fluences. The spectra are normalized for better comparison, and have the same shape in general. In the single spot spectrum for the fluence 10^{13} n·cm^{-2} (depicted in green) there are two additional peaks visible. These are a residuum from the laser excitation at 785nm and a 4H-SiC Raman line. The latter is for the longitudinal optical phonon expected at 970 cm^{-1}[115, 116] which coincides here with 849.7 nm. Both

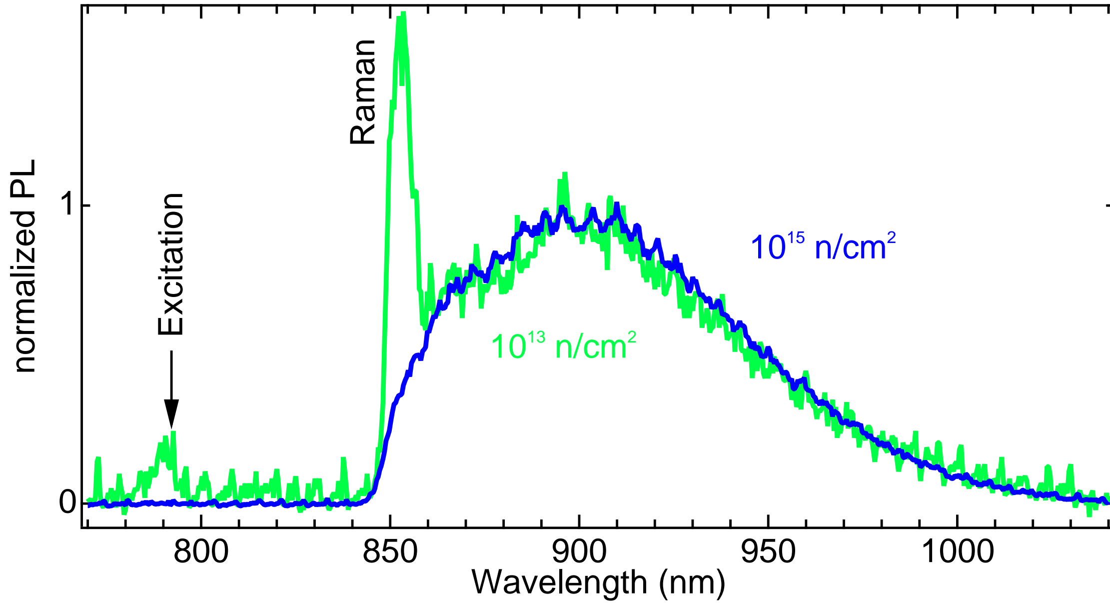

Figure 5.6.: PL spectra of a single spot and ensemble. Measured in the SPC setup at room temperature with excitation at 785 nm and 3.5 mW. A 850 nm longpassfilter eliminates the excitation wavelength in the detection path. The spectra are normalized for better comparison. **blue:** Ensemble spectrum from the sample with the fluence of 10^{15} n·cm^{-2}. **green:** Single spot spectrum from the sample with the fluence of 10^{13} n·cm^{-2}. Here, the PL intensity is ca. 50 times smaller, and both the excitation and a Raman line are visible. Otherwise, this spectrum resembles the ensemble silicon vacancy spectrum.

peaks are masked in the spectrum for 10^{15} n·cm^{-2} as here the PL intensity is about 50 times higher, but both laser residuum and Raman line are independent from the PL intensity. The spectra show some overlaying noise which is due to CCD pixel sensitivity differences, but they don't alter the general spectral shapes. In the low temperature PL spectrum from the LabRAM setup (figure 4.1 in chapter 4.1), we could show the presence of the silicon vacancies in the 10^{15} n·cm^{-2} sample. As the room temperature PL spectrum from the SPC setup for single spots of the samples irradiated with 10^{13} n·cm^{-2} and lower fluence are identical to the ensemble emission (10^{15} n·cm^{-2}), we can assume the single spot to be silicon vacancy emission as well. For the integral PL measurements (detected with two APDs) on single spots, we filter out the Raman line with an additional 875 nm longpassfilter. The integral PL intensity is measured at different excitation power density, see figure 5.7. To remove the APD dark counts and background fluorescence, the background B is measured next to the spot. It is linearly increasing with the excitation power density W. Subtracting B from the measured total count rate T on the spot yields the real PL signal I. It saturates with increasing excita-

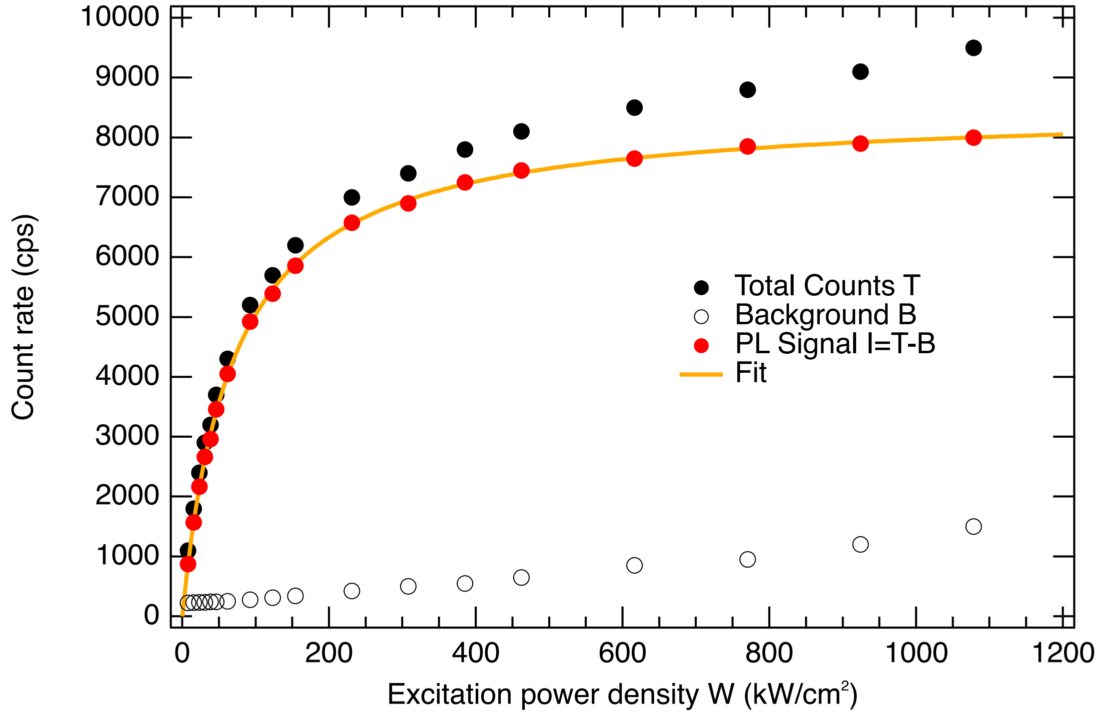

Figure 5.7.: PL saturation curve. Integrated PL intensity of a single spot on the sample with fluence 10^{11} n·cm^{-2}. Measured in the SPC setup at room temperature with excitation at 785 nm at various excitation powers. Longpassfilter 850 nm and 875 nm were used to remove the excitation wavelength and the SiC Raman line in the detection path. Measured are the total count rate T and the background B. The signal I is the difference I=T-B. The signal count rate saturates with increasing excitation power density W, which is expected for single defect centers. The saturation fit is according to equation 5.1.

tion power density W, which is expected for single defect centers. This can be fitted according to

$$I(W) = \frac{I_{sat}}{1 + \frac{W_0}{W}} \tag{5.1}$$

yielding a saturation PL intensity of I_{sat}=8.5 kcps and a saturation power density of W_0=69 kW·cm^{-2}, corresponding to a laser power of P_0=0.22 mW at the objective entrance aperture.

Second order correlation function

In the Hanbury Brown and Twiss (HBT) configuration (see figure 3.5), cross-correlation measurements on single spots were performed. The photon detection events of the APDs are correlated to yield the time-delay histograms. From this, the second order correlation function $g^{(2)}(\tau)$ can be deduced according to Brouri et al. [117], which is described in the Appendix A.2. The $g^{(2)}(\tau)$ function is depicted in figure 5.8 for different

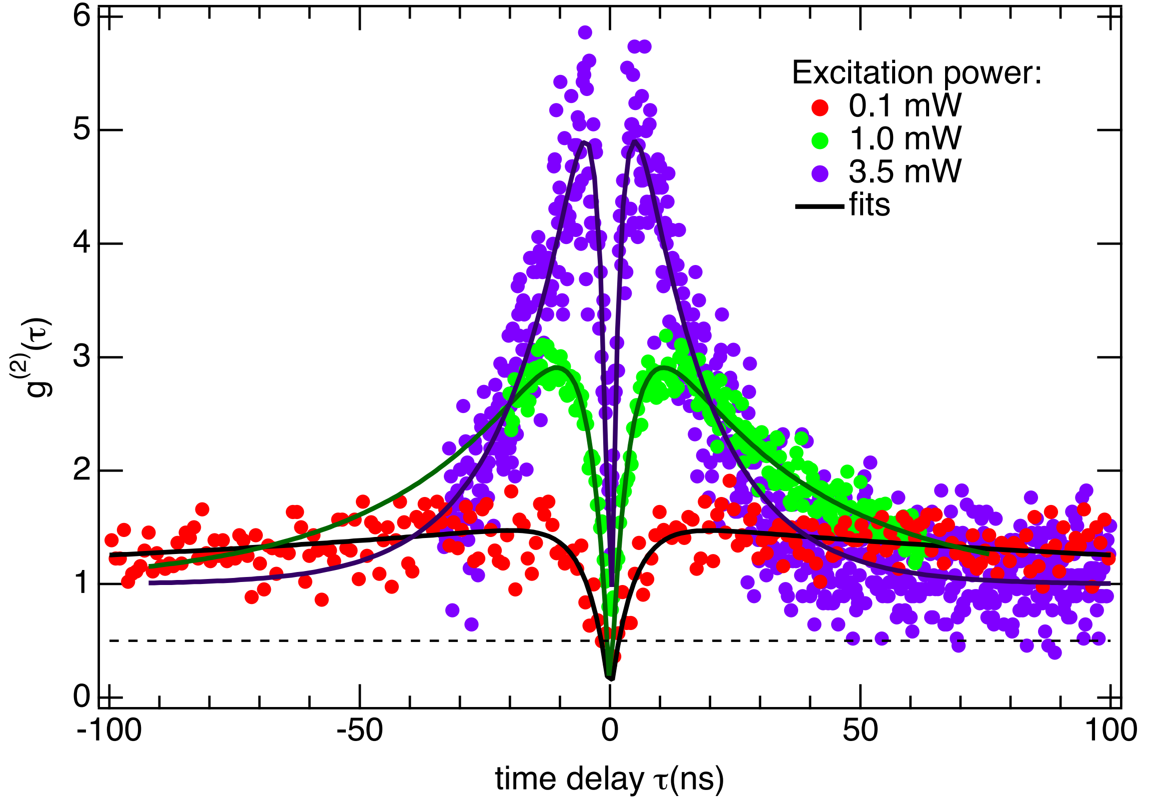

Figure 5.8.: Second order correlation function of a single spot for different excitation powers. Measured on the sample with fluence 10^{11} n·cm^{-2} in the SPC setup at room temperature with excitation at 785 nm. The antibunching dip at $\tau = 0$ going below 0.5 (horizontal dashed line) for small excitation powers proves the single spot to be a single defect. Additionally, power dependent bunching occurs.

excitation powers. The power is varied from 0.1 mW to 3.5 mW in ten measurement points (steps of 0.1 mW to 0.5 mW). For the sake of clarity, figure 5.8 shows only three representative curves. The other measurements are not contradicting the presented results. All second order correlation functions show an **antibunching** dip, proving the quantum mechanical behavior of the V_{Si} system. Additionally, **bunching** is observed. The second order correlation function can be well described with a double exponential fit

$$g^{(2)}(\tau) = 1 - (1+a)e^{-\frac{|\tau|}{\tau_1}} + a \cdot e^{-\frac{|\tau|}{\tau_2}} \tag{5.2}$$

The fit curves are shown as solid lines in figure 5.8.

The antibunching is more pronounced for small excitation powers. The reason is that the background increases linearly with the laser power (compare fig. 5.7) but quadratically in the correlation function [103]. This leads to a decreased signal-to-background ratio for increasing excitation power and thus the antibunching contrast is diminished with rising power. For the lowest excitation, we obtain $g^{(2)}(0)=0.29\pm0.07$.

For a single photon emitter, theory predicts $g^{(2)}(\tau)(0)=0$ (see theory section 2.3.6). Due to a finite temporal resolution of the setup (e.g. dead time of the APDs), the $g^{(2)}$ function may not reach zero for $\tau = 0$. Nevertheless, if $g^{(2)}(0) < 0.5$, the formula to calculate the number of emitters $g^{(2)}(0) = \frac{\langle n(n-1)\rangle}{\langle n\rangle^2} = 1 - \frac{1}{n} < 0.5$ yields n<2, and thus n=1 ($n \in \mathbb{N}$). Therefore, the $g^{(2)}(0)$ values here clearly identify the single spot as a single emitter, i.e. a single silicon vacancy.

The additional bunching effect of these $g^{(2)}$ functions are values above 1 for times $|\tau|>10$ ns, which cannot be explained with a simple 2-level emitter. Hence, either a 3-level or a 4-level model is considered. Both have been already introduced in the optical cycle model in section 2.3.5, figure 2.7. The level models with the relevant transition rates are depicted in figure 5.9. In both cases, the transition rates k_{12} and k_{21} between the ground state GS and the excited state ES are assumed to be independent from the spin state. Thus the ZFS is irrelevant and the respective two actually split levels can be treated here as one level.

With the power dependencies of the $g^{(2)}(\tau)$ fit parameters a, τ_1 and τ_2 (see equation 5.2), the transition rates can be calculated with some assumptions. The detailed derivation can be found in the appendix A.3. The rate calculations for the here measured $g^{(2)}(\tau)$ functions were carried out by Georgy Astakhov and Benedikt Stender [114]. Table 5.1 summarizes and compares the outcomes for the 3- and 4-level model. Both models yield similar transition rates that are comparable within the standard errors. The 4-level model can reproduce the power dependence of the fits parameters a, τ_1 and τ_2 somewhat better. This is not unexpected, as a fit gets always better, the more parameters are being used. The main change in the 4-level model is that the rate k_{31} is not kept constant. But the relative change in this rate from $1/k_{31}^{0}$=150 ns to $1/k_{31}^{\infty}$=123 ns is only 18%. This indicates that already the 3-level model is a sufficiently good description of the excitation dynamics.

From these transition rates respectively the corresponding times, one can calculate the lifetime τ of the excited state. It is

$$\tau = \frac{1}{\frac{1}{\tau_{12}} + \frac{1}{\tau_{23}+\tau_{31}}} = \frac{1}{k_{21} + \frac{1}{\frac{1}{k_{23}} + \frac{1}{k_{31}}}} \tag{5.3}$$

This yields τ=7.2 ns for the 3-level model, and 7.4 ns (with $1/k_{31}^{\infty}$), respectively 7.5 ns (with $1/k_{31}^{0}$) for the 4-level model.

Comparing these values with the lifetime τ=(6.3±0.6) ns from the time resolved PL decay measurements in section 4.2, the times do match reasonably well. Considering the different methods of measurement and extraction procedures as well as the uncertainties, the lifetime of the excited state can be given as τ=**(6.5±1.0) ns**.

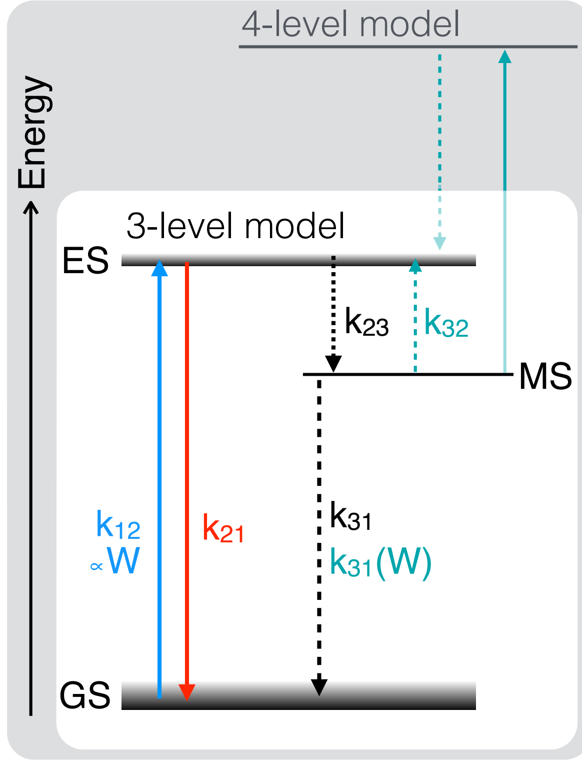

Figure 5.9.: Energy level scheme: Excitations are solid arrows, the PL is colored in red and non radiative transitions are dashed arrows.

Model:	3-level	4-level
σ (10^{-16} cm^2)	1.5	1.1
Rate		
$1/k_{21}$	7.6 ns	7.8 ns
$1/k_{23}$	16.8 ns	16.4 ns
$1/k^0_{31}$	107 ns	150 ns
$1/k^\infty_{31}$		123 ns

Table 5.1.: σ and rates k_{ij} (given as time constants $1/k_{ij}$) of a single V_{Si} for both models. *The calculations were carried out by Georgy Astakhov.*

Level schemes, transition rates k_{ij} and absorption cross section σ for 3- and 4-level model. 3-level model with constant rates k_{21}, k_{23} and k_{31} and an excitation with linear power dependence $k_{12}(W)=\sigma W$. The 4-level model adds a power dependent deshelving process. An excitation from MS to a higher lying state is possible, with a relaxation back to the ES. This is effectively introducing the rate k_{32}, respectively leading to a power dependent rate $k_{31}(W)$. The table shows the calculated values.

The transition rates or lifetimes (see table 5.1) are also interesting to compare with the corresponding 3-level model values for the NV-center in diamond [97, p. 293]. Both relaxation paths ES→GS and ES→MS happen around two times faster in the V_{Si} defect than in the NV-center ($1/k_{21,NV}$=20 ns, $1/k_{23,NV}$=31 ns). The lifetimes of the metastable state of both systems are comparable, with $1/k_{31}$=107 ns of V_{Si} being slightly shorter than $1/k_{31,NV}$=127 ns for NV. Thus the excited state lifetime of the NV-center is expected to be longer than the lifetime of V_{Si}. According to equation 5.3 and the values from literature [97, p. 293], the NV lifetime can be calculated to τ_{NV}=18 ns. From transient measurements, a value of τ_{NV}=13 ns [113] has been reported. This is indeed twice the lifetime of the silicon vacancy.

The question, which lifetime is better cannot be answered easily, as it depends on the application. A shorter lifetime results in shorter information storage time, but also enables faster cycling. Additionally, the rates for both systems only differ by a factor of two. That means the investigated V_{Si} is comparable and very similar to the NV-center in diamond.

Photostability

A crucial characteristic of a reliable single photon emitter is its photostability. Figure 5.10 shows the PL time traces of a single V_{Si} defect for different sampling times per bin Δb. For a sampling to Δb=100 ms the count rate remains constant over minutes. For examination of the stability on a shorter time scale, the bin width is reduced to Δb=1 ms. The number of detected photons per sampling bin is 10 in this case, and the time trace demonstrates statistical fluctuations without any indication of blinking at the observed timescales. An investigation of a single V_{Si} emitter over more than one week under continuous excitation did not lead to any photobleaching. Assuming that the excitation occurs on average every 10 ns, this corresponds to 10^{14} excitation cycles.

The maximum count rate of a single V_{Si} defect is about 10^4 cps. Using an optimized detection scheme with high detection efficiency of single photons as in the visible spectral range and with high optical transmission (above 90 %) in the NIR, a fourfold count rate of about $4{\cdot}10^4$ cps should be achievable. However, this count rate is still lower than expected from the transitions rates in table 5.1. This discrepancy can partially be explained by a relatively high refractive index of SiC ($n_{r,\,SiC}$=2.6), resulting in a large percentage of photons being restricted within the crystal due to total internal reflection. To overcome this problem, one can either fabricate a solid immersion lens or use nanocrystals. In this case, together with optimized detection scheme a count rate above 10^5 cps is feasible. And indeed, Widmann et al. recently achieved a count rate of $4{\cdot}10^4$ cps by using a solid immersion lens [11].

5.3. Annealing behavior

In the highly irradiated sample (neutron fluence $5\cdot10^{17}$ n$\cdot$cm^{-2}) a local increase of the PL intensity upon extended laser illumination was observed. To demonstrate this effect, different laser power densities were focused sequently on three different spots and remained there for 120 minutes, respectively. The PL timetrace during this treatment was tracked and is shown in the right part of figure 5.11. As expected, the PL intensity is higher for higher excitation power. For all three powers (0.5, 1.5 and 3.5 mW), the PL

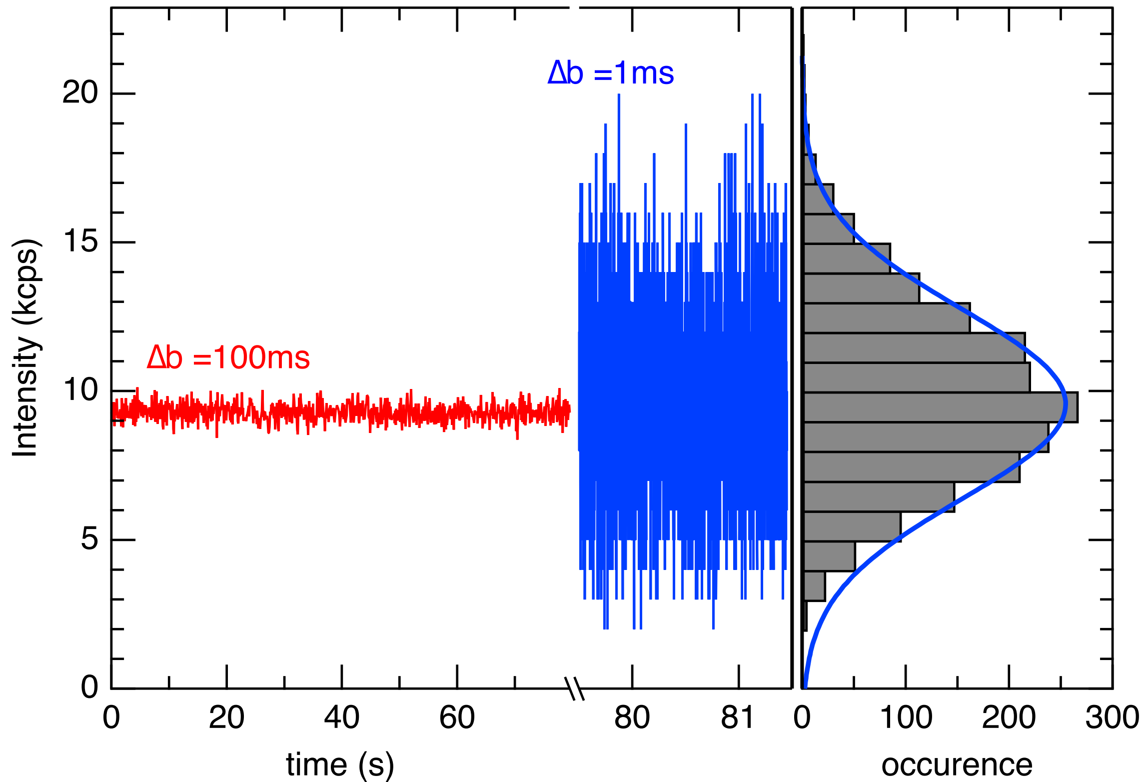

Figure 5.10.: Photostability. Left: PL time traces with sampling bins Δb=100 ms (red) and Δb=1 ms (blue) obtained on a single V_{Si} defect in the sample with fluence 10^{11} n·cm^{-2}. Measured in the SPC setup at room temperature with excitation at 785 nm and 3.5 mW. **Right:** Corresponding count rate histogram for Δb=1 ms. The solid line is a Gauss fit.

signal rises and saturates after some time. The timetraces normalized to the respective initial value, shown in the upper right panel of figure 5.11, reveal that the progression in all three cases is the same and the PL enhancement after 120 minutes of laser illumination is about (14±1)%.

After this procedure, a confocal raster scan was performed at low laser power of 50µW to minimize possible laser illumination effects during this scan. The left graph of figure 5.11 demonstrates clearly the PL enhancement for each spot compared to the quite uniform surrounding PL. The spot PL intensity is stronger, the higher the laser power on the respective spot has been during illumination. For the highest laser power of 3.5 mW, this enhancement is ca. 25% compared to the surrounding PL.

Prior to the discussion of possible mechanisms, a complementary thermal annealing experiment should be envisaged. Here, the temperature was increased stepwise from 125°C to 700°C and the PL intensity monitored after each step.

For each step the annealing temperature was kept constant for 90 minutes. The sample was put into a glass tube for better handling and prevention of contamination. The

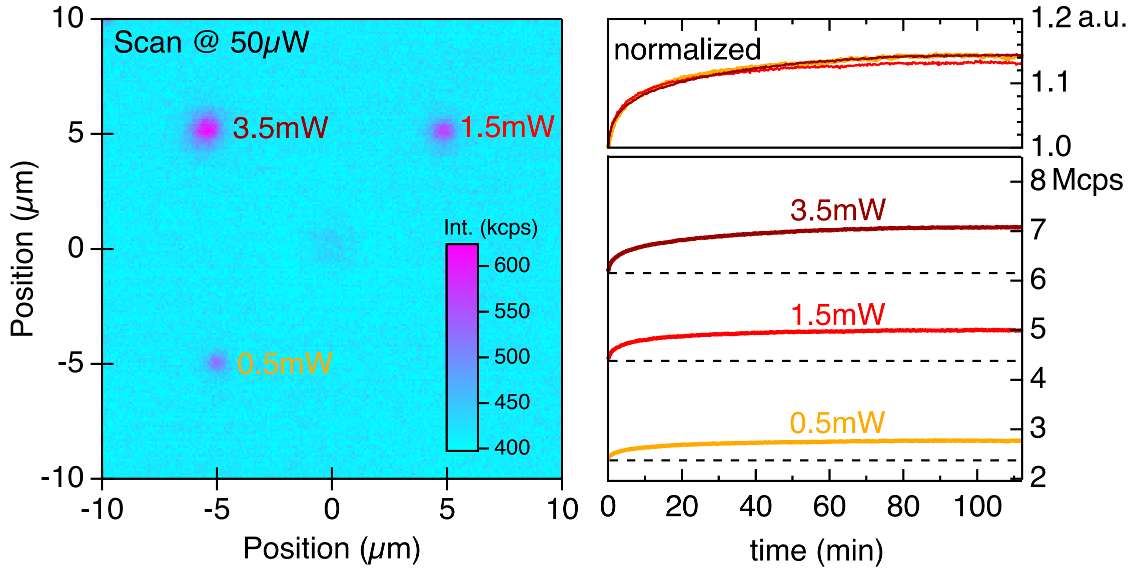

Figure 5.11.: Laser annealing. Left: Confocal raster scan after laser illumination of three spots with different laser power (indicated next to the spots). Measured in the SPC setup at room temperature with excitation at 785 nm and at 50μW. **Right:** PL time-traces during the laser illumination treatment at different laser powers: 0.5 mW (orange), 1.5 mW (red), 3.5 mW (dark red). In the upper panel, the same traces are normalized to the respective initial PL value.

annealing up to 200°C was performed on a heat stage, with the glass tube standing in oil for better and uniform heat transport. For annealing temperatures at and above 300 °C, a muffle furnace (M110 from Thermo Scientific) was used, in which the glass tube with the sample was placed. The heating ramp in this case was chosen to be around 3-4°C per minute. After each annealing step, the PL spectrum was measured in the LabRAM setup at room temperature with excitation at 633 nm. Figure 5.12 shows the obtained PL spectra (left) and the annealing temperature dependence of the integral PL signal relative to the corresponding value of the RT spectrum (right). The integral is calculated in the V_{Si} NIR emission region from 800-1000 nm and the RT spectrum was measured before the thermal annealing treatment.

The spectral shape remains unchanged, while the PL intensity increases with increasing annealing temperature up to T_{Ann}=600 °C. The subsequent annealing step at 700 °C leads to a significant drop in PL signal. Although 700°C is below the *annealing out* temperature of the V_{Si} (750°C [84]), the significantly lower PL can be explained with the same mechanism. Above 750°C, the V_{Si} mutate to the thermally more stable $C_{Si}V_C$ antisite-vacancy pair [118]. The onset of this *annealing out* may be starting even at a temperature between 600°C and 700°C. Hence, the annealing step at 700°C leads to a significant reduction of V_{Si} in the sample, resulting in PL decrease by a factor of 2, compared to the previous annealing step at 600°C.

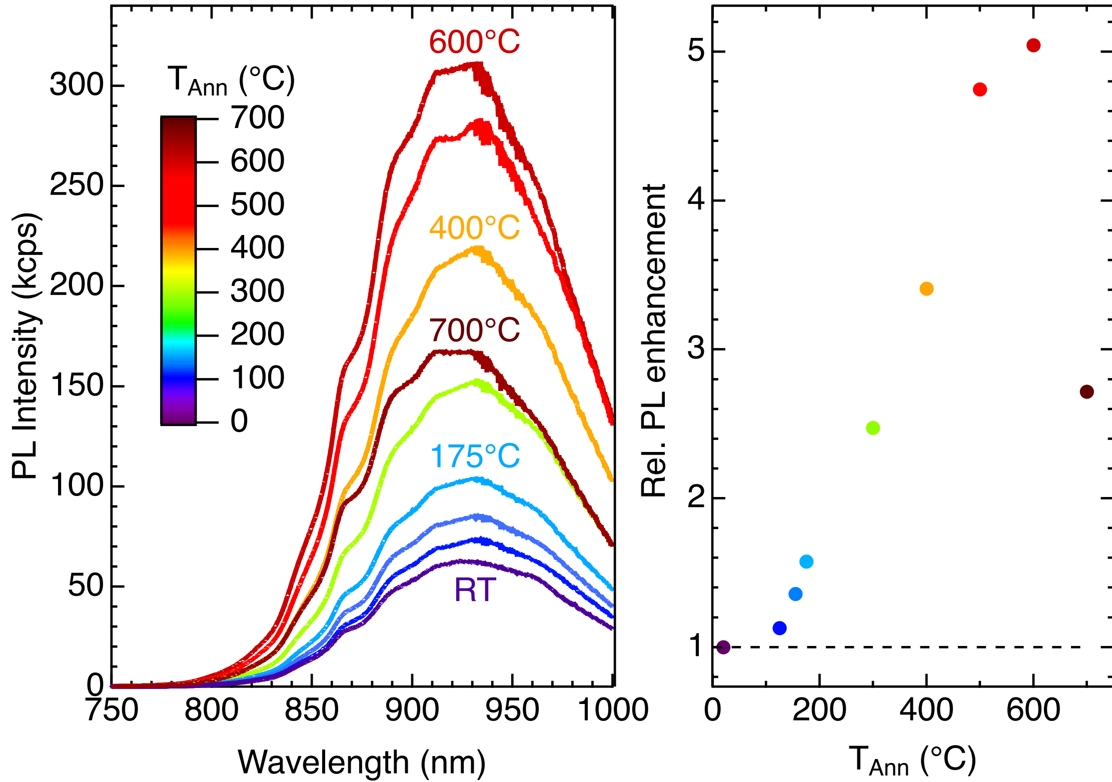

Figure 5.12.: Thermal annealing. Left: PL spectra after thermal annealing steps at increasing temperatures T_{Ann} from 20-700°C. Measured in the LabRAM setup at room temperature with excitation at 633 nm. **Right:** Relative PL enhancement versus annealing temperature T_{Ann} . Depicted is the integral PL from 800-1000 nm relative to the corresponding value before annealing (RT).

The maximal PL increase is reached after annealing at 600 °C, with a PL enhancement factor of 5.5 compared to the PL of the sample before annealing with a defect density of $N_{high} = 7 \cdot 10^{15} cm^{-3}$ (compare figure 5.5). Assuming a linear connection of the defect density and the integral PL, the now enhanced PL corresponds to a defect density of $N_{Ann} = 3.9 \cdot 10^{16} cm^{-3}$.

Discussion of possible annealing mechanisms

The prevailing mechanism leading to PL enhancement via thermal annealing is that heating results in atomic displacements, disappearance (annealing out) or/and transformation of some other types of intrinsic defects, e.g. recombination of Frenkel pairs or migration of interstitials [119]. These defects may serve as non-radiative recombination channels or as charge traps, preventing the radiative recombination via V_{Si} defects in close proximity. If these competing loss-mechanisms are removed, the PL of

V_{Si} gains strength. This proceeds until the V_{Si} mutate into antisite-vacancies or divacancies at elevated temperatures above 600°C.

Another mechanism could be a change of the charge state of the defects, be it V_{Si} or other neighboring defects. If this results in more negatively charged V_{Si}, or less non-radiative recombination channels, this leads also to an increase in PL. Remarkably, the pattern induced by laser illumination (see fig. 5.11) remains over many hours, indicating that a charge state change remains stable in the dark at least on the same time scale. While we cannot exclude a charging effect, the fact that 90% of irradiation induced defects in SiC can be removed upon annealing at 350°C [120] supports the thermal effect to be dominant.

In any case, competing loss-mechanism for the V_{Si} PL are removed. With both types of annealing, it is possible to increase the V_{Si} PL. The enhancement factor is determined by the applied laser power or, respectively, the temperature. The laser annealing showed a maximal PL gain of 25%, whereas the thermal annealing could reach PL gains up to 400% (enhancement factor of 5). Another difference is that the laser annealing operates locally, confined to the laser focus spot of 1-2 µm. The thermal annealing is a global treatment, influencing the PL throughout the whole sample.

Defect engineering – Summary

This chapter showed the controlled creation of V_{Si} in SiC via neutron irradiation. Moreover, the defect density could be varied over eight orders of magnitude and the emitter density as a function of the neutron irradiation fluence was estimated.

On the one hand, at low emitter densities, single defects with photostable room-temperature NIR emission were doubtlessly proven. On the other hand, in the sample with highest emitter density, the huge PL signal could even be improved by factor of 5 via annealing mechanisms. This investigation showed that with precise engineering of spin centers, the same approach can be used for very complementary defect applications. These may range from high density spin ensembles for maser amplifiers down to single spin quantum applications like single photon sources or nanosensing.

6. Electrical excitation in a SiC LED structure

So far the silicon vacancies have been excited by optical means. This chapter shows, that also electrical excitation of V_{Si} is possible. This was probed in a SiC LED structure from our cooperation partners P. G. Baranov and E. N. Mokhov from the Ioffe Institute in St. Petersburg, Russia. The results of this investigation are also published in Scientific Reports [121].

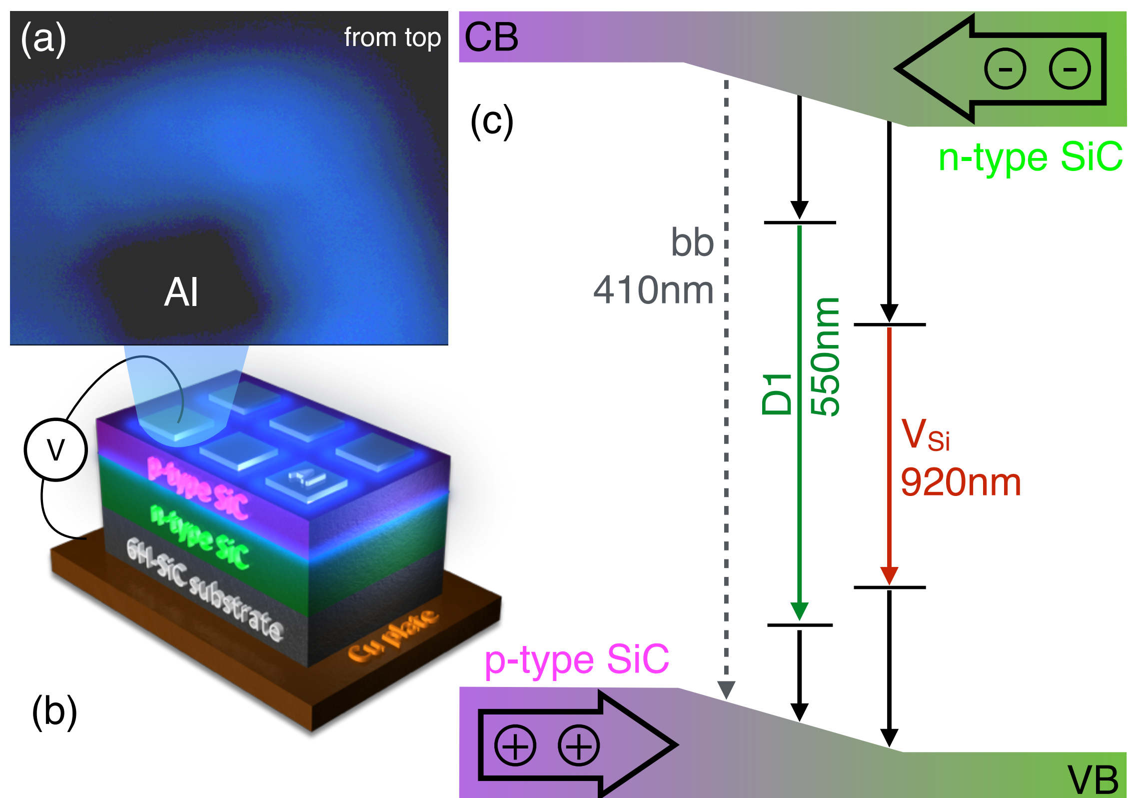

Figure 6.1.: SiC LED with intrinsic defects. **(a)** A picture of the luminous LED around an Al contact. **(b)** A 3-dimensional scheme of the SiC LED (*from H. Kraus with kind permission*). **(c)** Electron-hole recombination through the D1 and V_{Si} defects results in the 550 nm and 920 nm emission bands, respectively. The radiative band-to-band recombination (bb) at 410 nm is inefficient due to the indirect bandgap of SiC.

The LED is an epitaxially grown 6H-SiC single p-n-junction with doping levels of Al: $1 \cdot 10^{20}\mathrm{cm}^{-3}$ and Ga: $2 \cdot 10^{18}\mathrm{cm}^{-3}$ in the p-doped layer and N: $3 \cdot 10^{18}\mathrm{cm}^{-3}$ in the n-doped layer. The p-n-junction has been irradiated with 0.9 MeV electrons of fluence $10^{18}\,\mathrm{e{\cdot}cm}^{-2}$ in order to create defects. Afterwards, aluminum contacts of size $(0.4\mathrm{mm})^2$ have been evaporated onto the surface in a square pattern, creating several LEDs on the device. The top Al electrode can be chosen with a precisely moveable contact needle or with Au wire bonding. We mounted the LED sample on a copper plate serving as the second electrode. A schematic spatial 3-dimensional model of the LED is depicted in figure 6.1 (b). Upon applying voltage between one of the Al contacts and the Cu plate the luminescence glow is seen by bare eye, shown as an image in figure 6.1 (a). Figure 6.1 (c) shows the band schematic with the radiative recombination through defects within the bandgap of SiC. The direct band-to-band recombination bb (around 410 nm for the 6H-SiC bandgap of 3.0 eV) in SiC is unfavorable due to the indirect bandgap. This is the reason why SiC-LEDs, having been used for commercial yellow and blue LEDs until the 1990's, have been replaced by direct semiconductors like GaN. This disadvantage for opto-electronics turns into an advantage in our case, as the radiative recombination via defects is preferred.

The room temperature electroluminescence (EL) spectrum of one of the LEDs is presented in figure 6.2. It consists of two broad emission bands well below the bandgap of 6H-SiC. One lies in the visible range from 450-700 nm (labeled D1) and the other is in the NIR from 850 nm to at least the detection limit at 950 nm. For comparison, the RT PL spectrum with excitation at 633 nm of a reference sample containing V_{Si} is also depicted.

6.1. Emission in the visible range

The emission in the visible range can be attributed to the so called D1 center. The D1 center in 6H-SiC has been already observed in 1972/73 by Patrick and Choyke [111, 122], who suggested an intrinsic defect, most probably a complex due to high formation temperature. They assumed a divacancy as a good model for the D1 center. In 2004, Pinheiro et al. found the $Si_C(C_{Si})_2$ antisite complex as a better candidate for D1 [123]. However, the defect is not clearly identified, as EPR signals could not be observed so far [123]. At 77K, Patrick and Choyke observed three ZPLs between 470 nm and 480 nm and a not well resolved phonon sideband from 482 nm up to 495 nm (end of measurement range) [111]. Low temperature EL measurements at 77 K were also performed on our LED sample in the cryostat. The measured spectrum, depicted in figure 6.3, shows an emission band from 440 nm to 640 nm. Compared to the room tempera-

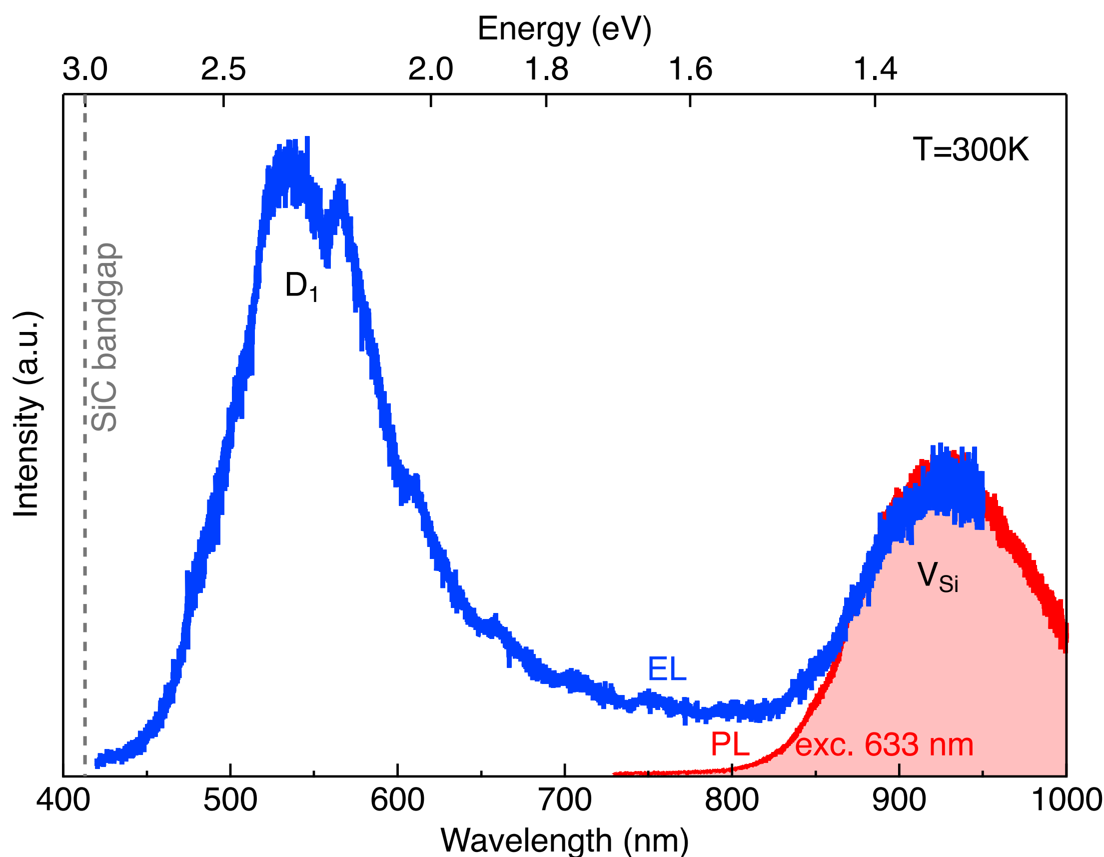

Figure 6.2.: Room temperature EL of defects in SiC. EL spectrum for I=15 mA of the SiC LED and PL spectrum of a reference SiC sample. Both recorded at room temperature in the LabRAM setup. The PL spectrum is excited at 633 nm. The 6H-SiC bandgap is denoted with a vertical dashed line.

ture EL (see figure 6.2), the emission at 77 K is slightly narrowed and blueshifted. Both can be expected due to smaller phononic contribution and a bandgap increase at lower temperatures, which could also affect the defect energy levels. Remarkably, the band emission maximum is located at 477 nm, therefore, although no ZPL can be extracted from the band emission, this is a clear assignment to the D1 center.

Additionally to EL, the low temperature PL of the LED sample in the cryostat at 77 K and under excitation with a 473 nm (2.62 eV) laserdiode was recorded (figure 6.4, turquoise spectrum). Here, several lines between 480 nm (longpass filter cutoff) and 540 nm are visible. The PL maximum is redshifted with respect to the EL maximum as the optical excitation into the maximum of the D1 band (2.62 eV) leads to a Stokes shift. Furthermore, an oscillation with a periodicity of roughly 7 nm is overlaying the spectrum in the high energy range, whose origin is unknown but probably is a measurement artifact. A clear assignment of ZPLs is not possible, as also 6H-SiC Raman lines

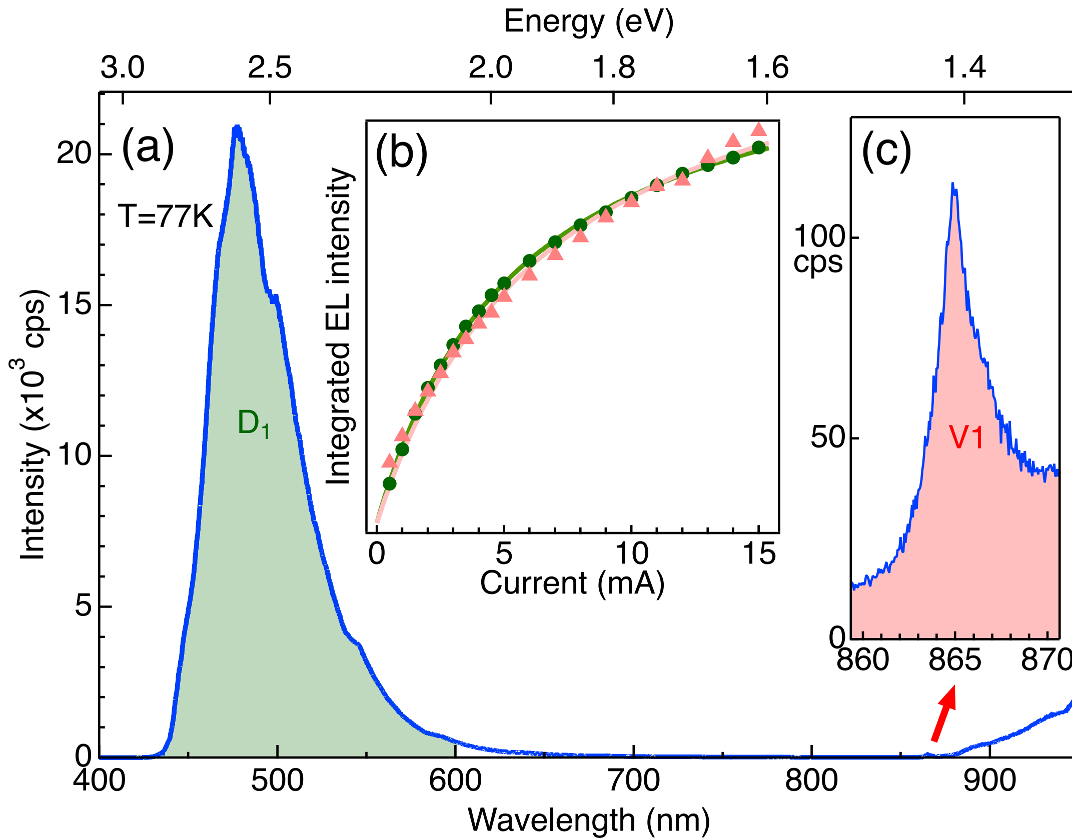

Figure 6.3.: EL at 77 K. (a) EL spectrum of the SiC LED for I=15 mA and 77 K in the LabRAM setup. The V_{Si} EL is magnified in the inset **(c)**. Inset **(b)** shows the EL-current-characteristic for currents from 0-15 mA. The markers are the integrated EL values for the D_1 EL (green) and the V1 EL (red), solid lines are fits (see text for details). The corresponding areas are shaded in (a), the values for V1 are multiplied by 2500.

are expected between 491.4 and 495 nm (corresponding to wavenumbers 789, 797.5 and 967 cm^{-1}).

6.2. NIR emission from V_{Si}

The room temperature NIR EL of the LED coincides with the V_{Si} PL emission (see figure 6.2) of the reference sample, both having a maximum emission wavelength at about 920 nm. PL measurements at low temperature T=77 K in the cryostat (see figure 6.4) clearly prove the optical excitation of V_{Si} as their ZPL can be identified. Excitation with 473 nm leads to emission of the V1 (865 nm) and V3 (906 nm) ZPLs. V2 emission should be at 887 nm but seems to be too weak to be assigned. Excitation at 633 nm (1.96 eV), which is below the D1 emission energy, is more efficient and shows all three ZPLs of the V_{Si}. The EL spectrum (measured at I=15 mA) shows in the NIR region also a peak at the position of V1. Due to a rising slope from 880 nm to the detection limit around 950 nm,

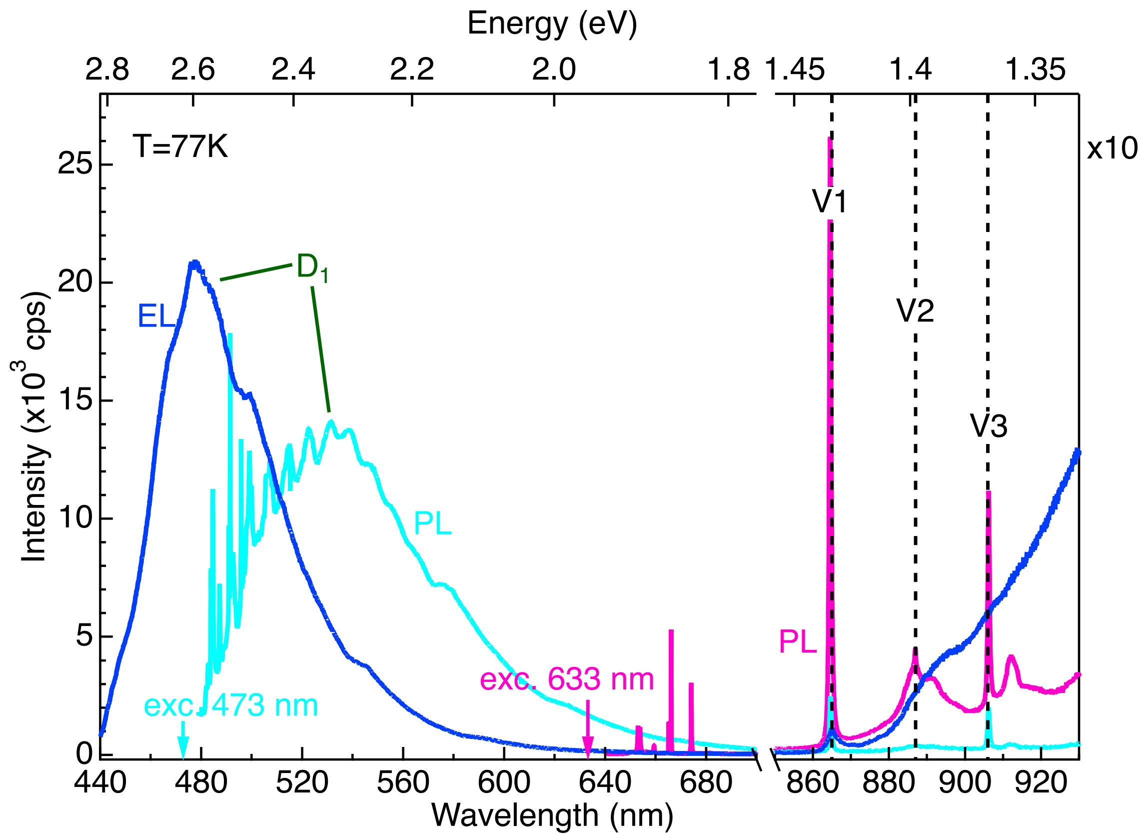

Figure 6.4.: EL and PL spectra at low temperature T=77 K. EL spectrum for I=15 mA. PL spectra, excited at 473 nm (turquoise) and 633 nm (magenta), respectively. In both cases, the SiC Raman lines are also visible. The D_1 emission is in the PL only accessible for exc. 473 nm. Emission intensities in the range from 850-930 nm are multiplied by 10. Here, the V_{Si} emission is visible. ZPLs are denoted with vertical dashed lines: V1 (865 nm), V2 (887 nm) and V3 (906 nm).

the V2 and V3 lines cannot be identified. Nevertheless, the presence of the V1 line in the EL spectrum suggests that the V_{Si} can as well be electrically excited. The ZPL spectral width in EL is larger than in PL, which is probably due to current-induced charge fluctuations in the proximity of the defects, leading to an increase of inhomogeneous broadening.

6.3. Emission and LED characteristic

Both optical and electrical excitation of V_{Si} lead to weaker emission compared to the D1 defect. Especially at low temperature, D1 dominates the spectrum. The reason is the much higher concentration of D1 defects than of silicon vacancies. However, at room temperature most of the D1 defects are ionized due to the thermal activation of defect-bound electrons into the conduction band. This is consistent with a small

activation energy (about 60 meV [124, 125]) of the D1 defect in the polytype 4H. With decreasing temperature, the activation process becomes inefficient and thus more D1 defects contribute to the EL, i.e. the EL intensity increases. On the other hand, the activation energy of the V_{Si} defects is much larger and their intensity weakly depends on temperature. Hence the room temperature EL shows a significant silicon vacancy contribution (see figure 6.2), where the V_{Si} maximum reaches around 50% of the D1 maximum value.

As the V_{Si} emission is at a lower energy than the D1 emission, a re-emission process via D1 is in principle possible. The PL spectrum with excitation into the maximum of the D1 band (at 473 nm, see figure 6.4) shows no significant enhancement of the V_{Si} PL, although the laser intensity per area is several orders of magnitude higher than that of the D1 emission. While this does not exclude re-emission, it verifies that a possible re-emission is inefficient compared to the electrical excitation of the V_{Si}.

Figure 6.3 (a) shows the EL spectrum at T=77 K with a magnification of the V_{Si}(V1) emission in the inset (c). The shaded regions denote integrated EL intensities, that are calculated for various applied currents. This input-output-characteristic for both defect types is displayed in the inset (b). The values for V1 are multiplied by 2500 for better comparison. Both curves show a typical LED characteristic with an onset of saturation of the emission with injection current I. The progression for both defects can be described by the equation $EL(I) \propto \frac{I}{I+I_0}$, shown in figure 6.3 (b) as solid lines. This corresponds to a simple model where the defects' charge carrier capturing rate is proportional to the injection current. From these fits, the characteristic saturation current I_0 can be estimated to I_0=(6.3±0.6) mA. This is higher than that in quantum dot-based single photon LEDs [126] but comparable to an electrically driven NV-based single photon source in diamond, for which Mizuochi et al. found a saturation current of (5.3±0.8) mA [4].

Discussion

This section showed, that intrinsic defects in a SiC device can be electrically driven, resulting in efficient EL with emission energies well below the SiC bandgap. Two spectrally different emission bands can be assigned to different types of defects. The D1 defects show EL in the visible range, which is intense at low temperatures but quenches with rising temperature. The V_{Si} defects emit in NIR even at room temperature.

Electrical excitation is in particular interesting for quantum light sources [127], and especially for single photon sources. As shown in chapter 5, the defect density can be controlled by varying the irradiation dose, which should allow to isolate single emitter.

Electrical excitation of single defects has been shown on the NV-center in diamond [41, 4], on a single organic molecule [128] or on single semiconductor quantum dots [129, 130]. However, all those approaches have drawbacks. The fabrication of electronic devices from diamond is challenging due to its insulating property. Organic molecules are very unstable and show photobleaching and quantum dot emission comes along with the need for low temperatures.

Defects in SiC are advantageous as both the creation of electronic devices from SiC is already well established, and isolated defects in SiC are excellent single photon emitters even at room temperature. These findings open a new way to fabricate cheap and robust LEDs emitting single photons on demand. Indeed, an electrically excited single photon source, even though not V_{Si} based, has been shown recently in a SiC diode [131]. This realization, the optical addressability of single V_{Si} (see chapter 5.2) and the electrical excitation of ensemble V_{Si} suggest that an electrically driven single photon source based on V_{Si} could be feasible.

7. Silicon vacancies in silicon carbide nanocrystals

This chapter describes the production of SiC nanocrystals (NCs) containing silicon vacancies. The small size of the particles, the near infrared emission and the spin properties open a way for interesting applications in the growing field of nanotechnology, especially for bioimaging and nanosensing. Involved in this work are our cooperation partners Prof. P. Baranov (Ioffe Institute, St. Petersburg, Russia), M. Trupke (Vienna Center for Quantum Science and Technology, Atominstitut, TU Wien, Austria), Dr. N. Tarakina (Exp. Physics 3, Julius-Maximilian University of Würzburg, Germany) and Prof A. Krueger and A. Muzha (Institute of Organic Chemistry, Julius-Maximilian University of Würzburg, Germany). The results are published in Applied Physics Letters [47] with equal contribution of first authors Andreas Muzha and myself.

7.1. Nanoparticles and their applications for bioimaging

After a short definition of nanoparticles, some of their general applications are introduced. More specific, the applications of nanocrystals in bioimaging are then described. The section shows furthermore, that SiC NCs are suitable for bioimaging and presents the current research status about defects in SiC NCs.

Nanoparticles

Nanoparticles are small objects with a size of 1 nm up to 100 nm. In this size regime, the transition from the (classical) *macro*world to the (quantum mechanical) *micro*world can be observed. On the nanometer scale, most of the biological scenes run their courses, surfaces and interfaces strongly influence the materials interactions and properties, and finally quantum effects dominate.

Nanocrystals in bioimaging applications

Nanoparticles or NCs for bioimaging applications have to fulfill quite demanding material requirements [132]. The particles should be nontoxic, biocompatible [133] and photostable [134]. Besides, large scale and low cost production capabilities are also an advantage.

There are different nanoparticle systems in use for bioimaging, but mostly they are not meeting all biomedical requirements. For example dye molecules have a narrow absorption window and rapidly photobleach [135]. Quantum dots (QDs) are cytotoxic [136] or potentially toxic and their reproducibility is limited [135].

Therefore, semiconductor nanocrystals, that fulfill the above mentioned requirements, have attracted growing attention as biolabels. SiC NCs without defects were suggested for cancer therapy [137] and [138, chapter 11]. But in those defect-free SiC NCs, the emission is mostly due to surface states or quantum confinement [139] and lies –like for the NV in nanodiamond– in the visible range. For bioimaging applications, NIR emission would be advantageous, as the penetration depth in tissue is higher. For instance, the effective attenuation in biological tissue is ca. 20 times higher for 650 nm than for 850 nm [77]. Besides, biological samples often have autofluorescence in the visible range and scatter light more than in the near infrared (NIR) [76].

Defects in SiC were proposed as biomarkers by Somogyi and Gali in the recent review *Computational design of in vivo biomarkers* [140]. But "*yet no paramagnetic defects have been shown in SiC nanostructures [...]*", according to Castelletto in [74, p. 617]. Only last year, in 2014, she and coauthors changed that with the "*first observation of room temperature single photon emission from 3C-SiC nanoparticles*" [46, p. 7939]. This is to my knowledge the only publication so far with defect based emission in SiC nanoparticles. Yet, the investigated defect is the carbon antisite vacancy pair (C_{Si}-V_C), emitting in the visible range (ZPL: 648nm) in 3C-SiC. And in case of the C_{Si}-V_C, the accessibility with magnetic resonance is not provided.

Concerning both the spectral window and the magnetic resonance, the V_{Si} defects in SiC NCs could be a superior system for bioimaging. They combine the preferable NIR emission and absorption window [112] for optimal tracking in biological tissue with magnetic field sensing [51]. The appeal of such a combined application has also been stated by Castelletto in [74, p. 622]: "*A field that could benefit from the introduction of SiC optical and paramagnetic defects in nanoparticles or QDs, is ultra-sensitive magnetometry in living cells.*"

7.2. SiC nanocrystals (NCs)

This section describes the fabrication process of the NCs and their characterization regarding size and crystallinity.

7.2.1. Fabrication

The fabrication process of the investigated SiC NCs consists of different steps, briefly sketched in figure 7.1.

First, high-quality SiC bulk material is grown via sublimation in argon atmosphere at high temperatures (2500-2600°C), resulting in a very low nitrogen impurity concentration below 10^{16}cm^{-3}. The precursor is a pure SiC powder synthesized from a silicon and carbon mixture of spectral purity, and the SiC crystals are grown on graphite wafers. The growth products are millimeter sized SiC crystals of the polytype 6H.

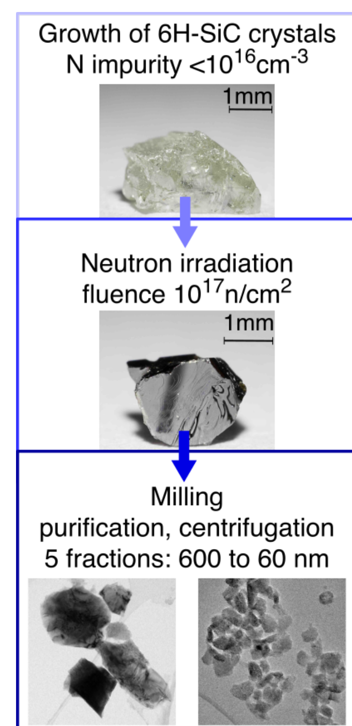

Figure 7.1.: Fabrication process of the SiC nanocrystals.

The second step is irradiation with neutrons with a fluence of 10^{17}cm^{-2} in order to produce silicon vacancy defects. The estimated concentration of generated V_{Si} defects is in the order of 10^{15}cm^{-3}.

Third, the irradiated bulk material passes a high energy wet-milling process in a vibration mill, cleaving the lattice bonds and crushing the millimeter thick SiC bulk pieces into small particles down to the nanometer scale. This process is similar to the production of nanodiamonds, e.g. reported in [42, 141]. Steel milling beads are employed, although SiC is harder. The steel contamination can be removed with a magnet and afterwards dissolving the residues in acid. The milled particles are all in a size well below 1 µm. The resulting purified particle suspension is stabilized with aqueous ammonia to adjust the pH into the stability window of the colloid. Afterwards, the suspension is centrifuged, separating five fractions with mean NC sizes of 600 nm, 200 nm, 140 nm, 120 nm and 60 nm.

7.2.2. Characterization

The fabricated SiC NCs were investigated in terms of their size and structure.

For standard optical microscopy, the aqueous solution was dropcast on silicon wafers and dried at room temperature. Photographs of these dried droplets through an optical microscope (depicted in figure 7.2) show an inhomogeneous coating of the substrate. The dried droplets have a thick outer fringe (known as coffee stain effect)

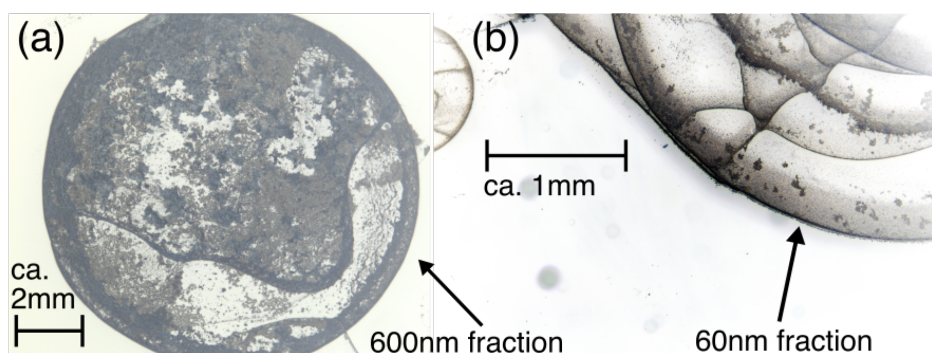

Figure 7.2.: Photographs of dropcast samples. Pictures of **(a)** the biggest fraction (600 nm) and **(b)** the smallest fraction (60 nm) were taken with a digital camera through an optical microscope. Shown in inverted colors. The photos demonstrate the uneven distribution of the colloid after drying (coffee stain effect and clustering).

and inhomogeneously distributed particles inside the drop. Figure 7.2 shows clusters of NCs, but also spots, where the substrate is uncovered. This holds in principle for all fractions, but with decreasing NC size, also the clustering decreases (compare fig. 7.2 (a) for the 600nm fraction with (b) for the 60nm fraction).

The size distribution of the particles was characterized with dynamic light scattering (DLS) in solution. Besides, structural investigations in a transmission electron microscope (TEM) were carried out.

In figure 7.3, the particle size distributions for the fractions 60, 140, 200 and 600 nm are depicted. The mean size is increasing and serves as name for each fraction. Also the widths differ and some distributions are asymmetric, which is a result of the centrifugation process. Additionally for the 60, 140 and 600 nm fraction, TEM pictures are displayed in the insets. The edges of the NCs are rounded due to the acid etching during purification.The scales show that the sizes of the NCs in each TEM picture correspond very well with the expectation from the DLS measurement.

High resolution (HR)TEM pictures have been recorded for the 60, 140 and 600 nm samples (see figure 7.4), in order to reveal the crystal quality and the lattice constants. The latter can be indexed in a hexagonal lattice with unit cell parameters a = 3.08Å and c = 15.2Å for all different fractions, perfectly in line with literature values for 6H-SiC [20, 142]. The direction of the c-axis is indicated with an arrow in subfigures 7.4(b, d, f).

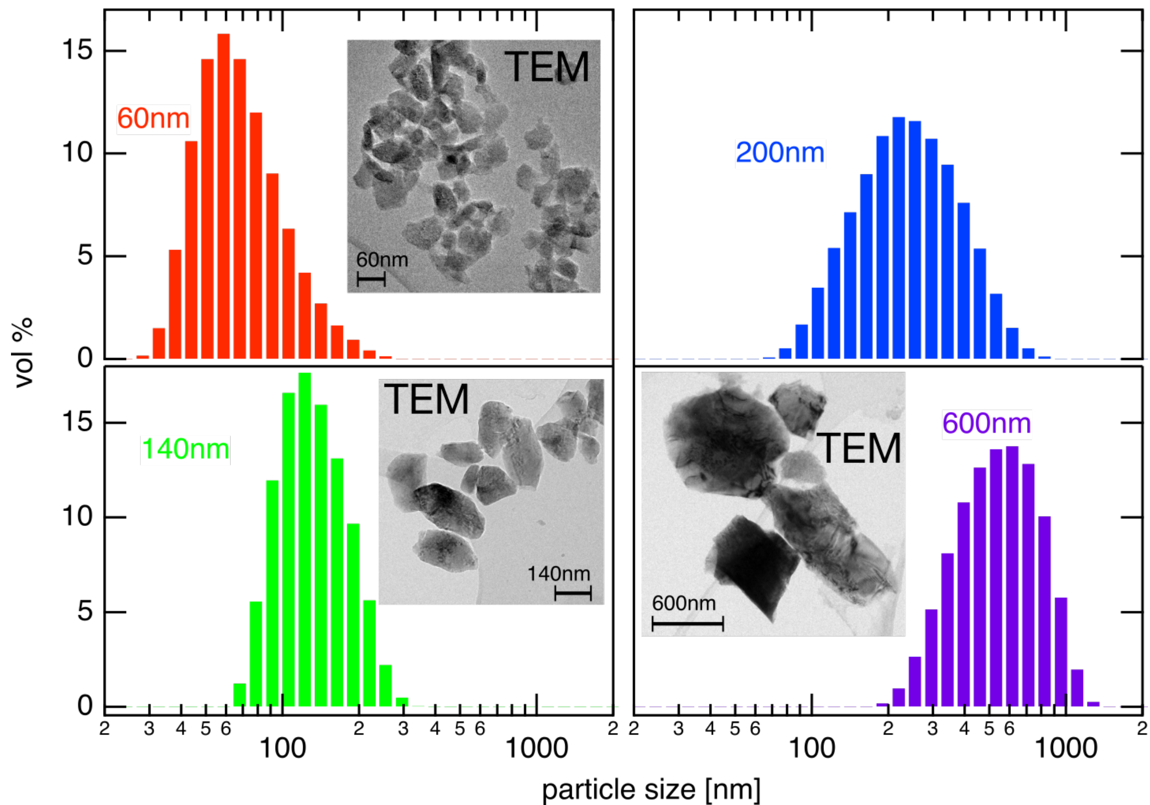

Figure 7.3.: Size distributions and TEM of milled SiC particles. The histograms show the size distributions from dynamic light scattering measurements of aqueous colloids of the fractions 60, 140, 200 and 600 nm. The insets for 60,140 and 600 nm are TEM pictures, each scale bar corresponds to the respective mean size, giving the name of the fraction. *The DLS measurements were carried out by A. Muzha, the TEM measurements by N. Tarakina.*

The round edges of the NCs (see also TEM images in figure 7.3) have a rather amorphous fringe. Except of this surface layer, the HRTEM images from the 600nm fraction (figure 7.4(a, b)) show an almost perfect atomic structure, corresponding to the 6H-SiC polytype. The amorphous layer of approximately 2 nm thickness is also found at the edges of the NCs from the 140nm fraction (see 7.4(c, d)). Additional selected area electron diffraction measurements (not shown) support the good crystalline quality. Although the quality of the NCs in total is still very high, some defects are visible in HRTEM images. The areas encircled in red in subfigures 7.4(a) and (c) denote an edge dislocation and respectively a grain boundary. In the smallest, 60nm fraction, the HRTEM images show clusters with highly crystalline NCs of about 10 nm in size, surrounded by rather amorphous material (see 7.4(f), indicated by dashed yellow line). The NC quality within such clusters is comparable with that of bigger crystals. Our model for this kind of cluster formation is that during milling new structural defects

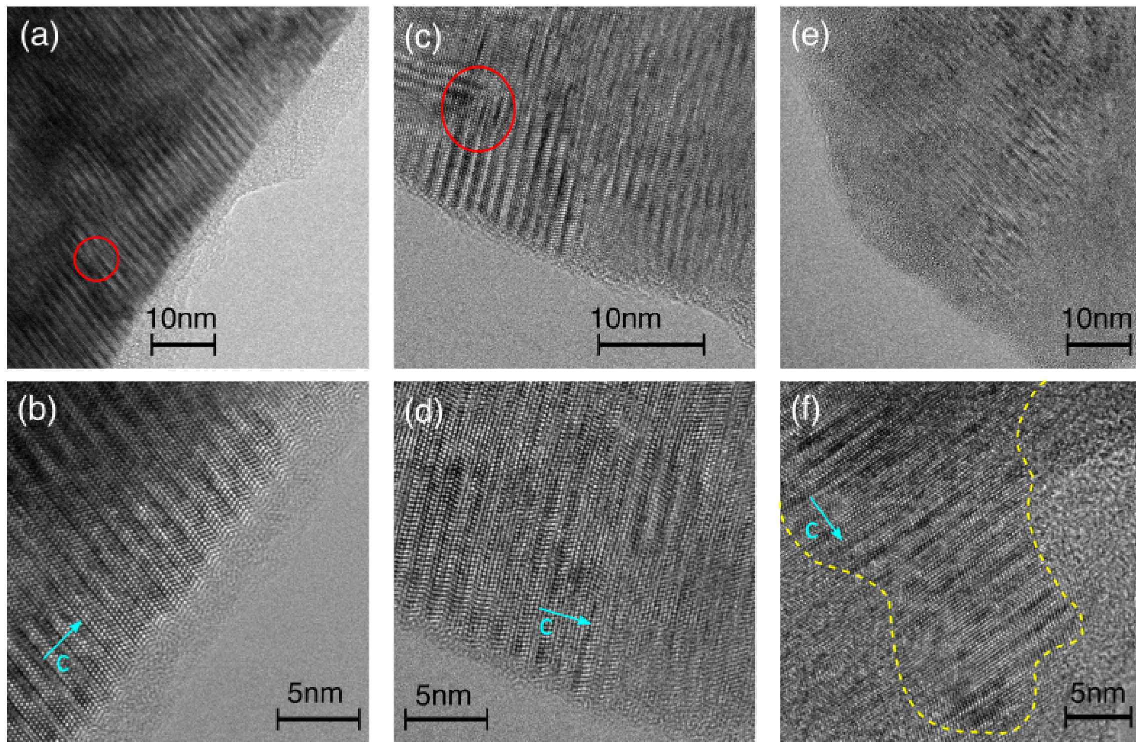

Figure 7.4.: HRTEM characterization of NCs. The HRTEM images belong to the fractions 600nm **(a,b)**, 140nm **(c, d)** and 60nm **(e, f)**. An amorphous surface layer surrounds the NCs. The otherwise good crystallinity is visible in the regular 6H-SiC zig-zag-pattern; the lattice c-direction is indicated in (b, d, f) with turquoise arrows. Lattice imperfections are encircled in red (a, c). The yellow dashed line in (f) indicates the border between crystalline NC and amorphous surrounding. *The measurements were carried out by N. Tarakina.*

tend to appear near existing ones, forming defect (amorphous) areas around the highly crystalline residuals.

Summarizing, the DLS measurements prove that we have an representative series of NCs with mean sizes ranging from 60 nm to 600 nm, i.e from the nanometer to the sub micron level. With electron microscopy methods, the good crystal quality of the NCs, although slightly suffering from the milling and purification process, was assured.

7.3. Photoluminescence of silicon vacancies in SiC NCs

This section is dedicated to the PL and ODMR investigations of the SiC NCs. The photoluminescence of all samples except the 120 nm fraction[1] is measured at different tem-

[1]Due to sample inhomogeneity (see fig. 7.2), not every characterization method yields good results in all fractions. No reasonable PL spectra could be obtained for the 120 nm fraction, therefore the PL

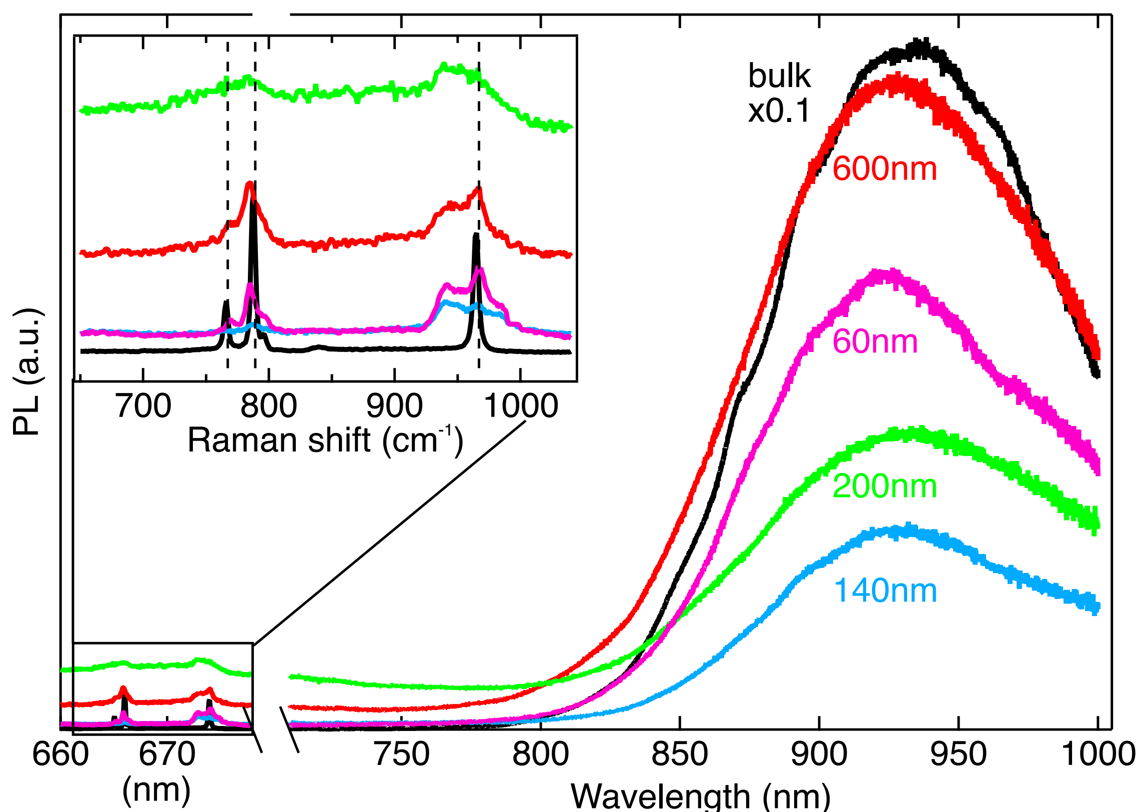

Figure 7.5.: PL of SiC NC fractions at room temperature (RT). Excitation at 632.8 nm. All fractions show NIR emission from 800-1000 nm. For comparison, the pre-milling bulk PL spectrum (multiplied with 0.1) is shown in black. Between 664 and 674 nm, three 6H-SiC Raman lines, located at 789 cm^{-1}, 797.5 cm^{-1} and 967 cm^{-1}, are identified. The inset shows a zoom in the Raman lines (indicated with vertical dashed lines) with the usual wavenumber axis.

peratures and is compared with the photoluminescence of the neutron-irradiated bulk before milling. The PL is measured in the LabRAM spectrometer with excitation with the He-Ne laser at 632.8 nm (1.96 eV). For room temperature (RT) measurements, the 100x magnification is used, whereas the measurements at lower temperature are done with the 50xLWD (long working distance) objective. All fractions show photoluminescence in the NIR at room temperature with a similar shape as the bulk PL (see figure 7.5). The bulk PL intensity is about one order of magnitude stronger, which can be explained with the milling process. The bond cleavage preferentially occurs at the least stable bonding environments, i.e. defective lattice sites. This results in a considerable loss of the amount of silicon vacancies in the resulting NCs. From the comparison of the PL intensities, one can roughly estimate that at least 10% of defects from the initial concentration are still present in the smallest NCs.

evaluation skips this fraction. But still the other fractions give a representative series of variation in NC size.

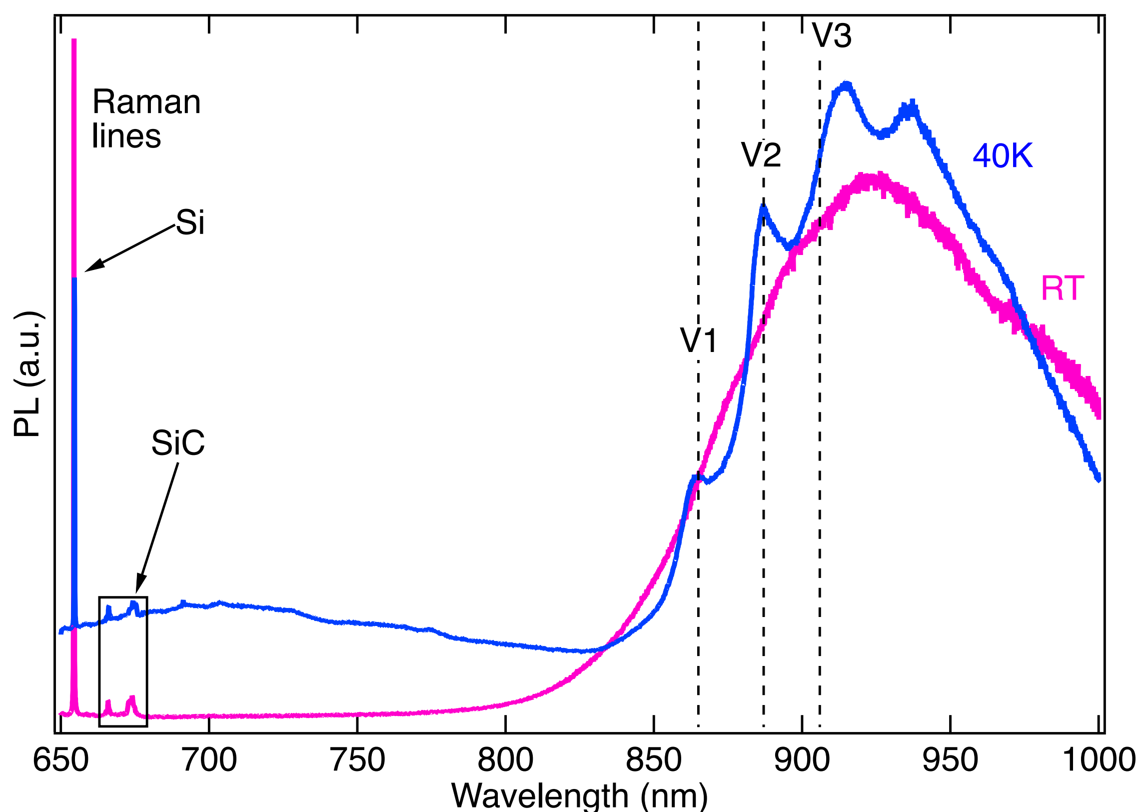

Figure 7.6.: PL of SiC NCs 60 nm fraction at different temperatures. Excitation with 632.8 nm at RT (pink) and at T=40 K (blue), where the V_{Si} ZPLs are more pronounced. Their respective positions at 865 nm, 887 nm and 906 nm are indicated by vertical dashed lines. Also the Si Raman line of the substrate at 654 nm is prominent, which is for clarity omitted in fig. 7.5. The presence of SiC Raman lines ensures that the measurements were performed on SiC NCs.

The PL spectrum of the bulk crystal consists of a broad emission band of V_{Si} defects from 850 nm to above 1000 nm. This PL signature is not observed in the as-grown crystals, but appears after neutron-irradiation (see chapter 4.1). At shorter wavelengths (664–674 nm), three Raman lines can be observed. Converted into the more common wavenumbers $\tilde{\nu}$, $[\tilde{\nu}]$=cm^{-1}, the lines are in agreement with the spectroscopic Raman fingerprint of polytype 6H: 789 cm^{-1}, 797.5 cm^{-1} and 967 cm^{-1} [143] (indicated by vertical dashed lines in the inset of fig. 7.5). The observed narrow line width is typical for high-quality bulk SiC. The Raman lines can also be seen in the PL spectra of the NC fractions, but are broadened due to lower crystal quality of the milled material. But especially here they are useful, as the presence of the Raman lines in a PL spectrum ensures that the measured signal is coming from SiC nanocrystals. This is needed due to the inhomogeneous NC distribution on the Si substrate (compare figure 7.2 in section 7.2.2).

The indication, that the NIR emission is due to V_{Si} defects can be verified with PL measurements at lower temperature, shown in figure 7.6 for the smallest, 60 nm fraction. In the 40 K spectrum the ZPLs can clearly be distinguished from the broad phonon sideband compared to the also shown room temperature measurement. The observed three ZPL peaks correspond to the well-established V1 (865 nm), V2 (887 nm), and V3 (906 nm) ZPLs of V_{Si} in 6H-SiC (compare table 2.2 in chapter 2.3.2), proving the silicon vacancy defects to be the origin of the NIR emission.

All in all, the photoluminescence measurements prove that the SiC nanocrystals still contain defects, in particular silicon vacancies, with emission in the near infrared.

7.4. ODMR of silicon vacancies in SiC NCs

Zero-field optically detected magnetic resonance at room-temperature can be demonstrated in these NCs – at least in the submicron particles of the 600 nm fraction. The measurements are described in this section and the findings will then be discussed with respect to possible applications.

The spectra of the pre-milling bulk sample and the 600nm fraction are shown in figure 7.7. The zfODMR measurements are taken in the home-built zfODMR setup with 785 nm optical excitation and RF power of 16 dBm (=40 mW). The ODMR signal is the relative PL change as a function of applied radio frequency. A piece of bulk material before milling serves as a reference sample (black curve). Its spectrum shows several sharp ODMR lines due to ZFS of irradiation-induced defects. The main peaks can be located at 31 MHz and 129 MHz with negative and positive ODMR contrast respectively. This is in good agreement with the spin resonances of silicon vacancies in 6H-SiC reported in literature (see table 7.1).

Source	[92]	[72]	[51]	pre-milling bulk	600nm NCs
Lines V1 & V3 [MHz]	27.6	27	28	31	48.7
Line V2 [MHz]	128.4	127	128	129	134.2

Table 7.1.: Zero field splitting 2D/h of silicon vacancies in 6H-SiC. Values from literature for comparison are shown. The right two columns show the values from measurements of pre-milling bulk material and of the 600 nm fraction NCs.

Additionally, there are two side peaks next to both the 31 and 129 MHz peaks, that cannot be explained by the hyperfine interaction (HFI). Their distance from the main peaks is between 15 and 18 MHz, which does neither fit to coupling with ^{29}Si on a next nearest neighbor site (HFI coupling constant 8.7 MHz [92, 144]) nor to coupling with an adjacent ^{13}C (HFI coupling constant >27MHz [144]). Additionally the intensity is too

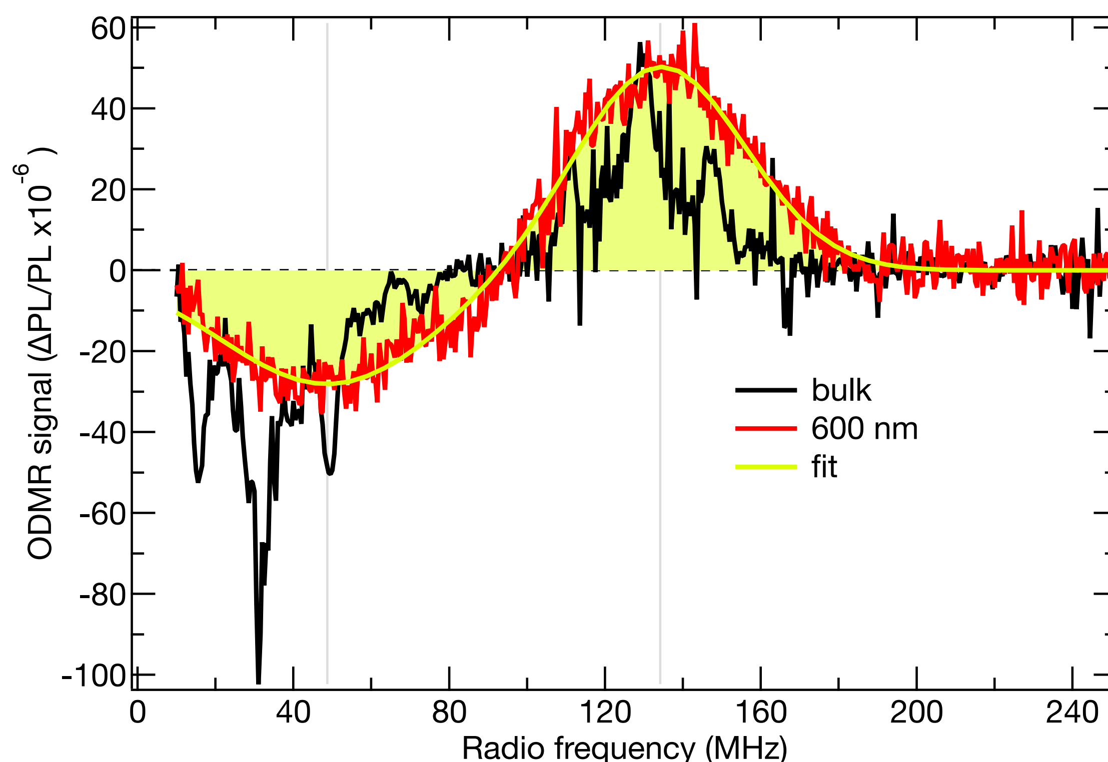

Figure 7.7.: zfODMR in milled SiC particles. Excitation at RT with 785 nm and 16dBm RF power. The ODMR spectra of pre-milled bulk (black) and 600 nm fraction nanocrystals (red) show the resonances of V_{Si}. The resonances in the milled manifold are significantly broadened and can be fitted with two Gaussian peaks (solid yellow-green line, filled to zero).

strong. The expected intensity ratio of the HFI peak for the interaction with one ^{29}Si and the main peak is 0.27 [144], while we have here an intensity ratio of 0.5. Similar observations were made by Widmann et al. in [11, fig. S6] for silicon vacancies in 4H-SiC. Despite the different polytype, leading to different ZFS and hence resonance frequencies, the fine structure can be compared in relation to the respective main peak structure. The zfODMR ensemble measurement [11, fig. S6(b)] shows a multipeak structure with 4 satellite lines around the 64 MHz main peak. The inner satellites have a distance of 13 MHz to the central resonance, the outer lines have distances of 21 respectively 26 MHz. Widmann et al. show similar multipeaks also in a single spin ODMR measurement in a weak magnetic field, with distances from the main peak of 14, 11 and 25 MHz. However the reason for this fine structure is still under discussion.

A working model for this is level splitting due to local magnetic field from paramagnetic centers or clusters. The PL measurements show, e.g. in figure 7.6 for T=40 K around 680-750 nm, that there are other kinds of defects present in the sample. Hence this suggestion is not far off, but still the origin of these side peaks is unknown.

In the ODMR spectrum of the 600 nm NC fraction, two main resonances are visible (red curve in fig. 7.7). They are broadened and blue-shifted in comparison to the bulk ODMR spectrum, but in principle resemble the bulk's main resonances. The broadening of the ODMR peaks is due to a variation of the ZFS parameter D for individual defects, which is in turn caused by inhomogeneities in the defects' surroundings. This is not surprising as the material went through the milling process, destroying the macroscopic crystal structure and also leading to variation in NC size, which could in part be eliminated by centrifugation, but each fraction still has a distribution of different NC sizes (see fig. 7.3).

The key point is the location of the vacancy: deep in the NC, the behavior of the defect should be like in the bulk. But if the defect is near the surface of the NC or even in the amorphous layer surrounding the NC, the defect's environment is not perfectly crystalline anymore, thus the interaction changes and with it the ZFS of this defect. As this effect is individual for each defect, the broadening should be inhomogeneous, and also increase with decreasing NC size (due to larger surface-to-volume ratio and more extended amorphous regions). To prove the inhomogeneous nature of the broadening, the ODMR spectrum of the 600 nm fraction is fitted with two Gaussian peaks, displayed in figure 7.7. The fit parameters are shown in table 7.2.

In the fractions with smaller NCs, no ODMR signal is detected. We suspect that the increasing inhomogeneity with smaller crystal size, leads to broader resonances, that cannot be resolved any more. Additionally, the smaller the fractions are, the less material is in the excited volume, and so the overall PL is weaker, making ODMR measurement more complicated. This can be seen in figure 7.6, where the 600 nm PL is much stronger than the PL of the smaller fractions. All in all, the ODMR measurement show that the magnetic resonance of defects in silicon carbide is not only observed in the bulk material, but also in the milled specimen, at least in the sub-micron scale. From the resonance positions, the ODMR signal in the 600 nm fraction can be assumed to originate from the silicon vacancies.

	Location f_c [MHz]	FWHM [MHz]
peak 1	48.7±0.84	64.7±2.7
peak 2	134.2±0.42	51.0±1.0

Table 7.2.: Fit parameters and FWHM of the Gaussian peaks for the fit of the zfODMR spectrum of the 600 nm fraction NCs shown in figure 7.7.

Discussion

This chapter demonstrated the fabrication of sub micron silicon carbide particles down to SiC nanocrystals via a mechanical milling routine compatible with large-scale production. This alone is a novelty compared to the previous electrochemical methods, like etching of bulk SiC, e.g. reviewed in [74]. The smallest particles consist of clusters of nanocrystals of good crystalline quality with a typical size of 10nm. In agreement with the theoretical prediction [140], the irradiation introduced defects are stable in the NCs. For the first time *in SiC nanocrystals*, it has been shown that silicon vacancy defects exhibit both near infrared emission as well as magnetic resonance.

For bioimaging applications, the NIR emission of V_{Si} is advantageous, as it is lying in the tissue transmission window. Additionally the magnetic resonance makes V_{Si} attractive for sensing applications [51], and in combination with embedding in SiC NCs, quantum sensing of *local* magnetic fields with V_{Si} seems feasible.

8. Summary

In this work, we shed light on different aspects of the silicon vacancy in SiC: (i) defect creation via irradiation and optical properties, (ii) defect engineering (iii) electrical excitation of defects and (iv) silicon vacancies in SiC nanocrystals.

The first part illustrated defect creation via irradiation, concluding that both electron and neutron irradiation are suitable for the creation of V_{Si}. Furthermore, two important optical properties of the V_{Si} could be discovered: First, the excitation of the V_{Si} is most efficient at excitation wavelengths between 720 nm and 800 nm. Second, the PL decay yields a characteristic excited state lifetime of (6.3±0.6) ns.

The second aspect is the controlled creation of V_{Si} in SiC via neutron irradiation. With varying neutron fluence, the defect density could be engineered over eight orders of magnitude, with an estimation of the emitter density as a function of the neutron irradiation fluence. This huge defect density variation shows that the same approach can be used for very complementary defect applications.

On the one hand, in the sample with highest emitter density, the huge PL signal could even be enhanced by factor of five via annealing mechanisms. In a device with such a high V_{Si} density, a room temperature MASER could be established. Its prerequisite, the stimulated emission of microwaves, has already been shown in our group [81].

On the other hand, in the low defect density samples, single defects with photostable room temperature NIR emission were doubtlessly proven. Their lifetime of around 7 ns confirmed the value of the transient measurement. The average lifetime of the excited state can thus be given as τ=(6.5±1.0) ns. Single defects, emitting photons on demand even at room temperature, are sought-after subjects for various quantum information applications, like quantum computing and cryptography or quantum metrology.

The third part demonstrated, that intrinsic defects can not only be optically but as well electrically excited in a SiC LED structure. Defects in SiC are advantageous as the creation of electronic devices from SiC is already well established, and isolated defects in SiC are ideal single photon emitters even at room temperature. The combination of both opens a new way to fabricate cheap and robust LEDs emitting single photons on demand. Recently, a publication by Lohrmann and coworkers showed an electri-

cally driven defect based single photon source operating at room temperature in a SiC device [131].

The fourth investigation revealed for the first time that V_{Si} can even exist SiC nanocrystals down to sizes of about 60 nm. The substructure of these NCs suggests, that a separation into 10 nm-sized crystals should be feasible. The stability of V_{Si} in SiC NCs should be provided even down to 2 nm-sized crystals, according to theory [145]. The V_{Si} in the NCs show stable PL emission in the NIR and even magnetic resonance in the 600 nm fraction. For bioimaging applications, the NIR emission of V_{Si} is advantageous, as it's lying in the tissue transmission window. Additionally the magnetic resonance makes V_{Si} attractive for sensing applications. The combination of biolabeling and nanosensing with V_{Si} embedded in SiC NCs opens intriguing perspectives, e.g. quantum sensing of neuron activity (the magnetic field is generated due to electric pulses between neurons).

In conclusion, we ascertained on the one hand basic properties of the silicon vacancy in silicon carbide. On the other hand, proof-of-principle measurements tested the potential for various defect-based applications of V_{Si} in SiC, and confirmed the feasibility of e.g. electrically driven single photon sources or nanosensing applications in the near future.

Zusammenfassung

In dieser Arbeit wurden verschiedene Aspekte der Silizium-Fehlstelle in SiC beleuchtet: (i) die Erzeugung der Defekte durch Bestrahlung und deren optische Eigenschaften, (ii) Maßschneidern der Defektdichte, (iii) elektrische Anregung der Defekte und (iv) V_{Si} in SiC Nanokristallen.

Der erste Teil veranschaulicht die Defekterzeugung mittels Bestrahlung, die im Falle der V_{Si} sowohl mit Neutronen als auch mit Elektronen geschehen kann. Des Weiteren wurden zwei wichtige optische Eigenschaften der V_{Si} herausgefunden: Erstens ist die Anregung der V_{Si} im Bereich von 720 nm bis 800 nm am effizientesten. Zweitens zeigt das Abklingen der PL eine charakteristische Lebensdauer des angeregten Zustands von (6.3±0.6) ns.

Der zweite Aspekt ist die kontrollierte Erzeugung der V_{Si} in SiC durch Neutronenbestrahlung. Dabei konnte die Defektdichte über den Neutronenfluss gezielt über acht Größenordnungen verändert, sowie die Defektdichte als Funktion des Bestrahlungsflusses abgeschätzt werden. Diese enorme Dichtevariation zeigt, dass derselbe Prozesses für unterschiedlichste Anwendungen genutzt werden kann. Auf der einen Seite, in der Probe mit der höchsten Defektdichte, konnte das ohnehin schon große PL Signal noch um den Faktor fünf durch Temperprozesse erhöht werden. Solch eine Probe könnte man für einen Raumtemperatur-MASER nutzen. Eine Grundvoraussetzung dafür, die stimulierte Mikrowellenemission, wurde schon in unserer Gruppe gezeigt [81]. Auf der anderen Seite konnten in den Proben mit geringer Defektdichte einzelne Defekte mit stabiler nahinfrarot Emission bei Raumtemperatur zweifelsfrei nachgewiesen werden. Ihre Lebensdauer von etwa 7 ns bestätigt den Wert aus den transienten Messungen. Die durchschnittliche Lebensdauer kann demnach mit τ=(6.5±1.0) ns angegeben werden. Einzelne Defekte, die bei Raumtemperatur Photonen auf Abruf aussenden, sind gefragte Objekte für verschiedene Anwendungen in der Quanteninformation, wie etwa Quantencomputer und -kryptographie oder Quantenmesstechnik.

Der dritte Teil zeigt auf, dass intrinsische Defekte nicht nur optisch sondern in einer SiC LED Struktur auch elektrisch angeregt werden können. Da die Herstellungstechnologie weit entwickelt ist, eignet sich SiC hervorragend für elektronische Bauteile, und einzelne Defekte in SiC sind ideale Einzelphotonenemitter, sogar bei Raumtemperatur. Die Kombination beider Aspekte eröffnet einen neuen Weg, günstige und robuste LEDs herzustellen, die einzelne Photonen auf Abruf emittieren. Und in der Tat wurde kürzlich in einer Veröffentlichung von Lohrmann et al. eine elektrisch be-

triebene Defekt basierte Einzelphotonenquelle in SiC gezeigt, die bei Raumtemperatur funktioniert [131].

Die vierte Untersuchung zeigte zum ersten Mal, dass V_{Si} in SiC Nanokristallen bis hinunter zu einer Größe von ca. 60 nm existieren können. Die Substruktur der NCs legt nahe, dass eine weitere Verkleinerung in Kristalle auf 10 nm Größe möglich sein sollte. Die V_{Si} in NCs sollten theoretisch auch in 2 nm kleinen Kristallen noch stabil sein [145]. Die Defekte zeigen stabile PL Emission im Nahinfraroten und sogar Magnetresonanz in der 600 nm Fraktion. Die NIR Emission ist vorteilhaft für Anwendungen zur Bildgebung in biologischem Material, weil dessen Transmissionsfenster im NIR liegt. Zusätzlich lässt sich die Fehlstelle auch als (Magnetfeld-)Sensor benutzen. Mit den V_{Si} in SiC NCs kann die Kombination eines Biolabels mit einem Miniatursensor gelingen und eröffnet faszinierende Ausblicke, z.B. auf einen Quanten-Sensor lokaler Magnetfelder von Neuronen.

Zusammenfassend haben wir zum Einen grundlegende Eigenschaften der Silizium-Fehlstelle in Siliziumkarbid herausgefunden. Zum Anderen konnten Messungen zur Machbarkeit von verschiedenen Anwendungen sowohl das Potenzial von V_{Si} in SiC für defektbasierte Anwendungen aufzeigen, als auch die Umsetzbarkeit von z.B. elektrisch betriebenen Einzelphotonenquellen oder Nanosensoren in naher Zukunft bestätigen.

Bibliography

[1] R. P. Feynman. Simulating physics with computers. *International Journal of Theoretical Physics*, **21**, 6-7, 467 (1982). doi: 10.1007/BF02650179.

[2] M. A. Nielsen and I. L. Chuang. *Quantum Computing and Quantum Information*. Cambridge University Press (2010). ISBN 978-1-107-00217-3.

[3] D. P. DiVincenzo. The physical implementation of quantum computation. *Progress of Physics*, **48**, 9-11, 771 (2000). doi: 10.1002/1521-3978(200009)48.

[4] N. Mizuochi, T. Makino, H. Kato, D. Takeuchi, M. Ogura, H. Okushi, M. Nothaft, P. Neumann, A. Gali, F. Jelezko, J. Wrachtrup and S. Yamasaki. Electrically driven single-photon source at room temperature in diamond. *Nature Photonics*, **6**, 5, 299 (2012). doi: 10.1038/nphoton.2012.75.

[5] C. Zu, W. B. Wang, L. He, W. G. Zhang, C. Y. Dai, F. Wang and L. M. Duan. Experimental realization of universal geometric quantum gates with solid-state spins. *Nature*, **514**, 7520, 72 (2014). doi: 10.1038/nature13729.

[6] H. Bernien, B. Hensen, W. Pfaff, G. Koolstra, M. S. Blok, L. Robledo, T. H. Taminiau, M. Markham, D. J. Twitchen, L. Childress and R. Hanson. Heralded entanglement between solid-state qubits separated by three metres. *Nature*, **497**, 7447, 86 (2013). doi: 10.1038/nature12016.

[7] G. Kucsko, P. C. Maurer, N. Y. Yao, M. Kubo, H. J. Noh, P. K. Lo, H. Park and M. D. Lukin. Nanometre-scale thermometry in a living cell. *Nature*, **500**, 7460, 54 (2013). doi: 10.1038/nature12373.

[8] T. Staudacher, F. Shi, S. Pezzagna, J. Meijer, J. Du, C. A. Meriles, F. Reinhard and J. Wrachtrup. Nuclear Magnetic Resonance Spectroscopy on a (5-Nanometer)3 Sample Volume. *Science*, **339**, 6119, 561 (2013). doi: 10.1126/science.1231675.

[9] H. J. Mamin, M. Kim, M. H. Sherwood, C. T. Rettner, K. Ohno, D. D. Awschalom and D. Rugar. Nanoscale Nuclear Magnetic Resonance with a Nitrogen-Vacancy Spin Sensor. *Science*, **339**, 6119, 557 (2013). doi: 10.1126/science.1231540.

[10] L. P. McGuinness, Y. Yan, A. Stacey, D. A. Simpson, L. T. Hall, D. Maclaurin, S. Prawer, P. Mulvaney, J. Wrachtrup, F. Caruso, R. E. Scholten and L. C. L. Hollenberg. Quantum measurement and orientation tracking of fluorescent nanodiamonds inside living cells. *Nature Nanotechnology*, **6**, 6, 358 (2011). doi: 10.1038/nnano.2011.64.

[11] M. Widmann, S.-Y. Lee, T. Rendler, N. T. Son, H. Fedder, S. Paik, L.-P. Yang, N. Zhao, S. Yang, I. Booker, A. Denisenko, M. Jamali, S. A. Momenzadeh, I. Gerhardt, T. Ohshima, A. Gali, E. Janzén and J. Wrachtrup. Coherent control of single spins in silicon carbide at room temperature. *Nature Materials* (2014). doi: 10.1038/nmat4145.

[12] D. J. Christle, A. L. Falk, P. Andrich, P. V. Klimov, J. u. Hassan, N. T. Son, E. Janzén, T. Ohshima and D. D. Awschalom. Isolated electron spins in silicon carbide with millisecond coherence times. *Nature Materials*, 1–11 (2014). doi: 10.1038/nmat4144.

[13] R. M. Hazen, R. T. Downs, A. P. Jones and L. Kah. Carbon Mineralogy and Crystal Chemistry. *Reviews in Mineralogy and Geochemistry*, **75**, 1, 7 (2013). doi: 10.2138/rmg.2013.75.2.

[14] J. Kelly. *http://img.chem.ucl.ac.uk/www/kelly/moissanite.htm*. Web. 08.07.2015. A brief history of SiC (2006).

[15] E. G. Acheson. US Patent 0492767: Production of artificial crystalline carbonaceous materials. US Patent Office (1893).

[16] H. Moissan. Nouvelles recherches sur la météorite de Cañon Diablo. *Comptes rendus hebdomadaires des séances de l'Académie des sciences*, 773–780 (1904).

[17] W. J. Choyke and G. Pensl. Siliciumkarbid - Halbleiter fur die neunziger Jahre. *Physikalische Blätter*, **3**, 1 (1991).

[18] J. Boyd. http://spectrum.ieee.org/semiconductors/devices/silicon-carbide-ready-to-run-the-rails. *Silicon carbide ready to run the rails* (2013).

[19] C. E. Hunter and D. Verbiest. US Patent 5723391: Silicon carbide gemstones. US Patent Office (1998).

[20] M. Shur, M. Levinshtein and S. Rumyantsev. *SiC materials and devices*, volume 1. World Scientific (2006). ISBN 981-256-835-2.

[21] P. A. Ivanov and V. E. Chelnokov. Recent Developments in SiC Single-Crystal Electronics. *Semiconductor Science and Technology*, **7**, 7, 863 (1992). doi: 10.1088/0268-1242/7/7/001.

[22] A. Krüger. *Neue Kohlenstoffmaterialien*, volume 1. Teubner Verlag, Wiesbaden (2007). ISBN 978-3-519-00510-0.

[23] R. Weast, M. Astle and W. Beyer, editors. *Handbook of Chemistry and Physics*. CRC Press, Boca Raton, Florida, 65 edition (1985). ISBN 0-8493-0465-2.

[24] L. A. d. S. Balona and J. H. N. Loubser. ESR in irradiated silicon carbide. *Journal of Physics C: Solid State Physics*, **3**, 11, 2344 (1970). doi: 10.1088/0022-3719/3/11/015.

[25] E. A. Burgemeister, W. von Muench and E. Pettenpaul. Thermal conductivity and electrical properties of 6H silicon carbide. *Journal of Applied Physics*, **50**, 9, 5790 (1979). doi: 10.1063/1.326720.

[26] H. J. Round. A Note on Carborundum. *Electrical World*, 879 (1907).

[27] N. Zheludev. The life and times of the LED - a 100-year history. *Nature Photonics*, **1**, 189 (2007). doi: 10.1038/nphoton.2007.34.

[28] K. Momma and F. Izumi. VESTA 3 for three-dimensional visualization of crystal, volumetric and morphology data. *J. Appl. Cryst.*, **44**, 1272 (2011). doi: 10.1107/S0021889811038970.

[29] P. Friedrichs, T. Kimoto, L. Ley and G. Pensl, editors. *Silicon Carbide*, volume 1 of *Growth, Defects, and Novel Applications*. Wiley, Weinheim (2010). ISBN 978-3-527-40953-2.

[30] J. A. Lely. US Patent 2854364: Sublimation Process for Manufacturing Silicon Carbide Crystals. United States Patent Office (1958).

[31] Y. M. Tairov and V. F. Tsvetkov. Investigation of growth processes of ingots of silicon carbide single crystals. *Journal of Crystal Growth*, **43**, 2, 209 (1978). doi: 10.1016/0022-0248(78)90169-0.

[32] H. Morkoç, S. Strite, G. B. Gao, M. E. Lin, B. Sverdlov and M. Burns. Large-band-gap SiC, III-V nitride, and II-VI ZnSe-based semiconductor device technologies. *Journal of Applied Physics*, **76**, 3, 1363 (1994). doi: 10.1063/1.358463.

[33] D. Chen, M. E. Sixta, X. F. Zhang, L. C. De Jonghe and R. O. Ritchie. Role of the grain-boundary phase on the elevated-temperature strength, toughness, fatigue and creep resistance of silicon carbide sintered with Al, B and C. *Acta Materialia*, **48**, 18, 4599 (2000). doi: 10.1016/S1359-6454(00)00246-9.

[34] H. Fujiwara, T. Kimoto, T. Tojo and H. Matsunami. Characterization of in-grown stacking faults in 4H–SiC (0001) epitaxial layers and its impacts on high-voltage Schottky barrier diodes. *Applied Physics Letters*, **87**, 5, 051912 (2005). doi: 10.1063/1.1997277.

[35] S. G. Sridhara, F. H. C. Carlsson, J. Bergman and E. Janzén. Luminescence from stacking faults in 4H SiC. *Applied Physics Letters*, **79**, 24, 3944 (2001). doi: 10.1063/1.1425084.

[36] K. Koumoto, S. Takeda, C. H. Pai, T. Sato and H. Yanagida. High-Resolution Electron Microscopy Observations of Stacking Faults in beta-SiC. *Journal of the American Ceramic Society*, **72**, 10, 1985 (1989). doi: 10.1111/j.1151-2916.1989.tb06014.x.

[37] J. Bergman, L. Storasta, F. H. C. Carlsson, S. Sridhara, B. Magnusson and E. Janzén. Defects in 4H silicon carbide. *Physica B: Condensed Matter*, **308-310**, 675 (2001). doi: 10.1016/S0921-4526(01)00790-6.

[38] J. L. O'Brien, A. Furusawa and J. Vučković. Photonic quantum technologies. *Nature Photonics*, **3**, 12, 687 (2009). doi: 10.1038/nphoton.2009.229.

[39] J. O. Orwa, A. D. Greentree, I. Aharonovich, A. D. C. Alves, J. Van Donkelaar, A. Stacey and S. Prawer. Fabrication of single optical centres in diamond - a review. *Journal of Luminescence*, **130**, 9, 1646 (2010). doi: 10.1016/j.jlumin.2009.12.028.

[40] I. Aharonovich, S. Castelletto, D. A. Simpson, C.-H. Su, A. D. Greentree and S. Prawer. Diamond-based single-photon emitters. *Reports on Progress in Physics*, **74**, 7, 076501 (2011). doi: 10.1088/0034-4885/74/7/076501.

[41] A. Lohrmann, S. Pezzagna, I. Dobrinets, P. Spinicelli, V. Jacques, J. F. Roch, J. Meijer and A. M. Zaitsev. Diamond based light-emitting diode for visible single-photon emission at room temperature. *Applied Physics Letters*, **99**, 25, (2011). doi: 10.1063/1.3670332.

[42] E. Neu, D. Steinmetz, J. Riedrich-Möller, S. Gsell, M. Fischer, M. Schreck and C. Becher. Single photon emission from silicon-vacancy colour centres in chemical vapour deposition nano-diamonds on iridium. *New Journal of Physics*, **13**, 2, 025012 (2011). doi: 10.1088/1367-2630/13/2/025012.

[43] S. Castelletto, B. C. Johnson, V. Ivády, N. Stavrias, T. Umeda, A. Gali and T. Ohshima. A silicon carbide room-temperature single-photon source. *Nature Materials*, **12**, 11, 1 (2013). doi: 10.1038/namt3806.

[44] A. Krueger. Beyond the shine: recent progress in applications of nanodiamond. *Journal of Materials Chemistry*, **21**, 34, 12571 (2011). doi: 10.1039/c1jm11674f.

[45] I. I. Vlasov. Molecular-sized fluorescent nanodiamonds. *Nature Nanotechnology*, **9**, 1, 54 (2013). doi: 10.1038/nnano.2013.255.

[46] S. Castelletto, B. C. Johnson, C. Zachreson, D. Beke, I. Balogh, T. Ohshima, I. Aharonovich and A. Gali. Room Temperature Quantum Emission from Cubic Silicon Carbide Nanoparticles. *ACS Nano*, **8**, 8, 7938 (2014). doi: 10.1021/nn502719y.

[47] A. Muzha, F. Fuchs, N. V. Tarakina, D. Simin, M. Trupke, V. A. Soltamov, E. N. Mokhov, P. G. Baranov, V. Dyakonov, A. Krueger and G. V. Astakhov. Room-temperature near-infrared silicon carbide nanocrystalline emitters based on optically aligned spin defects. *Applied Physics Letters*, **105**, 24, 243112 (2014). doi: 10.1063/1.4904807.

[48] G. Balasubramanian, I. Y. Chan, R. Kolesov, M. Al-Hmoud, J. Tisler, C. Shin, C. Kim, A. Wojcik, P. R. Hemmer, A. Krueger, T. Hanke, A. Leitenstorfer, R. Bratschitsch, F. Jelezko and J. Wrachtrup. Nanoscale imaging magnetometry with diamond spins under ambient conditions. *Nature*, **455**, 7213, 648 (2008). doi: 10.1038/nature07278.

[49] V. M. Acosta, E. Bauch, M. P. Ledbetter, C. Santori, K.-M. Fu, P. E. Barclay, R. G. Beausoleil, H. Linget, J. F. Roch, F. Treussart, C. S, G. W and D. Budker. Diamonds with a high density of nitrogen-vacancy centers for magnetometry applications. *Physical Review B*, **80**, 11, 15 (2009). doi: 10.1103/PhysRevB.80.115202.

[50] K. Fang, V. M. Acosta, C. Santori, Z. Huang, K. M. Itoh, H. Watanabe, S. Shikata and R. G. Beausoleil. High-sensitivity magnetometry based on quantum beats in diamond nitrogen-vacancy centers. *Physical Review Letters*, **110**, 13, 130802 (2013). doi: 10.1103/PhysRevLett.110.130802.

[51] H. Kraus, V. A. Soltamov, F. Fuchs, D. Simin, A. Sperlich, P. G. Baranov, G. V. Astakhov and V. Dyakonov. Magnetic field and temperature sensing with atomic-scale spin defects in silicon carbide. *Scientific Reports*, **4** (2014). doi: 10.1038/srep05303.

[52] D. Simin, F. Fuchs, H. Kraus, A. Sperlich, P. G. Baranov, G. V. Astakhov and V. Dyakonov. High-Precision Angle-Resolved Magnetometry with Uniaxial Quantum Centers in Silicon Carbide. *Physical Review Applied*, **4**, 1, 014009 (2015). doi: 10.1103/PhysRevApplied.4.014009.

[53] J. R. Weber, W. F. Koehl, J. B. Varley, A. Janotti, B. B. Buckley, C. G. Van de Walle and D. D. Awschalom. Quantum computing with defects. *Proceedings of the National Academy of Sciences*, **107**, 19, 8513 (2010). doi: 10.1073/pnas.1003052107.

[54] A. Morello. Single spins in silicon carbide. *Nature Materials*, 1–2 (2014). doi: 10.1038/nmat4171.

[55] J. R. Petta. Coherent Manipulation of Coupled Electron Spins in Semiconductor Quantum Dots. *Science*, **309**, 5744, 2180 (2005). doi: 10.1126/science.1116955.

[56] S. Ritter, C. Nölleke, C. Hahn, A. Reiserer, A. Neuzner, M. Uphoff, M. Mücke, E. Figueroa, J. Bochmann and G. Rempe. An elementary quantum network of single atoms in optical cavities. *Nature*, **484**, 7393, 195 (2012). doi: 10.1038/nature11023.

[57] T. D. Ladd, F. Jelezko, R. Laflamme, Y. Nakamura, C. Monroe and J. L. O'Brien. Quantum computers. *Nature*, **464**, 7285, 45 (2010). doi: 10.1038/nature08812.

[58] A. M. Tyryshkin, S. Tojo, J. J. L. Morton, H. Riemann, N. V. Abrosimov, P. Becker, H.-J. Pohl, T. Schenkel, M. L. W. Thewalt, K. M. Itoh and S. A. Lyon. Electron spin coherence exceeding seconds in high-purity silicon. *Nature Materials*, **11**, 2, 143 (2011). doi: 10.1038/nmat3182.

[59] A. Gruber, A. Dräbenstedt, C. Tietz, L. Fleury, J. Wrachtrup and C. von Borczyskowski. Scanning Confocal Optical Microscopy and Magnetic Resonance on Single Defect Centers. *Science*, **276**, 5321, 2012 (1997). doi: 10.1126/science.276.5321.2012.

[60] F. Jelezko, T. Gaebel, I. Popa, A. Gruber and J. Wrachtrup. Observation of Coherent Oscillations in a Single Electron Spin. *Physical Review Letters*, **92**, 7, 076401 (2004). doi: 10.1103/PhysRevLett.92.076401.

[61] L. Childress, M. V. Gurudev Dutt, J. M. Taylor, A. S. Zibrov, F. Jelezko, J. Wrachtrup, P. R. Hemmer and M. D. Lukin. Coherent dynamics of coupled electron and nuclear spin qubits in diamond. *Science*, **314**, 5797, 281 (2006). doi: 10.1126/science.1131871.

[62] T. Gaebel. Room-temperature coherent coupling of single spins in diamond. *Nature Physics*, **2**, 6, 365 (2006). doi: 10.1038/nphys330.

[63] M. V. G. Dutt, L. Childress, L. Jiang, E. Togan, J. Maze, F. Jelezko, A. S. Zibrov, P. R. Hemmer and M. D. Lukin. Quantum Register Based on Individual Electronic and Nuclear Spin Qubits in Diamond. *Science*, **316**, 5829, 1312 (2007). doi: 10.1126/science.1139831.

[64] W. Pfaff, B. J. Hensen, H. Bernien, S. B. van Dam and M. S. Blok. Unconditional quantum teleportation between distant solid-state quantum bits. *Science* (2014).

[65] G. Waldherr, Y. Wang, S. Zaiser, M. Jamali, T. Schulte-Herbrüggen, H. Abe, T. Ohshima, J. Isoya, J. F. Du, P. Neumann and J. Wrachtrup. Quantum error correction in a solid-state hybrid spin register. *Nature*, **506**, 7487, 204 (2014). doi: 10.1038/nature12919.

[66] D. DiVincenzo. Quantum bits: Better than excellent. *Nature Materials*, **9**, 6, 468 (2010). doi: 10.1038/nmat2774.

[67] A. Dzurak. Quantum computing: Diamond and silicon converge. *Nature*, **479**, 7371, 47 (2011). doi: 10.1038/479047a.

[68] A. G. Smart. Silicon carbide defects hold promise for device-friendly qubits. *Physics Today*, **65**, 1, 10 (2012). doi: 10.1063/PT.3.1410.

[69] I. Aharonovich and M. Toth. Optical materials: Silicon carbide goes quantum. *Nature Physics*, **10**, 2, 93 (2014). doi: 10.1038/nphys2858.

[70] W. F. Koehl, B. B. Buckley, F. J. Heremans, G. Calusine and D. D. Awschalom. Room temperature coherent control of defect spin qubits in silicon carbide. *Nature*, **479**, 7371, 84 (2011). doi: 10.1038/nature10562.

[71] P. Baranov, A. Bundakova, A. Soltamova, S. Orlinskii, I. Borovykh, R. Zondervan, R. Verberk and J. Schmidt. Silicon vacancy in SiC as a promising quantum system for single-defect and single-photon spectroscopy. *Physical Review B*, **83**, 12, 125203 (2011). doi: 10.1103/PhysRevB.83.125203.

[72] D. Riedel, F. Fuchs, H. Kraus, S. Väth, A. Sperlich, V. Dyakonov, A. A. Soltamova, P. G. Baranov, V. A. Ilyin and G. V. Astakhov. Resonant addressing and manipulation of silicon vacancy qubits in silicon carbide. *Physical Review Letters*, **109**, 22, 226402 (2012). doi: 10.1103/PhysRevLett.109.226402.

[73] P. G. Baranov, V. A. Soltamov, A. A. Soltamova, G. V. Astakhov and V. D. Dyakonov. Point Defects in SiC as a Promising Basis for Single-Defect, Single-Photon Spectroscopy with Room Temperature Controllable Quantum States. *Materials Science Forum*, **740-742**, 425 (2013). doi: 10.4028/www.scientific.net/MSF.740-742.425.

[74] S. Castelletto, B. C. Johnson and A. Boretti. Quantum Effects in Silicon Carbide Hold Promise for Novel Integrated Devices and Sensors. *Advanced Optical Materials*, **1**, 9, 609 (2013). doi: 10.1002/adom.201300246.

[75] J. Steeds, G. Evans, L. Danks and S. Furkert. Transmission electron microscope radiation damage of 4H and 6H SiC studied by photoluminescence spectroscopy. *Diamond & Related Materials*, **11**, 1923 (2002). doi: 10.1016/S0925-9635(02)00212-1.

[76] P. Sharma, S. Brown, G. Walter, S. Santra and B. Moudgil. Nanoparticles for bioimaging. *Advances in Colloid and Interface Science*, **123-126**, 471 (2006). doi: 10.1016/j.cis.2006.05.026.

[77] A. M. Smith, M. C. Mancini and S. Nie. Second window for in vivo imaging. *Nature Nanotechnology*, **4**, 11, 710 (2009). doi: 10.1038/nnano.2009.326.

[78] C. Bradac, T. Gaebel, N. Naidoo, M. J. Sellars, J. Twamley, L. J. Brown, A. S. Barnard, T. Plakhotnik, A. V. Zvyagin and J. R. Rabeau. Observation and control of blinking nitrogen-vacancy centres in discrete nanodiamonds. *Nature Nanotechnology*, **5**, 5, 345 (2010). doi: 10.1038/nnano.2010.56.

[79] M. W. Doherty, F. Dolde, H. Fedder, F. Jelezko, J. Wrachtrup, N. B. Manson and L. C. L. Hollenberg. Theory of the ground-state spin of the NV(-) center in diamond. *Physical Review B*, **85**, 20, 205203 (2012). doi: 10.1103/PhysRevB.85.205203.

[80] A. O. Levchenko, V. V. Vasil'ev, S. A. Zibrov, A. S. Zibrov, A. V. Sivak and I. V. Fedotov. Inhomogeneous broadening of optically detected magnetic resonance of the ensembles of nitrogen-vacancy centers in diamond by interstitial carbon atoms. *Applied Physics Letters*, **106**, 10, 102402 (2015). doi: 10.1063/1.4913428.

[81] H. Kraus, V. A. Soltamov, D. Riedel, S. Väth, F. Fuchs, A. Sperlich, P. G. Baranov, V. Dyakonov and G. V. Astakhov. Room-temperature quantum microwave emitters based on spin defects in silicon carbide. *Nature Physics*, **10**, 12, 1 (2013). doi: 10.1038/nphys2826.

[82] P. T. B. Shaffer, F. P. Larkins and A. M. Stoneham. Electronic structure of isolated single vacancy centres in silicon carbide. *Journal of Physics C: Solid State Physics*, **3**, 6 (1970). doi: 10.1088/0022-3719/3/6/025.

[83] V. S. Vainer and V. A. Il'in. Electron spin resonance of exchange-coupled vacancy pairs in hexagonal silicon carbide. *Sov. Phys. Solid State*, **23**, 1 (1981).

[84] H. Itoh, M. Yoshikawa, I. Nashiyama, S. Misawa, H. Okomura and S. Yoshida. Radiation Induced Defects in CVD-Grown 3C-SiC. *IEEE Transactions on Nuclear Science*, **37**, 6, 1732 (1990). doi: 10.1109/23.101184.

[85] H. Itoh, M. Yoshikawa, I. Nashiyama, H. Okumura, S. Misawa and S. Yoshida. Photoluminescence of radiation induced defects in 3C-SiC epitaxially grown on Si. *Journal of Applied Physics*, **77**, 2, 837 (1995). doi: 10.1063/1.359008.

[86] E. Janzén, A. Gali, P. Carlsson, A. Gällström, B. Magnusson and N. T. Son. The silicon vacancy in SiC. *Physica B: Condensed Matter*, **404**, 22, 4354 (2009). doi: 10.1016/j.physb.2009.09.023.

[87] H. Kraus. Optically Detected Magnetic Resonance on Organic and Inorganic Carbon-Based Semiconductors. Ph.D. thesis, Julius-Maximilians Universität Würzburg (2014).

[88] M. Wagner, B. Magnusson, W. Chen, E. Janzén, E. Sörman, C. Hallin and J. L. Lindstrom. Electronic structure of the neutral silicon vacancy in 4H and 6H SiC. *Physical Review B*, **62**, 24, 16555 (2000). doi: 10.1103/PhysRevB.62.16555.

[89] S. Orlinski, J. Schmidt, E. Mokhov and P. Baranov. Silicon and carbon vacancies in neutron-irradiated SiC: A high-field electron paramagnetic resonance study. *Physical Review B*, **67**, 12, 125207 (2003). doi: 10.1103/PhysRevB.67.125207.

[90] L. Torpo, R. M. Nieminen, K. E. Laasonen and S. Poykko. Silicon vacancy in SiC: A high-spin state defect. *Applied Physics Letters*, **74**, 2, 221 (1999). doi: 10.1063/1.123299.

[91] T. Wimbauer, B. Meyer, A. Hofstaetter, A. Scharmann and H. Overhof. Negatively charged Si vacancy in 4H SiC: A comparison between theory and experiment. *Physical Review B*, **56**, 12, 7384 (1997). doi: 10.1103/PhysRevB.56.7384.

[92] E. Sörman, N. Son, W. Chen, O. Kordina, C. Hallin and E. Janzén. Silicon vacancy related defect in 4H and 6H SiC. *Physical Review B*, **61**, 4, 2613 (2000). doi: 10.1103/PhysRevB.61.2613.

[93] N. Mizuochi, S. Yamasaki, H. Takizawa, N. Morishita, T. Ohshima, H. Itoh, T. Umeda and J. Isoya. Spin multiplicity and charge state of a silicon vacancy (TV2a) in 4H-SiC determined by pulsed ENDOR. *Physical Review B*, **72**, 23, 235208 (2005). doi: 10.1103/PhysRevB.72.235208.

[94] J. A. Weil and J. R. Bolton. Electron Paramagnetic Resonance. John Wiley & Sons, Hoboken, New Jersey (2007). ISBN 978-0471-75496-1.

[95] V. Soltamov, A. Soltamova, P. Baranov and I. Proskuryakov. Room Temperature Coherent Spin Alignment of Silicon Vacancies in 4H- and 6H-SiC. *Physical Review Letters*, **108**, 22, 226402 (2012). doi: 10.1103/PhysRevLett.108.226402.

[96] A. Zywietz, T. Lingner, J. Furthmuller, S. Greulich-Weber, F. Bechstedt, J. M. Spaeth, U. Gerstmann, E. Rauls, Z. Hajnal, T. Frauenheim and H. Overhof. Vacancies in SiC: Influence of Jahn-Teller distortions, spin effects, and crystal structure. *Physical Review B*, **59**, 23, 15166 (1999). doi: 10.1103/PhysRevB.59.15166.

[97] C. Kurtsiefer, S. Mayer, P. Zarda and H. Weinfurter. Stable Solid-State Source of Single Photons. *Physical Review Letters*, **85**, 2, 290 (2000). doi: 10.1103/PhysRevLett.85.290.

[98] F. Jelezko and J. Wrachtrup. Single defect centres in diamond: A review. *physica status solidi (a)*, **203**, 13, 3207 (2006). doi: 10.1002/pssa.200671403.

[99] M. Fox. *Quantum Optics: An Introduction: An Introduction*, volume 15. Oxford university press (2006). ISBN 978-0-198-56673-5.

[100] B. Lounis and M. Orrit. Single-photon sources. *Reports on Progress in Physics*, **68**, 5, 1129 (2005). doi: 10.1088/0034-4885/68/5/R04.

[101] E. Smith and G. Dent. *Modern Raman Spectroscopy*. A Practical Approach. Wiley (2005). ISBN 0-471-49668-5.

[102] W. Becker. *Advanced Time-Correlated Single Photon Counting Techniques*. Springer (2005). ISBN 978-3-540-26047-9.

[103] T. Basché, W. E. Moerner, M. Orrit and H. Talon. Photon antibunching in the fluorescence of a single dye molecule trapped in a solid. *Physical Review Letters*, **69**, 10, 1516 (1992). doi: 10.1103/PhysRevLett.69.1516.

[104] A. L. Falk, B. B. Buckley, G. Calusine, W. F. Koehl, V. V. Dobrovitski, A. Politi, C. A. Zorman, P. X. L. Feng and D. D. Awschalom. Polytype control of spin qubits in silicon carbide. *Nature Communications*, **4**, 1819 (2013). doi: 10.1038/ncomms2854.

[105] H. W. Weber, H. Böck, E. Unfried and L. R. Greenwood. Neutron dosimetry and damage calculations for the TRIGA MARK-II reactor in Vienna. *Journal of Nuclear Materials*, **137**, 3, 236 (1985). doi: 10.1016/0022-3115(86)90225-4.

[106] H. L. Heinisch, L. R. Greenwood, W. J. Weber and R. E. Williford. Displacement damage in silicon carbide irradiated in fission reactors. *Journal of Nuclear Materials*, **327**, 2-3, 175 (2004). doi: 10.1016/j.jnucmat.2004.02.012.

[107] H. Heissenstein, C. Peppermueller and R. Helbig. Characterization of phosphorus doped n-type 6H-silicon carbide epitaxial layers produced by nuclear transmutation doping. *Journal of Applied Physics*, **83**, 12, 7542 (1998). doi: 10.1063/1.367518.

[108] H. Itoh, N. Hayakawa, I. Nashiyama and E. Sakuma. Electron spin resonance in electron-irradiated 3C-SiC. *Journal of Applied Physics*, **66**, 9, 4529 (1989). doi: 10.1063/1.343920.

[109] J. W. Steeds. Orientation dependence of near-threshold damage production by electron irradiation of 4H SiC and diamond and outward migration of defects . *Nuclear Inst. and Methods in Physics Research, B*, **269**, 14, 1702 (2011). doi: 10.1016/j.nimb.2010.12.029.

[110] H. von Bardeleben, J. Cantin, L. Henry and M. Barthe. Vacancy defects in p-type 6H-SiC created by low-energy electron irradiation. *Physical Review B*, **62**, 16, 10841 (2000). doi: 10.1103/PhysRevB.62.10841.

[111] L. Patrick and W. J. Choyke. Photoluminescence of Radiation Defects in Ion-Implanted 6H SiC. *Physical Review B*, **5**, 1 (1972). doi: 10.1103/PhysRevB.5.3253.

[112] T. C. Hain, F. Fuchs, V. A. Soltamov, P. G. Baranov, G. V. Astakhov, T. Hertel and V. Dyakonov. Excitation and recombination dynamics of vacancy-related spin centers in silicon carbide. *Journal of Applied Physics*, **115**, 13, 133508 (2014). doi: 10.1063/1.4870456.

[113] A. T. Collins, M. F. Thomaz and M. I. B. Jorge. Luminescence decay time of the 1.945 eV center in Type Ib diamond. *Journal of Physics C: Solid State Physics*, **16**, 11, 2177 (1983). doi: 10.1088/0022-3719/16/11/020.

[114] F. Fuchs, B. Stender, M. Trupke, D. Simin, J. Pflaum, V. Dyakonov and G. V. Astakhov. Engineering near-infrared single-photon emitters with optically active spins in ultrapuresilicon carbide. *Nature Communications*, **6**, 1 (2015). doi: 10.1038/ncomms8578.

[115] D. W. Feldman, J. H. Parker, Jr, W. J. Choyke and L. Patrick. Phonon Dispersion Curves by Raman Scattering in SiC, Polytypes 3C, 4H, 6H, 15R, and 21R. *Physical Review*, **173**, 3, 787 (1968). doi: 10.1103/PhysRev.173.787.

[116] M. Bauer, A. M. Gigler, A. J. Huber, R. Hillenbrand and R. W. Stark. Temperature-depending Raman line-shift of silicon carbide. *Journal of Raman Spectroscopy*, **40**, 12, 1867 (2009). doi: 10.1002/jrs.2334.

[117] R. Brouri, A. Beveratos, J.-P. Poizat and P. Grangier. Photon antibunching in the fluorescence of individual color centers in diamond. *Optics Letters*, **25**, 17, 1294 (2000). doi: 10.1364/OL.25.001294.

[118] M. Pinheiro, T. Lingner, F. Caudepon, S. Greulich-Weber and J. Spaeth. Annealing study on radiation-induced defects in 6H-SiC. In *Materials Science Forum*, 517–520. Silicon Carbide and Related Materials (2004). doi: 10.4028/www.scientific.net/MSF.457-460.517.

[119] M. Bockstedte, A. Mattausch and O. Pankratov. Ab initio study of the annealing of vacancies and interstitials in cubic SiC: Vacancy-interstitial recombination and aggregation of carbon interstitials. *Physical Review B*, **69**, 23, 235202 (2004). doi: 10.1103/PhysRevB.69.235202.

[120] V. Nagesh, J. W. Farmer, R. F. Davis and H. S. Kong. Defects in neutron irradiated SiC. *Applied Physics Letters*, **50**, 17, 1138 (1987). doi: 10.1063/1.97941.

[121] F. Fuchs, V. A. Soltamov, S. Väth, P. G. Baranov, E. N. Mokhov, G. V. Astakhov and V. Dyakonov. Silicon carbide light-emitting diode as a prospective room temperature source for single photons. *Scientific Reports*, **3** (2013). doi: 10.1038/srep01637.

[122] L. Patrick and W. J. Choyke. Localized vibrational modes of a persistent defect in ion-implanted SiC. *Journal of Physics and Chemistry of Solids*, **34**, 3, 565 (1973). doi: 10.1016/0022-3697(73)90051-6.

[123] M. Pinheiro, E. Rauls, U. Gerstmann, S. Greulich-Weber, H. Overhof and J. M. Spaeth. Silicon vacancy annealing and DI luminescence in 6H-SiC. *Physical Review B*, **70**, 24, 245204 (2004). doi: 10.1103/PhysRevB.70.245204.

[124] T. Egilsson, I. Ivanov, A. Henry and E. Janzén. Pseudo-Donors in SiC. *Materials Science Forum*, **338-342**, 647 (2000). doi: 10.4028/www.scientific.net/MSF.338-342.647.

[125] L. Storasta, F. H. C. Carlsson, S. G. Sridhara, J. Bergman, A. Henry, T. Egilsson, A. Hallén and E. Janzén. Pseudodonor nature of the D1 defect in 4H-SiC. *Applied Physics Letters*, **78**, 1, 46 (2001). doi: 10.1063/1.1334907.

[126] C. Böckler, S. Reitzenstein, C. Kistner, R. Debusmann, A. Löffler, T. Kida, S. Höfling, A. Forchel, L. Grenouillet, J. Claudon and J. M. Gérard. Electrically driven high-Q quantum dot-micropillar cavities. *Applied Physics Letters*, **92**, 9, 091107 (2008). doi: 10.1063/1.2890166.

[127] A. Boretti, L. Rosa, A. Mackie and S. Castelletto. Electrically Driven Quantum Light Sources. *Advanced Optical Materials*, 1–22 (2015). doi: 10.1002/adom.201500022.

[128] M. Nothaft, S. Hoehla, F. Jelezko, N. Fruehauf, J. Pflaum and J. Wrachtrup. Electrically driven photon antibunching from a single molecule at room temperature. *Nature Communications*, **3**, 628 (2012). doi: 10.1038/ncomms1637.

[129] Z. Yuan. Electrically Driven Single-Photon Source. *Science*, **295**, 5552, 102 (2001). doi: 10.1126/science.1066790.

[130] T. Heindel, C. Schneider, M. Lermer, S. H. Kwon, T. Braun, S. Reitzenstein, S. Höfling, M. Kamp and A. Forchel. Electrically driven quantum dot-micropillar single photon source with 34% overall efficiency. *Applied Physics Letters*, **96**, 1, 011107 (2010). doi: 10.1063/1.3284514.

[131] A. Lohrmann, N. Iwamoto, Z. Bodrog, S. Castelletto, T. Ohshima, T. J. Karle, A. Gali, S. Prawer, J. C. McCallum and B. C. Johnson. Single-photon emitting diode in silicon carbide. *Nature Communications*, **6**, 1 (2015). doi: 10.1038/ncomms8783.

[132] N. Mohan, C.-S. Chen, H.-H. Hsieh, Y.-C. Wu and H.-C. Chang. In Vivo Imaging and Toxicity Assessments of Fluorescent Nanodiamonds in Caenorhabditis elegans. *Nano Letters*, **10**, 9, 3692 (2010). doi: 10.1021/nl1021909.

[133] J. Botsoa, V. Lysenko, A. Géloën, O. Marty, J. M. Bluet and G. Guillot. Application of 3C-SiC quantum dots for living cell imaging. *Applied Physics Letters*, **92**, 17, 173902 (2008). doi: 10.1063/1.2919731.

[134] J. Fan, H. Li, J. Jiang, L. K. Y. So, Y. W. Lam and P. K. Chu. 3C-SiC Nanocrystals as Fluorescent Biological Labels. *Small*, **4**, 8, 1058 (2008). doi: 10.1002/smll.200800080.

[135] U. Resch-Genger, M. Grabolle, S. Cavaliere-Jaricot, R. Nitschke and T. Nann. Quantum dots versus organic dyes as fluorescent labels. *Nature Methods*, **5**, 9, 763 (2008). doi: 10.1038/nmeth.1248.

[136] A. M. Derfus, W. C. W. Chan and S. N. Bhatia. Probing the Cytotoxicity of Semiconductor Quantum Dots. *Nano Letters*, **4**, 1, 11 (2004). doi: 10.1021/nl0347334.

[137] B. Mognetti, A. Barberis, S. Marino, F. Di Carlo, V. Lysenko, O. Marty and A. Géloën. Preferential Killing of Cancer Cells Using Silicon Carbide Quantum Dots. *Journal of Nanoscience and Nanotechnology*, **10**, 12, 7971 (2010). doi: 10.1166/jnn.2010.3049.

[138] S. E. Saddow. *Silicon Carbide Biotechnology*. Elsevier, 1 edition (2012). ISBN 978-0-12-385906-8.

[139] J. Botsoa, J. Bluet, V. Lysenko, L. Sfaxi, Y. Zakharko, O. Marty and G. Guillot. Luminescence mechanisms in 6H-SiC nanocrystals. *Physical Review B*, **80**, 15, 155317 (2009). doi: 10.1103/PhysRevB.80.155317.

[140] B. Somogyi and A. Gali. Computational design of in vivobiomarkers. *J. Phys.: Condens. Matter*, **26**, 14, 143202 (2014). doi: 10.1088/0953-8984/26/14/143202.

[141] S. Heyer, W. Janssen, S. Turner, Y.-G. Lu, W. S. Yeap, J. Verbeeck, K. Haenen and A. Krueger. Toward Deep Blue Nano Hope Diamonds: Heavily Boron-Doped Diamond Nanoparticles. *ACS Nano*, **8**, 6, 5757 (2014). doi: 10.1021/nn500573x.

[142] G. C. Capitani, S. Di Pierro and G. Tempesta. The 6H-SiC structure model: Further refinement from SCXRD data from a terrestrial moissanite. *American Mineralogist*, **92**, 2-3, 403 (2007). doi: 10.2138/am.2007.2346.

[143] A. Perez-Rodriguez, Y. Pacaud, L. Calvo-Barrio, C. Serre, W. Skorupa and J. Morante. Analysis of ion beam induced damage and amorphization of 6H-SiC by Raman scattering. *Journal of Electronic Materials*, **25**, 3, 541 (1996). doi: 10.1007/BF02666633.

[144] N. Mizuochi, S. Yamasaki, H. Takizawa, N. Morishita, T. Ohshima, H. Itoh and J. Isoya. Continuous-wave and pulsed EPR study of the negatively charged silicon vacancy with S=3/2 and C3v symmetry in n-type 4H-SiC. *Physical Review B*, **66**, 23, 235202 (2002). doi: 10.1103/PhysRevB.66.235202.

[145] B. Somogyi, V. Zólyomi and A. Gali. Near-infrared luminescent cubic silicon carbide nanocrystals for in vivo biomarker applications: an ab initio study. *Nanoscale*, **4**, 24, 7720 (2012). doi: 10.1039/c2nr32442c.

[146] I. Aharonovich, S. Castelletto, D. A. Simpson, A. D. Greentree and S. Prawer. Photophysics of chromium-related diamond single-photon emitters. *Physical Review A*, **81**, 4, 043813 (2010). doi: 10.1103/PhysRevA.81.043813.

A. Appendix

A.1. Samples used in this thesis

The samples of each respective chapter are catalogued in table A.1 by polytype, growth, doping type and level, irradiation, annealing and their specialty. Further information, like the exact (layer) structure or the milling process is given in each chapter.

Chapter	4.2	5	6	7
Polytype	4H		6H	6H
Growth	epitaxy, wafer from CREE		epitaxy	sublimation (Argon, 2500-2600°C)
Impurity/ Doping [cm^{-3}]	N: $5 \cdot 10^{14}$		p: Al: $1 \cdot 10^{20}$ n: N: $3 \cdot 10^{18}$ and Ga: $2 \cdot 10^{18}$	N: $< 10^{16}$
Irradiation with fluence	electrons (0.9 MeV) 2.2-$7.5 \cdot 10^{18}$ e/cm^2	neutrons (0.18-2.5 MeV) $1 \cdot 10^{9}$-$5 \cdot 10^{17}$ n/cm^2	electrons (0.9 MeV) 10^{18} e/cm^2	neutrons (0.18-2.5 MeV) 10^{17} n/cm^2
Annealing		partly	Ar, 1700°C for 1min	
Speciality	fluence variation		pn-junction, contacts: Al $(0.4mm)^2$	Milling, Nanocrystals

Table A.1.: Overview of the SiC samples used in this thesis.

A.2. Correlation function

The start-stop TCSPC in chapter 5.2 are measuring time-delay histograms c(t), i.e. the distribution of consecutive photon pairs. According to Basché et al. [103], this is indistinguishable from the full correlation function, if the count rates are low and the delay times are short enough.

In order to yield the second order correlation function $g^{(2)}(\tau)$ from the histogram c(t), the data have to be normalized and corrected for systematical errors [117]. Systematical errors are a time offset, counts due to background fluorescence and dark counts and due to the finite time resolution due to the detectors' dead times. The latter is in our case not relevant, as the count rates are so low, that the dead time of the APDs is not a limiting factor.

Time correction

To have access to negative delay times $\tau < 0$, a time retarder is built into one of the arms of the HBT setup. This results in a systematic time offset t_{off}, which has to be corrected by a linear time shift: $c(\tau) = c(t - t_{\text{off}})$.

Normalization

Both the normalization and the subsequent background correction were performed according to Brouri and coworkers in [117]. A Poissonian light source has a coincidence rate in a time bin of width Δb of $\dot{N}_1 \dot{N}_2 \Delta b$, where $\dot{N}_{1,2}$ are the count rates on $\text{APD}_{1,2}$. The time-delay histograms c(t) is thus normalized to that of a Poissonian source according to the formula

$$C_{norm}(\tau) = \frac{c(\tau)}{\dot{N}_1 \dot{N}_2 \Delta b T} \tag{A.1}$$

with the measurement aquisition time T.

Background correction

The background correction takes into account systematical background counts, that are uncorrelated with the photons emitted from the defect. This has to be verified with an independent measurement, where also the signal count rate S and the background count rate B are determined. With the ratio $\rho = \frac{S}{S+B}$, the second order correlation function is the obtained via

$$g^{(2)}(\tau) = \frac{C_{norm}(\tau) - (1 - \rho^2)}{\rho^2}. \tag{A.2}$$

A.3. Calculation of transition rates

In table 5.1 of chapter 5.2, the transition rates and absorption cross sections for a single silicon vacancy are shown. The procedures to derive them from the power dependencies of the fit parameters a, τ_1 and τ_2 in the second order correlation function $g^{(2)}(\tau) = 1 - (1 + a(W))e^{-\frac{|\tau|}{\tau_1(W)}} + a(W) \cdot e^{-\frac{|\tau|}{\tau_2(W)}}$ are described in the following. The rate calculations were carried out by G. Astakhov and B. Stender [114].

3-level model

As a first attempt, a 3-level model with ground state GS, excited state ES and metastable state MS was assumed (compare figure 5.9 in chapter 5.2). The following calculations were adapted from that of color centers in diamond [97, 42, 146]. The radiative relaxation k_{21}, as well as k_{23} and k_{31} are assumed to be constant with $k_{21} + k_{23} > k_{31}$. Furthermore, k_{12} is power dependent according to $k_{12}(W) = \sigma W$ with the absorption cross section σ.

The fit parameters of $g^{(2)}(\tau)$ are:

$$a = \frac{1 - k_{31}\tau_2}{k_{31}(\tau_2 - \tau_1)} \tag{A.3}$$

$$\tau_{1,2} = \frac{2}{A \pm \sqrt{A^2 - 4B}} \tag{A.4}$$

where A and B are defined as

$$A := k_{12} + k_{21} + k_{23} + k_{31}$$
$$B := k_{12}k_{23} + k_{12}k_{31} + k_{21}k_{31} + k_{23}k_{31}.$$

From the limits of very small and high excitation powers (W→0 and W→ ∞; denoted with superscripts ^{0} and $^\infty$), the transition rates can be calculated via the following connections:

$$k_{31} = \frac{1}{(a^\infty + 1)\tau_2^\infty} \tag{A.5}$$

$$k_{23} = a^\infty k_{31} \tag{A.6}$$

$$k_{21} = \frac{1}{\tau_1^0} - k_{23} \tag{A.7}$$

From the saturation curve I(W) (equation 5.1), yielding the saturation power density W_0, the absorption cross section σ can be extracted:

$$\sigma = \frac{E_{exc}}{W_0 T} \cdot \frac{k_{31}(k_{21}+k_{23})}{k_{23}+k_{31}} \tag{A.8}$$

with the excitation energy E_{exc} and the transmission coefficient at the SiC surface T=0.81.

This model describes reasonably well the bunching amplitude a(W) and the antibunching decay time τ_1(W). But the relatively long bunching decay time τ_2 at low excitation powers W < 100 kW·cm^{-2} is not well reproduced within this 3-level model. A possible explanation is that a deshelving process of the metastable state may occur under optical excitation, and thus the model is extended to a 4-level model.

4-level model

The 4-level model was used analogously to an approach applied to describe the photophysics of the SiV center in diamond [42]. It allows a possible excitation from MS to a higher lying state (power dependent deshelving process), with a relaxation back to the ES having a transfer rate k_{32} from the MS to ES. This can also be described with a power dependent rate k_{31}(W) under the assumption $k_{21}+k_{23} \gg k_{31} \forall$ W. We calculate the limits of k_{31}:

$$k_{31}^0 = \frac{1}{\tau_2^0} \tag{A.9}$$

$$k_{31}^\infty = \frac{1}{(a^\infty+1)\tau_2^\infty} \tag{A.10}$$

Equations A.6 and A.7 still hold, if k_{31} is replaced with k_{31}^∞.

The power dependence of k_{31} is modeled with a saturation law:

$$k_{31}(W) = \frac{(k_{31}^\infty - k_{31}^0)W}{W+W_s} + k_{31}^0 \tag{A.11}$$

With equation A.8, where k_{31} is replaced with k_{31}^0, the absorption cross section σ can be estimated. This estimated σ is used together with the calculated $k_{21}, k_{23}, k_{31}^0, k_{31}^\infty$ to fit the experimental data for a(W), τ_1(W) and τ_2(W) (compare formulae A.3 and A.4): First τ_2(W) is fitted with W_s as the only free parameter. Then τ_1(W), τ_2(W) and a(W) are fitted, allowing σ and a^∞ to vary. From the best fits (see [114]) we obtain W_s=75 kW·cm^{-2} and a^∞=7.5. The absorption cross section σ and the transition rates are summarized in table 5.1 of section 5.2.

A.4. Publications and conference contributions

Peer reviewed work

1. *F. Fuchs and B. Stender, M. Trupke, D. Simin, J. Pflaum, V. Dyakonov, and G. V. Astakhov.* Engineering near-infrared single-photon emitters with optically active spins in ultrapure silicon carbide. *Nat. Comm.* **6**, 1-7 (2015). 10.1038/ncomms8578

2. *F. Fuchs and A. Muzha, N. V. Tarakina, D. Simin, M. Trupke, V. A. Soltamov, E. N. Mokhov, P. G. Baranov, V. Dyakonov, A. Krueger, G. V. Astakhov.* Room-temperature near-infrared silicon carbide nanocrystalline emitters based on optically aligned spin defects. *Appl. Phys. Lett.* **105**, 243112 (2014). 10.1063/1.4904807

3. *F. Fuchs, V. A. Soltamov, S. Väth, P. G. Baranov, E. N. Mokhov, G. V. Astakhov, V. Dyakonov.* Silicon carbide light-emitting diode as a prospective room temperature source for single photons. *Sci. Rep.* **3**, 1637 (2013). 10.1038/srep01637

4. *D. Simin, F. Fuchs, H. Kraus, A. Sperlich, P. G. Baranov, G. V. Astakhov, V. Dyakonov.* High-precision angle-resolved magnetometry with uniaxial quantum centers in silicon carbide. *Phys. Rev. Applied* **4**, 014009 (2015). 10.1103/4.014009

5. *T. C. Hain, F. Fuchs, V. A. Soltamov, P. G. Baranov, G. V. Astakhov, T. Hertel, V. Dyakonov.* Excitation and recombination dynamics of vacancy-related spin centers in silicon carbide. *J. Appl. Phys.* **115**, 133508 (2014). 10.1063/1.4870456

6. *H. Kraus, V. A. Soltamov, F. Fuchs, D. Simin, A. Sperlich, P. G. Baranov, G. V. Astakhov, V. Dyakonov.* Magnetic field and temperature sensing with atomic-scale spin defects in silicon carbide. *Sci. Rep.* **4**, 5303 (2014). 10.1038/srep05303

7. *H. Kraus, V. A. Soltamov, D. Riedel, S. Väth, F. Fuchs, A. Sperlich, P. G. Baranov, V. Dyakonov, G. V. Astakhov.* Room-temperature quantum microwave emitters based on spin defects in silicon carbide. *Nat. Phys.* **10**, 157-162 (2014). 10.1038/nphys2826.

8. *D. Riedel, F. Fuchs, H. Kraus, S. Väth, A. Sperlich, V. Dyakonov, A. A. Soltamova, P. G. Baranov, V. A. Ilyin, G. V. Astakhov.* Resonant addressing and manipulation of silicon vacancy qubits in silicon carbide. *Phys. Rev. Lett.* **109**, 226402 (2012). 10.1103/PhysRevLett.109.226402

9. *S. Moser, L. Moreschini, H. Y. Yang, D. Innocenti, F. Fuchs, N. H. Hansen, Y. J. Chang, K. S. Kim, A. L. Walter, A. Bostwick, E. Rotenberg, F. Mila, and M. Grioni.* Angle-Resolved Photoemission Spectroscopy of Tetragonal CuO: Evidence for Intralayer Coupling Between Cupratelike Sublattices. *Phys. Rev. Lett.* **113**, 187001(2014). 10.1103/PhysRevLett.113.187001

10. *S. Issing, F. Fuchs, C. Ziereis, E. Batke, A. Pimenov, Y. V. Ivanov, A. A. Mukhin, and J. Geurts.* Lattice dynamics of $Eu_{1-x}Y_xMnO_3$ ($0 \leq x \leq 0.5$). *Eur. Phys. J. B* **73**, 353–360 (2010). 10.1140/epjb/e2010-00009-6

Oral Presentations and conference posters

1. DPG SKM spring meeting 2015 (Berlin, Germany). *F. Fuchs, A. Muzha, N. Tarakina, D. Simin, M. Trupke, P. Baranov, V. Dyakonov, A. Krueger, and G. Astakhov* SiC nano-crystalline NIR emitters based on optically excited and spin polarized defects.
2. DPG SKM spring meeting 2014 (Dresden, Germany). *F. Fuchs, M. Trupke, G. Astakhov, and V. Dyakonov.* Spin defect engineering in silicon carbide using neutron irradiation.
3. International Conference on Silicon Carbide and Related Materials (ICSCRM) 2013 (Miyazaki, Japan). *F. Fuchs, V. Soltamov, S. Väth, P. Baranov, E. Mokhov, G. Astakhov, V. Dyakonov.* Silicon carbide light-emitting diode as a prospective room temperature source for single photons.
4. DPG AMOP spring meeting 2013 (Hannover,Germany). *F. Fuchs, V. Soltamov, S. Väth, P. Baranov, E. Mokhov, G. Astakhov, V. Dyakonov.* Atomic defects in silicon carbide LEDs as a perspective single photon source.
5. DPG SKM spring meeting 2013 (Regensburg, Germany). *F. Fuchs, V. Soltamov, S. Väth, P. Baranov, E. Mokhov, G. Astakhov, V. Dyakonov.* Intrinsic defects in silicon carbide LEDs as a perspective single photon source
6. DPG Deutsche Physikerinnentagung 2012 (Freiburg, Germany). *F. Fuchs, V. Soltamov, S. Väth, P. Baranov, E. Mokhov, G. Astakhov, V. Dyakonov.* Intrinsic defects in silicon carbide LEDs as a perspective single photon source.
7. DPG SKM spring meeting 2012 (Berlin,Germany). *F. Fuchs, G. Astakhov, A. Soltamova , P. Baranov, and V. Dyakonov.* Spatially-resolved photoluminescence of silicon vacancy centers in 6H-SiC.

A.5. Danksagung

Zum Schluss dieser Arbeit möchte ich mich noch bei einigen Menschen bedanken, die mich während dieses Lebensabschnitts begleitet und unterstützt haben, und so erheblich zum Gelingen meiner Promotion beigetragen haben.

Zuallererst danke ich meinem Doktorvater Prof. **Vladimir Dyakonov**, der es mir ermöglichte, diese Arbeit an seinem Lehrstuhl anzufertigen. Danke für deine Unterstützung, auf die ich mich immer verlassen konnte, und dein Vertrauen in meine Person. Deine kritischen Fragen und hilfreiche Kommentare zu Vorträgen und Konferenzen haben mich immer ein Stück weiter gebracht. Daneben bin ich auch dem Gruppenleiter der SiC Gruppe, Dr. **Georgy Astakhov**, zu großem Dank verpflichtet bin. Nach der anfänglichen Gewöhnungsphase bin ich nun sehr froh, dich als fachlichen Betreuer zu haben. Ich habe viel von dir gelernt und ohne dich wäre die SiC Gruppe bestimmt nicht da, wo sie jetzt ist.

Danke auch an Prof. **Jean Geurts**, der mich 2009 in meiner Zulassungsarbeit, meinem Erstkontakt zu wirklicher Forschung, betreut hat und durch den ich meine Freude am wissenschaftlichen Arbeiten entdeckt habe. Ich freue mich besonders, dass du als Zweitgutachter meine Doktorarbeit beurteilst.

Allen derzeitigen und ehemaligen Kollegen der EP 6 möchte ich danken für den guten Zusammenhalt und die angenehme Atmosphäre, die das Arbeiten extrem erleichtert hat. Besonderer Dank gilt hier **Dmitrij**, meinem immer aufmüpfigen, ehemaligen Masteranden und jetzigen Kollegen. Es hat mir immer Spaß gemacht, mit dir zusammen zu arbeiten; schön, dass du dabei geblieben bist. Weiterer Dank geht an: **Väthi** für die Unaufgeregtheit, Loyalität und die Kaffeepausen. **Michel** für die stete Erinnerung an die Leichtigkeit des Seins. Die Feierabendbierrunden, u.a. mit **Fritzi, Kris, Mike, Andy** etc. Die ehemaligen EP 6 Leute: **Christian**, **Alex** (danke für die MTB Trails und die unvergessliche Zeit) und **Julia** (danke für die stets gute Laune, Lindt-Schokoladen-Komplizenschaft u.v.m.). Danken möchte ich auch noch unseren Technikern, **André** und **Valentin**, sowie **Diep**, der Guten Seele der EP 6.

Außerdem geht ein großer Dank an meine Bürokollegen **Hex** und **Hannes**. Ohne euch wüsste ich viele nützliche (und unnütze) Dinge nicht, und hätte viele Computerprobleme nicht (so prompt) gelöst bekommen. Ich hoffe ihr habt von meiner Anwesenheit symbiotisch genauso profitiert wie ich von eurer. Speziell unsere gemeinsame Zeit in Japan, lieber Hannes (& Nici & Lina), habe ich immer in wunderbarer Erinnerung.

Des Weiteren möchte ich unseren externen Kooperationspartnern für die produktive Zusammenarbeit danken, ohne die einige Ergebnisse meiner Arbeit nicht zustande gekommen wären: Prof. **Pavel Baranov** (Ioffe Institut, St. Petersburg, Russland), Dr. **Michael Trupke** (TU Wien, Wien, Österreich), Prof. **Tobias Hertel** und **Tilman Hain** (Physikalische Chemie II, Uni Würzburg), Prof. **Anke Krueger** und **Andreas Muzha** (Organische Chemie, Uni Würzburg).

Darüber hinaus sind mit mir einige Studienkollegen dem schönen Würzburg treu geblieben. Danke an **Martin, Marco, Sonja** und **Fabian** für schöne Abende, Ratschläge und Beistand und vor allem eure Freundschaft! In diesem Sinne auch ein herzliches Dankeschön an **Sarah** und **Anna**; ihr habt mir in den letzten drei Jahren mit Rat und Tat beiseite gestanden und Würzburg für mich mit Leben gefüllt!

Ein ganz besonderer Dank gebührt meinen Eltern, **Karl** und **Margit**, die den Grundstein für mein naturwissenschaftliches Interesse gelegt haben. Ihr habt mir nicht nur mein ganzes Studium finanziert, sondern seid immer für mich da und gebt mir den nötigen Rückhalt. Auch meinen Geschwistern **Ferdi** und **Vero** danke ich herzlich. Egal mit welchen Problemen oder wie groß der Labor-Frust sein mag, ich kann mich immer an euch wenden.